

AN ISOLATED CLASP TOG DOMAIN SUPPRESSES MICROTUBULE
CATASTROPHE AND PROMOTES RESCUE

APPROVED BY SUPERVISORY COMMITTEE

Luke M. Rice, Ph.D.

Xuewu Zhang, Ph.D.

Hongtao Yu, Ph.D.

Benjamin P. Tu, Ph.D.

DEDICATION

As with all things, dedicated to the incredible women in my life,
especially my mother, Jaba, my sister, Aalo, and grandmother,
Gitanjali.

AN ISOLATED CLASP TOG DOMAIN SUPPRESSES MICROTUBULE
CATASTROPHE AND PROMOTES RESCUE

by

SHREOSHI MAJUMDAR

DISSERTATION / THESIS

Presented to the Faculty of the Graduate School of Biomedical Sciences

The University of Texas Southwestern Medical Center at Dallas

In Partial Fulfillment of the Requirements

For the Degree of

DOCTOR OF PHILOSOPHY

The University of Texas Southwestern Medical Center at Dallas

Dallas, Texas

May, 2019

Copyright

By

SHREOSHI MAJUMDAR, 2019

All Rights Reserved

ACKNOWLEDGEMENTS

First and foremost, I would like to begin by thanking my thesis advisor, Dr. Luke Rice for the opportunity of working on a novel project and having faith in me despite the many roadblocks I faced. Without Luke's tenacity, Stu1 would have been relegated to the back of our -80 °C freezer and I would not have been writing this thesis. I have learned a lot from my tenure in his lab and I hope to implement these valuable lessons in my future career. I hope I have imbibed some of the elegance of experimental strategy, clarity of thinking, and eloquence of words that Luke has attempted to instill in us.

Next, I would like to thank my thesis committee, Dr. Xuewu Zhang, Dr. Hongtao Yu and Dr. Benjamin P. Tu for their guidance and support. Dr. Zhang kindly provided the key reagent of SUMO-plasmid that made expressing soluble Stu1 TOGs possible while Dr. Yu has been an incredible source of ideas especially at critical points when my project was at a standstill. And last but certainly not least, I am grateful to Dr. Tu for all his continuing advice throughout the years ever since I was a first-year rotation student in his lab.

If I have achieved anything these past six years, it has been accomplished by standing on the shoulders of giants. My Rice lab family have taught me everything I needed to know (and some things I really did not) and have made me laugh through it all. My siblings Sarah, Felipe, and Tae have been endless sources of moral support and help in wrangling Stu1. I cannot imagine my life without talking to them every day. I would be remiss if I did not extend my thanks to the entirety of ND10 including the SBL and MBR core facilities: in particular, I would like to thank Dr. James Chen, who has championed

my every effort and witnessed the first structure of Stu1-TOG2 with me, and Dr. Chad Brautigam whose scientific and baking skills I seek to emulate. Thanks are also due to Mr. Crispin for ensuring I never had to worry about paperwork.

Finally, I want to express my eternal gratitude to my family and friends for continuing to believe in me when I could not. My mother, Jaba, and my sister, Aalo, are the bedrock of everything I do. And the very large group of friends, the providers of lots of advice, pep-talks, entertainment (oh wait, I'm the entertainment), food, perspective, and much more. Special shout-outs to Joyce, my roommate and biophysics compatriot of five years; Leann, my fellow mermaid; Laura, who has taken me on many adventures; Rachel, my career guru; Deliana, who has no idea what I do but supports me all the same; Kathryn and Austin, who are always a phone call away; Jenny, who listens to my ridiculous stories; all of Canada; and Sureka, the last third of Eggroll.

AN ISOLATED CLASP TOG DOMAIN SUPPRESSES MICROTUBULE CATASTROPHE
AND PROMOTES RESCUE

Publication No. _____

Shreoshi Majumdar, Ph.D.

The University of Texas Southwestern Medical Center at Dallas

Supervising Professor: Luke M. Rice, Ph.D.

ABSTRACT

Microtubules are heavily regulated dynamic polymers of $\alpha\beta$ -tubulin that are required for proper chromosome segregation and organization of the cytoplasm. Polymerases in the XMAP215 family use arrayed TOG domains to promote faster microtubule elongation. Regulatory factors in the CLASP family that reduce catastrophe and/or increase rescue also contain arrayed TOGs. How CLASP TOGs contribute to activity is poorly understood. Using *S. cerevisiae* Stu1 as a model CLASP, I report structural, biochemical, and reconstitution studies that clarify functional properties of CLASP TOGs. To begin with, I introduce microtubules, their dynamics and regulatory proteins in Chapter 1. In Chapter 2, I discuss how the two TOGs in Stu1 have very different tubulin-binding properties: TOG2 binds to both unpolymerized and polymerized tubulin, and TOG1 binds very weakly to either. I also explore the structure of TOG2 and how it reveals a CLASP-specific residue that likely dictates distinctive tubulin-binding properties. Next, in Chapter 3, I study how, contrary to the expectation that TOGs must work in arrays, the isolated TOG2 domain strongly suppresses microtubule catastrophe and increases microtubule rescue in vitro. Single point mutations on the tubulin-binding surface of TOG2 ablate its anti-catastrophe and rescue activity in vitro, and Stu1 function in cells. Revealing that an isolated CLASP TOG can regulate polymerization dynamics without being part of an array provides insight into the mechanism of CLASPs and diversifies the understanding of TOG function. Finally, in Chapter 4, I will summarize my work and provide insight into future directions.

Table of Contents

ACKNOWLEDGEMENTS	xii
ABSTRACT	viii
PRIOR PUBLICATIONS	xi
LIST OF FIGURES	xii
LIST OF ABBREVIATIONS	xiii
CHAPTER ONE: INTRODUCTION	14
Microtubule function and dynamics	14
Microtubules are cytoskeletal components targeted by anti-cancer drugs.....	14
MTs are polymers of $\alpha\beta$ -tubulin subunits.....	15
Microtubule polymerization is driven by GTP hydrolysis and a conformational cycle.....	17
What do the ends of growing and shrinking MTs look like?.....	24
TOG-domain containing regulatory proteins	29
Regulation of MT dynamics by MAPs	29
Stu2/XMAP215 is a family of MT polymerases.....	32
The CLASP family are MT rescue and anti-catastrophe factors.....	40
My thesis project: elucidating the role of the CLASP TOGs	43
CHAPTER TWO: STRUCTURE & BIOCHEMISTRY	47
Abstract.....	47
Results	48
Construct design	48
Tubulin and microtubule binding properties of the Stu1 TOGs.....	51
Structure of the TOG2 domain from Stu1.....	62
Binding affinities of Stu1-TOG2 point mutants to tubulin and MT lattice.....	70
The TOG1-TOG2 fragment of Stu1 adopts a compact arrangement	75
Discussion	81
Experimental Procedures.....	84

CHAPTER THREE: RECONSTITUTION	93
Abstract.....	93
Results	94
The isolated Stu1-TOG2 domain suppresses catastrophe and stimulates rescue.....	94
Mutations on the tubulin-binding interface of Stu1-TOG2 abolish anti-catastrophe and rescue activity in vitro, Stu1 function in cells	99
The TOG2 domain does not detectably increase the EB comet	104
Discussion	106
Experimental Procedures.....	110
 CHAPTER FOUR: PERSPECTIVES	 93
Current work on Stu1-TOG2:tubulin interactions	119
Future Directions	120
 References	 125

PRIOR PUBLICATIONS

An isolated CLASP TOG domain suppresses microtubule catastrophe and promotes rescue. **Majumdar S**, Kim T, Chen Z, Munyoki S, Tso SC, Brautigam CA, Rice LM. *Mol Biol Cell*. **2018** Jun 1;29(11):1359-1375. doi: 10.1091/mbc.E17-12-0748. Epub 2018 Apr 5.

May I check your cap? Geyer, E. A*.; **Majumdar, S***; Rice, L. M.; *eLife*, **2016**;5: e15570

Antibody mechanics on a membrane-bound HIV segment essential for GP41-targeted viral neutralization. Kim M, Sun ZY, Rand KD, Shi X, Song L, Cheng Y, Fahmy AF, **Majumdar S**, Ofek G, Yang Y, Kwong PD, Wang JH, Engen JR, Wagner G, Reinherz EL. *Nat Struct Mol Biol*. **2011** Oct 16;18(11):1235-43. doi: 10.1038/nsmb.2154.

LIST OF FIGURES

Figure 1.1:	16
Figure 1.2:	21
Figure 1.3:	22
Figure 1.4:	23
Figure 1.5:	26
Figure 1.6:	27
Figure 1.7:	28
Figure 1.8:	31
Figure 1.9:	36
Figure 1.10:	37
Figure 1.11:	38
Figure 1.12:	39
Figure 1.13:	45
Figure 1.14:	46
Figure 2.1:	49
Figure 2.2:	50
Figure 2.3:	55
Figure 2.4:	56
Figure 2.5:	57
Figure 2.6:	58
Figure 2.7:	59
Figure 2.8:	60
Figure 2.9:	65
Figure 2.10:	66
Figure 2.11:	67
Figure 2.12:	72
Figure 2.13:	73
Figure 2.14:	74
Figure 2.15:	79
Figure 2.16:	83
Figure 3.1:	96
Figure 3.2:	97
Figure 3.3:	98
Figure 3.4:	102
Figure 3.5:	103
Figure 3.6:	105
Figure 4.1:	122
Figure 4.2:	123
Figure 4.3:	124

LIST OF ABBREVIATIONS

- AUC – analytical ultracentrifugation
- CD – circular dichroism
- CLASP – cytoplasmic linker associated protein
- DCX – Doublecortin
- Dis1 – distorted trichomes 1
- DMSO – dimethyl sulfoxide
- EB1 – End-binding protein 1
- EM – Electron microscopy
- E-site – Exchangeable site
- GDP – Guanosine diphosphate
- GTP – Guanosine-5'-triphosphate
- GTP γ S - Guanosine 5'-O'[γ -thio]triphosphate
- GMPCPP - Guanosine-5'-[(α , β)-methylene]triphosphate
- HEAT – Huntingtin, elongation factor 3, protein phosphatase 2A, and the yeast kinase TOR1
- MAP – Microtubule associated protein
- MCAK – Mitotic centromere-associated kinesin
- MT(s) – Microtubule(s)
- N-site – Non-exchangeable site
- PEG – polyethylene glycol
- Stu1 – Suppressor of tubulin 1
- Stu2 – Suppressor of tubulin 2
- TOG – Tumor overexpressed gene
- XMAP215 – Xenopus microtubule-associated protein 215

CHAPTER ONE: INTRODUCTION

Microtubule function and dynamics

Microtubules are cytoskeletal components targeted by anti-cancer drugs

Microtubules (MTs) are long, hollow polymers of $\alpha\beta$ -tubulin that are essential to the cellular function and organization (Brouhard, 2015; Brouhard and Rice, 2018; Desai and Mitchison, 1997). In non-mitotic cells, these cytoskeletal filaments organize the cytoplasm, serve as tracks for motor-based transport of cargo, and regulate cellular migration, polarity and morphogenesis (Akhmanova and Steinmetz, 2015; Akhmanova and Steinmetz, 2008). In dividing cells, MTs are integral components of the mitotic spindle that is essential for faithful segregation of chromosomes.

Because of their role in cell division, MTs are important targets for anti-cancer therapeutics including taxol (paclitaxel), vinca alkaloids, and colchicine. Specifically, MT-targeted drugs affect MT function by perturbing one of their most fundamental properties. MTs are highly dynamic and rapidly switch between phases of growth and shrinking, a phenomenon known as dynamic instability (Desai and Mitchison, 1997). MT dynamics are critical to their functioning and allow them to properly engage and segregate chromosomes. Chemotherapy drugs disrupt MT dynamics in different ways. Taxol, for example, binds to the MT lattice (β -tubulin) to stabilize the polymer and prevent disassembly. This in turn blocks the progression of mitosis. Cells are arrested at the mitotic checkpoint triggering apoptosis or reversion to the G0 phase of cell division. Recent studies also indicate that taxol might suppress MT detachment from

centrosomes (Bharadwaj and Yu, 2004; Brito et al., 2008; Ganguly et al., 2010; Jordan and Wilson, 2004). Further understanding of MTs, their dynamics, and regulation could lead to the development of novel anti-cancer agents.

MTs are polymers of $\alpha\beta$ -tubulin subunits

$\alpha\beta$ -tubulin subunits comprise of individual α - and β -tubulin monomers bound together as an obligate heterodimer (Figure 1.1-A). The heterodimers assemble head-to-toe (longitudinal interactions) into protofilaments and then the protofilaments interact laterally to form a hollow tube. The number of protofilaments varies between 11-15 with 13 being the most common number (Chaaban and Brouhard, 2017; Chalfie and Thomson, 1982; Desai and Mitchison, 1997). *In vivo*, the number depends on cell type and species while *in vitro*, the type of nucleotide bound to the tubulin, presence of drugs or regulatory proteins can all affect protofilament number (Bechstedt and Brouhard, 2012; Díaz et al., 1998; Hyman et al., 1995). The majority of the lateral contacts between protofilaments are homotypic i.e. α -tubulin to α -tubulin and β -tubulin to β -tubulin. However, as a typical 13-protofilament MT wraps around, the lateral contacts are disrupted at the seam where they are heterotypic i.e. α -tubulin to β -tubulin (Figure 1.1-B). The function and role of the seam in MT dynamics is a matter of much interest. The plus-end of the MT (β -tubulin exposed) is the primary site of MT elongation in cells and demonstrates fast growth *in vitro*. The minus-end (α -tubulin exposed) can also show growth in *in vitro* reconstitution assays but the dynamics including growth rate are significantly suppressed compared to the plus-end (Akhmanova and Steinmetz, 2015; Brouhard and Rice, 2014). (Figure 1.1-B)

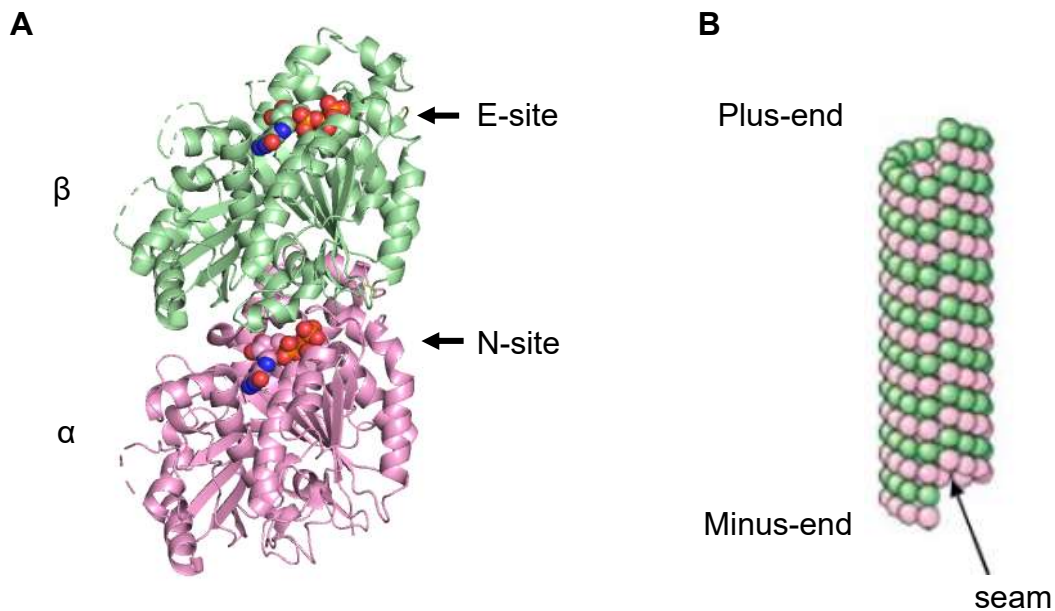


Figure 1.1: $\alpha\beta$ -tubulin heterodimers assemble into protofilaments that interact laterally to form a microtubule.

A. Structure of yeast $\alpha\beta$ -tubulin from PDB code 4FFB with α -tubulin in pink and β -tubulin in green. GTP binding sites are highlighted using spheres. β -tubulin site is exchangeable (E-site) whereas the α -tubulin site is not (N-site)

B. Heterodimers assemble 'head to toe' into a polar microtubule with a plus-end (α -tubulin exposed) and a minus-end (β -tubulin exposed). The minus-end is typically protected *in vivo*.

Microtubule polymerization is driven by GTP hydrolysis and a conformational cycle

MTs exhibit apparently random switching between phases of polymerization and rapid depolymerization, labeled dynamic instability. The transition event from growth to rapid shrinking is called catastrophe and from catastrophe back to growth is called rescue (Figure 1.2). Two processes drive dynamic instability: a nucleotide hydrolysis cycle and a tubulin conformation cycle (Brouhard, 2015; Desai and Mitchison, 1997; Mitchison and Kirschner, 1984).

Both tubulin monomers, α - and β -, bind a single GTP or GDP molecule each. In the heterodimer, α -tubulin-bound GTP is buried at the interface of the two monomers and is rendered non-exchangeable (N-site, Figure 1.1 A) (Nogales et al., 1998). The β -tubulin site remains solvent-exposed and therefore, exchangeable (E-site, Figure 1.1 A) (Mitchison, 1993; Nogales, 2000). During polymerization of $\alpha\beta$ -tubulin into MTs, the addition of a subunit stacked onto an existing one at the tip completes the GTP hydrolysis active site (Nogales et al., 1999). The GTP bound to β -tubulin hydrolyzes. Over the course of elongation, heterodimers within the lattice undergo GTP hydrolysis eventually creating a highly unstable core of GDP-bound subunits (Desai and Mitchison, 1997).

Since the binding affinity of solution-state tubulin to the MT tip is relatively low, hydrolysis occurs at a delay after the incorporation of a subunit at the tip (usually the plus-end). Consequently, the MT tip has a layer of unhydrolyzed GTP-tubulins. This “stabilizing GTP cap” protects the MT from depolymerization. Loss of this cap has been shown to induce catastrophe and disintegration of the MT into free tubulin. The free GDP-bound tubulin dimers can now undergo nucleotide exchange and acquire a GTP

molecule priming them to re-enter the assembly-disassembly cycle. (Figure 1.2)
(Brouhard and Sept, 2012).

During the continuing process of growth and shrinking and associated GTP hydrolysis, $\alpha\beta$ -tubulin also undergoes conformational changes. Individual heterodimers can pass through at least three distinct conformations. These are as follows: 1) unpolymerized tubulin in a “curved” conformation, 2) polymerized tubulin in a “straight, expanded” conformation and lastly, 3) polymerized tubulin a “straight, compacted” conformation. Several high-resolution structures of tubulin that support this mechanism have been obtained through electron crystallography, X-ray crystallography, and most recently cryo-electron microscopy. A fourth conformation of “straight, compacted & twisted” has also been described through recent cryo-electron microscopy studies. (Figure 1.3)
(Alushin et al., 2014; Zhang et al., 2015)

Unpolymerized, GTP-bound tubulin exists in the curved conformation, characterized by an approximately 12° kink at the interface between the individual monomers. High-resolution crystal structures of $\alpha\beta$ -tubulin in complex with a binding partner are consistent with this curved conformation and show a distinct rotation of one monomer against the vertical axis versus the other. (Ayaz et al., 2012, 2014; Gigant et al., 2000; Prota et al., 2014).

Originally, polymerized tubulin was believed to exist in a single “straight” conformation where the individual monomers are not rotated. The original structural findings from electron crystallography of zinc-induced tubulin sheets demonstrated that the tubulin monomers comprise of a core of two beta-sheets surrounded by alpha-helices. The monomers could be overlaid on top of one another with a simple translation along the

vertical axis i.e. a “straight” conformation (Nogales et al., 1998) (Figure 1.4). Recent studies have indicated a more nuanced view and given rise to the possibility of multiple “straight” conformations. Using cryo-electron microscopy, it has been demonstrated that right after binding the MT tip, heterodimers straighten into a “straight, expanded” conformation. Once in the body of the MT lattice, the heterodimer undergoes subsequent GTP hydrolysis and release of inorganic phosphate, and adopts a “straight, compact” conformation. This conformation is shorter in length by 3 Å due a movement of an α -tubulin subdomain (Alushin et al., 2014). (Figure 1.3)

Figure 1.4 reproduced from a prior paper serves to further elucidate the rotational difference between the monomers in the different conformations (Rice et al., 2008). In the straight conformation (top panel), a simple translation is enough to align the α -tubulin and β -tubulin structures. In the curved conformations, however, in addition to a translation, one of the monomers needs to be rotated. The degree of rotation can vary between 10-13° depending on the crystal structure.

The nucleotide state of the MT lattice may add further nuance to the “straight, compact” conformation. Studies on the conformational state of tubulin have largely been carried out on mammalian MTs, either stabilized by non-hydrolyzable GTP analog GMPCPP (mimic for GTP-bound state) or allowed to grow for short periods in the presence of GTP (to study GDP-bound state) [Alushin 2014]. Further studies by the Nogales lab using GTPyS, a slowly-hydrolyzable GTP analog, indicates that in addition to compaction, there may be a small twist in the lattice giving rise to the possibility of a “straight, compacted & twisted” state (Manka and Moores, 2018; Zhang et al., 2015). GTPyS is believed to be a close mimic of the GDP-Pi nucleotide state that occurs right

after hydrolysis and right before release of the inorganic phosphate. Thus, this intermediate state is ripe for future study. Furthermore, the compaction may be species-dependent. This work was carried out in mammalian MTs but recent structures of yeast MTs have shown no evidence of compaction in the MT lattice (Howes et al., 2017; von Loeffelholz et al., 2017).

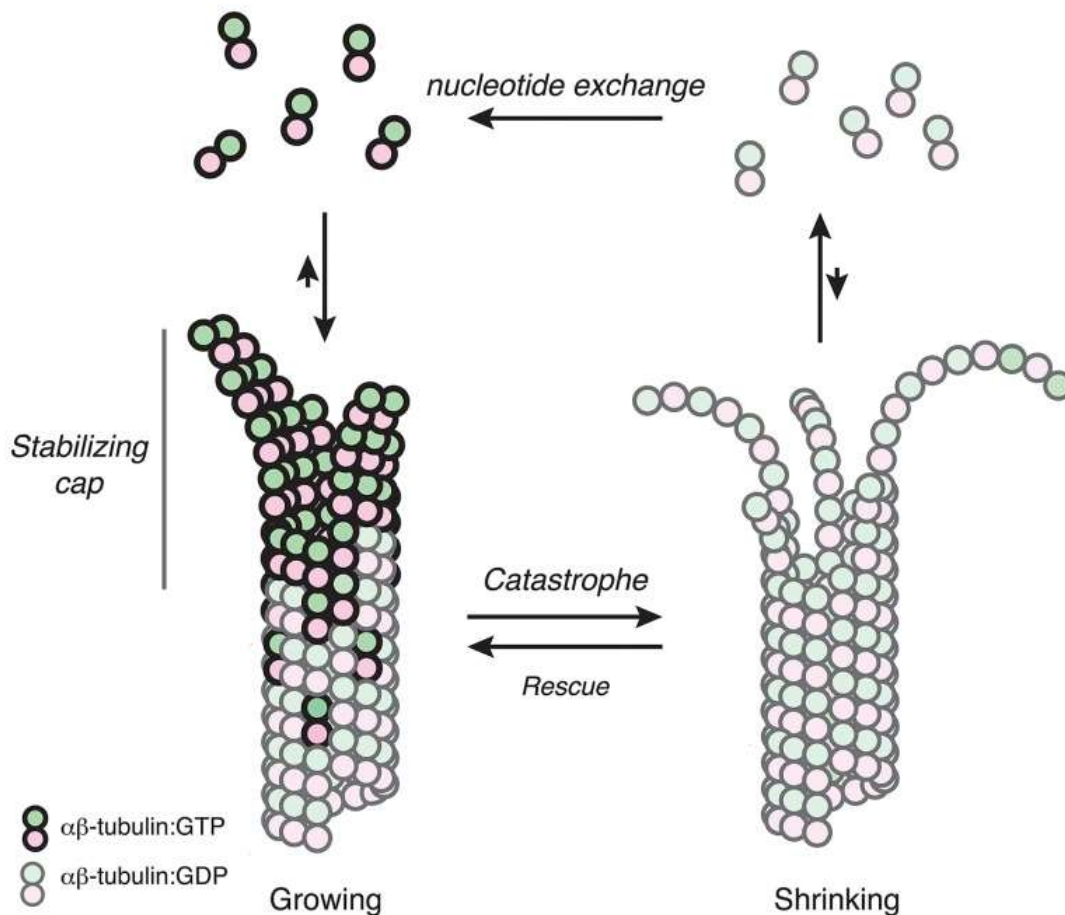


Figure 1.2: the cycle of microtubule polymerization (figure and legend reproduced from Brouhard and Rice, 2014).

Microtubules are hollow cylindrical polymers composed of $\alpha\beta$ -tubulin subunits. Microtubule polymerization occurs through the addition of GTP-bound $\alpha\beta$ -tubulin subunits onto microtubule ends. Growing microtubule ends show outwardly curved, tapered, and flattened end structures (left), presumably reflecting the conformational changes that occur during polymerization. The addition of a new subunit completes the active site for GTP hydrolysis, and consequently most of the body of the microtubule contains GDP-bound $\alpha\beta$ -tubulin. The GDP lattice is unstable but protected from depolymerization by a stabilizing “GTP cap,” an extended region of newly added GTP- or GDP.Pi-bound $\alpha\beta$ -tubulin. The precise nature of the microtubule end structure and the size and composition of the cap are a matter of debate. Loss of the stabilizing cap leads to rapid depolymerization, which is characterized by an apparent peeling of protofilaments. “Catastrophe” denotes the switch from growth to shrinkage, and “rescue” denotes the switch from shrinkage to growth.

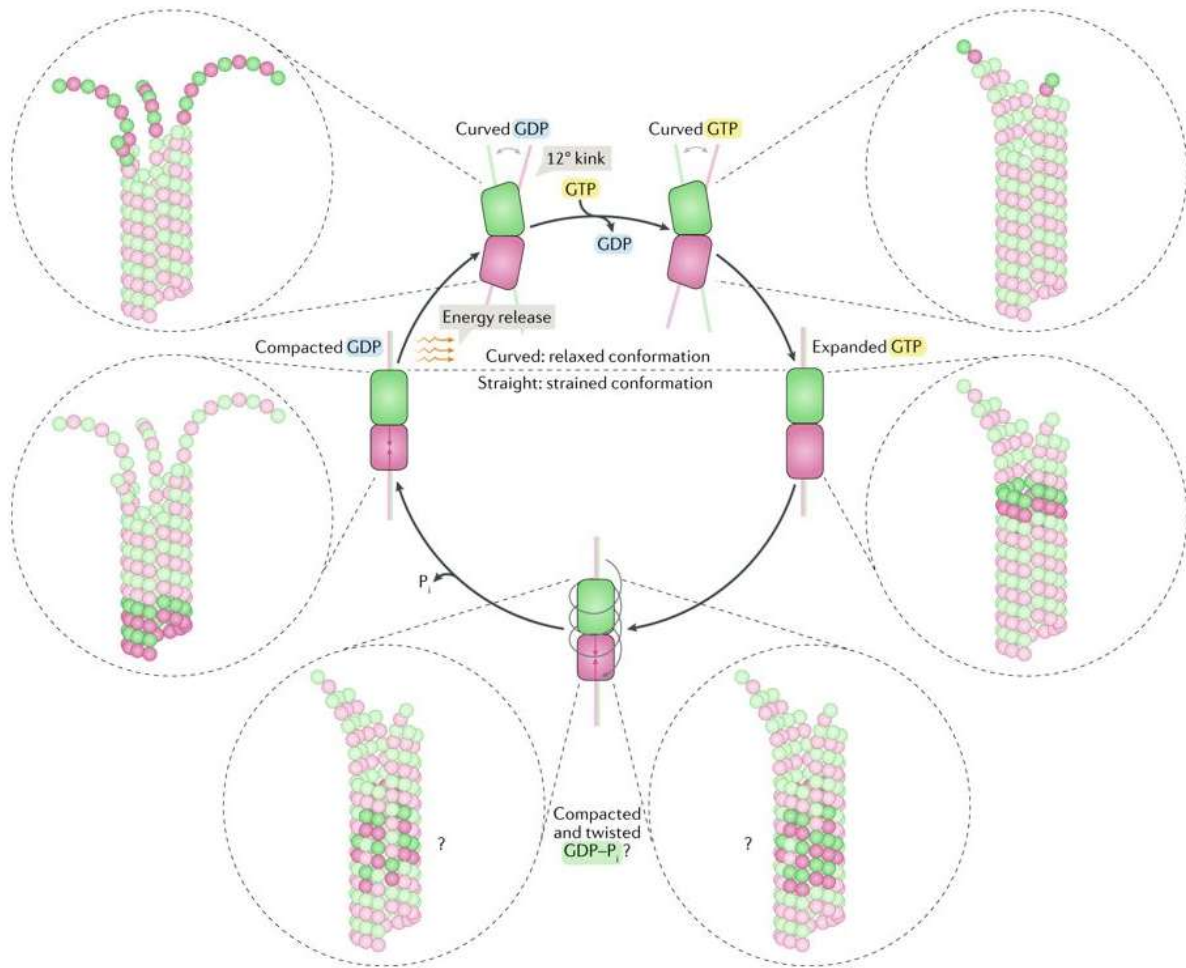


Figure 1.3: The different conformational states of tubulin. Figure reproduced from Brouhard and Rice, 2018.

During assembly and disassembly, $\alpha\beta$ -tubulin cycles through at least three distinct conformation. Solution-state tubulin is curved and straightens out in the body of the MT lattice. Initially, when the tubulin subunit is at the MT tip, it is in an expanded conformation and gradually undergoes upward compaction in α -tubulin with hydrolysis, resulting in compacted and compacted & twisted conformations.

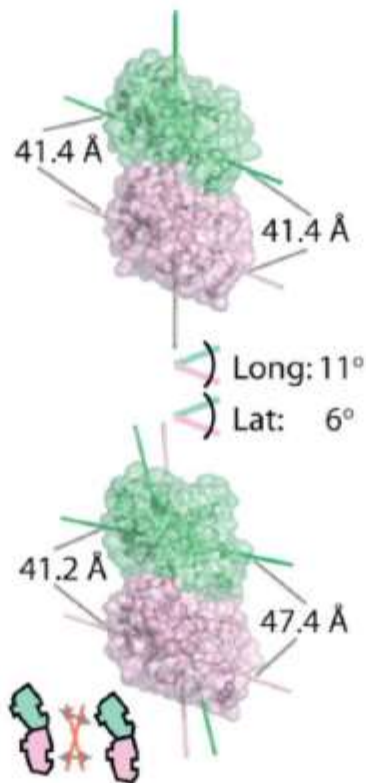


Figure 1.4: Two conformations of $\alpha\beta$ -tubulin. Figure and legend reproduced from Rice et al., 2008.

Longitudinal and lateral interaction surfaces are aligned in the straight (1JFF, top), but not in the curved (1SA0, bottom) conformation. In the curved conformation, the α - and β -tubulin protofilament and lateral interaction axes are skewed by 11° and 6° , respectively; these rearrangements separate equivalent laterally interacting atoms by up to 6 Å. (*Inset*) This misalignment of interfaces destabilizes lateral interactions between curved $\alpha\beta$ -tubulins.

What do the ends of growing and shrinking MTs look like?

Clearly, there is scope for much further investigation of the different states of tubulin conformation in the body of MT lattice. There is also a lot of ground to be covered in the investigation of the structure of the MT tip. The stabilizing cap at the tip of the growing MT contains hundreds of tubulin dimers (Bieling et al., 2007). Thanks to cryo-electron microscopy, we have several structures of the growing MT tip: ends have been captured in a broad variety of structures ranging from short, blunt ends to long, outwardly-curved, flattened sheet-like extensions (Chrétien et al., 1995; Mandelkow et al., 1991). To quote Brouhard & Rice “while scientists are not necessarily artists, and we differ in our tolerance for flourish, it’s fair to say that the field has no consensus about what a microtubule end actually looks like” (Brouhard and Rice, 2018). The data do indicate that the ends are not so blunt. Some protofilaments are longer than others giving rise to end tapering and some degree of curvature is present. A schematic representation from Brouhard & Rice 2018 is reproduced in Figure 1.5 and a survey of micrographs from Mandelkow et. al 1991 is reproduced in Figure 1.6. In the section on XMAP215 polymerases, I describe the current model for how a polymerase increases MT growth rate by acting directly on the growing ends.

On the other hand, shrinking MT ends and the mechanisms behind inducing catastrophe are not as well-studied as their growing counterparts. This may be attributed to the time-resolution limits of microscopy when studying fast shrinking and possibly fewer protein families that track the shrinking ends (unlike the abundance of tip-trackers for the growing ends). From limited cryo-electron microscopy studies on depolymerizing MTs, we can see that subsequent to catastrophe, GDP-bound tubulin

dimers return back to the curved conformation as demonstrated by the “banana peel” or “ram’s horns” configuration adopted by protofilaments. A reproduction of micrographs from Mandelkow et. al. 1991 is provided in Figure 1.7. The increasing end tapering of the protofilaments as they “peel” off from the MTs can help envision some possible mechanisms for promoting catastrophe. For example, MCAK tightly binds curved $\alpha\beta$ -tubulin and can promote MT depolymerization by stabilizing the curved conformation of $\alpha\beta$ -tubulin at the MT end leading to enhanced protofilament curvature (Gardner et al., 2011; Helenius et al., 2006). Conversely, a possible mechanism for an anti-catastrophe regulatory protein could be that the protein stabilizes the unfurling protofilaments at the shrinking end and prevents further curvature or stabilizes a “straighter” version of tubulin/protofilaments and reduces curvature. This would allow the shrinking microtubule to return to a growing state. I explore the idea further in Chapter 4.

The mechanisms behind the transition events, catastrophe and rescue, are poorly understood. My hope is that through the study of proteins that regulate catastrophe and rescue, we might be able to understand more about the molecular origin of the transitions between growing and shrinking.

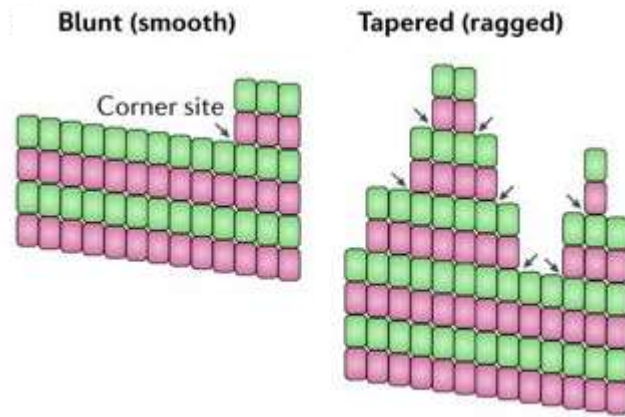


Figure 1.5: Schematics of the growing MT plus-end. Figure and legend reproduced from Brouhard and Rice 2018.

Two-dimensional schematics of blunt (few corner sites, arrows) and tapered (more corner sites, arrows) microtubule ends. Tapering refers to the extension of some protofilaments beyond others; raggedness describes an uneven or rough distribution of protofilament lengths.

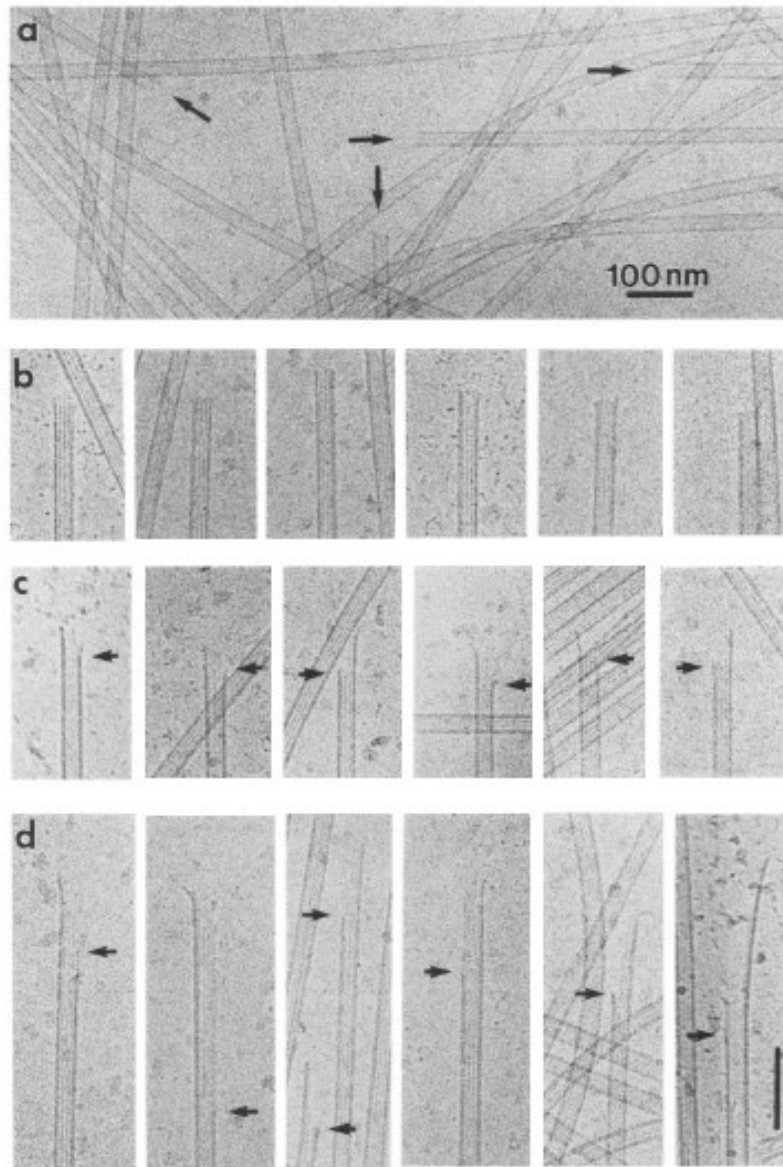


Figure 1.6: Micrographs of the growing MT plus-end. Figure and legend reproduced from Mandelkow et al., 1991.

Micrographs showing different protuberances of protofilaments from the end of growing microtubules: a) survey with several blunt ends (arrows) b) Blunt ends, all protofilaments terminate almost simultaneously. c) short protuberances of protofilaments, up to 50 nm long d) long protuberances (>50 nm). Scale bar, 100 nm.

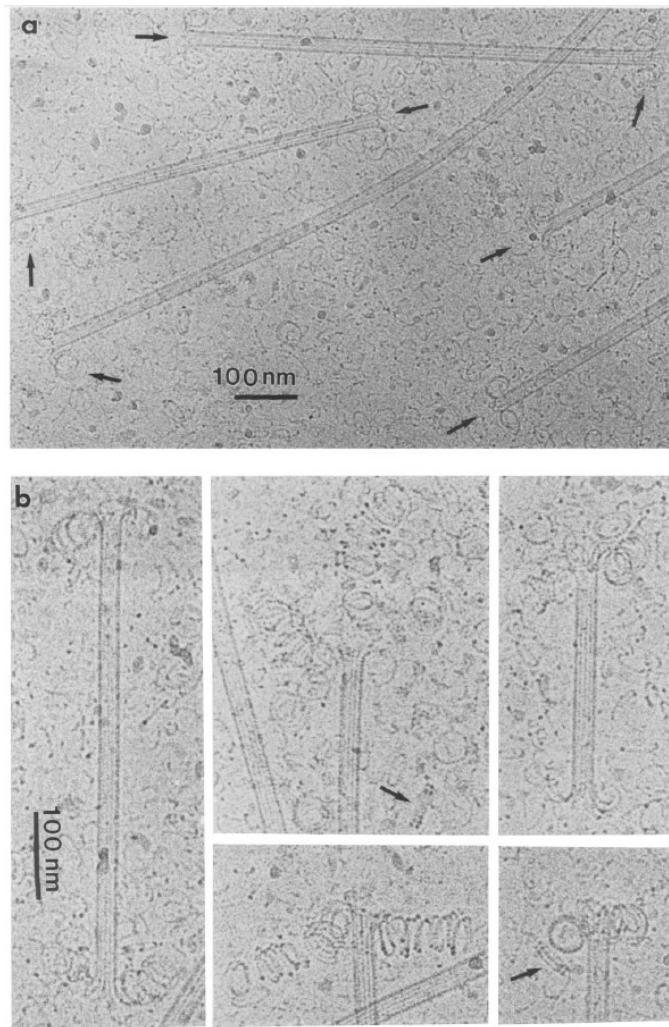


Figure 1.7: Micrographs of the shrinking MT end. Figure and legend reproduced from Mandelkow et al., 1991.

Shrinking microtubules (11 mg/ml), 12 s after the addition of 20 mM Mg²⁺. (a) Survey, (b) details at higher magnification. Note the pronounced coiling at microtubule ends and the increased concentration of oligomers in the background. Bar, 100 nm.

TOG-domain containing regulatory proteins

Regulation of MT dynamics by MAPs

The property of dynamic instability in MTs facilitates rapid reorganization of microtubule networks and is crucial for the effectiveness of the MT cytoskeleton in responding to the needs of the cell. Left to its own devices, *in vitro*, $\alpha\beta$ -tubulin can cycle between MT polymers and free tubulin with only the addition of appropriate buffering conditions, excess GTP, and a seeding substrate. In the cell, however, the process is heavily regulated through mechanisms involving hundreds of additional proteins. Of particular interest to us are the proteins that can alter MT dynamics, microtubule-associated proteins (MAPs). MAPs are capable of significantly affecting MT structure and function. Several families of MAPs have been identified and display a broad range of function. A large number of these MT regulatory factors have been identified, but the molecular mechanisms behind their activity are still being understood.

Several types of the more well-understood MAPs are illustrated in Figure 1.8 reproduced from Brouhard and Rice 2018: 1) microtubule polymerases such as XMAP215 promote faster growth (described in subsequent sections) (Brouhard et al., 2008), 2) depolymerases such as MCAK promote shrinking and/or catastrophe (MCAK preferentially binds curved $\alpha\beta$ -tubulin removing tubulin subunits at MT end and inducing curvature in protofilaments to promote catastrophe, (Gardner et al., 2011; Helenius et al., 2006; Hunter et al., 2003), 3) End-binding proteins (EB1, Bim-1) recognize and bind to the specific conformation state of compacted & twisted in the MT lattice and increase catastrophe frequency by speeding up the rate of GTP hydrolysis (Duellberg et al., 2016; Maurer et al., 2012, 2014), 4) Doublecortin (DCX) binds to the MT end stabilizing

the curved conformation of tubulin at the very tip of the MT and nucleates MTs from free tubulin (Bechstedt and Brouhard, 2012) and 5) MT nucleation/anti-catastrophe factor, TPX2, which also preferentially binds partially curved tubulin at MT ends and is believed to stabilize $\alpha\beta$ -tubulin: $\alpha\beta$ -tubulin interactions (Reid et al., 2016; Roostalu et al., 2015).

Notably absent from this diagram of important MAPs are the family of rescue/anti-catastrophe factors, the CLASPs. Varied functions of this family in promotion of MT rescue, suppression of MT catastrophe, kinetochore attachment and inter-MT interactions have been studied. However, despite the fact that the CLASPs contain tubulin-binding domains similar to the well-studied XMAP215 polymerases, we understand little about the underlying molecular mechanism to the extent that a pictorial description such as the preceding figure will not suffice.

The overarching goal of my project has been to gain insight into the molecular origin of CLASP function through biochemical, structural and reconstitution assays. In Chapter 2, I describe the results of the biochemical and structural studies that I have conducted and in Chapter 3, I look at *in vitro* reconstitution of MT dynamics and the effect of a CLASP family member on them.

Before I proceed to describe these experimental results, in the following sections, I offer a more thorough introduction to the CLASP family as well as the Stu2/XMAP215 polymerases and how they influence MT dynamics.

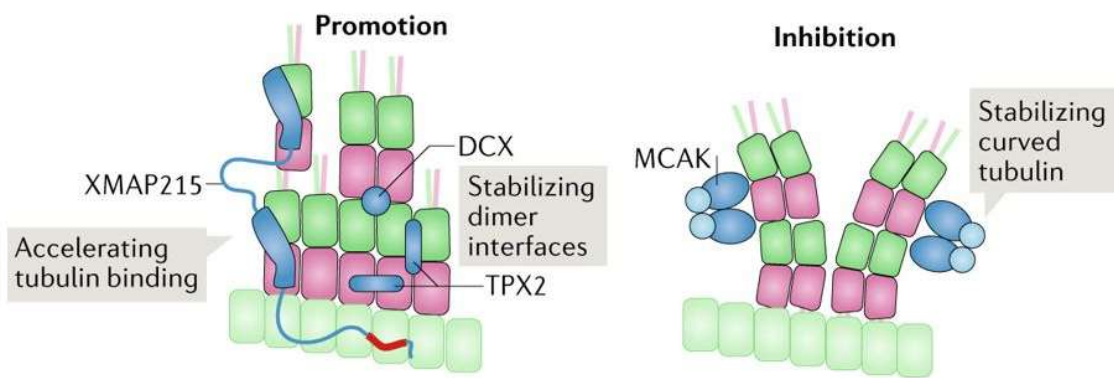


Figure 1.8: MAPs regulate MT dynamics by performing a variety of functions.
Figure and legend reproduced from Brouhard and Rice 2018.

Microtubule-associated proteins (MAPs) regulate microtubule nucleation by recognizing and altering the conformation of tubulin. Nucleation-promoting MAPs such as XMAP215, targeting protein for Xklp2 (TPX2) and neuronal migration protein doublecortin (DCX) help form a nascent plus end (left). They recognize curved tubulin conformations present at the microtubule tip and accelerate addition of $\alpha\beta$ -tubulin (XMAP215; only two of its TOG domains are shown) or stabilize tubulin–tubulin interaction at interfaces between dimers (TPX2 and DCX). Nucleation-inhibiting MAPs such as mitotic centromere-associated kinesin (MCAK) destabilize the microtubule end by binding and promoting highly curved tubulin conformation (right).

Stu2/XMAP215 is a family of MT polymerases

Microtubule polymerases in the Stu2/XMAP215 family increase the growth rates of MTs significantly *in vivo* and *in vitro*. Reconstitution assays *in vitro* have demonstrated a five-fold increase in polymerization rates of MTs when XMAP215 is present (Brouhard et al., 2008; Widlund et al., 2011). The polymerases share a common overall domain organization similar to the CLASPs: multiple arrayed tubulin-interacting TOG domains followed by an SK-rich basic domain and a flexible C-terminal tail (Figure 1.9). The higher eukaryotic members such as XMAP215 are monomeric while the lower eukaryotic ones like the *Saccharomyces cerevisiae* polymerase Stu2 are dimeric proteins. The dimeric proteins have a coiled-coil domain following the basic domain that enables homodimerization (Figure 1.9).

TOG (Tumor Overexpressed Gene) domains are small (25-30 kDa) paddle-shaped, helical repeat proteins. Each domain contains approximately six HEAT (Huntingtin, elongation factor 3, protein phosphatase 2A, and the yeast kinase TOR1) repeats.

Three major families of MAPs are known to contain TOGs: Stu2/XMAP215 polymerases, CLASP rescue factors, and the cilia-specific Crescerin, which also promotes MT polymerization (Akhmanova and Steinmetz, 2015; Das et al., 2015)

The most well-studied TOG domains are the polymerase ones, especially those from the *Saccharomyces cerevisiae* Stu2. Stu2 is an essential protein in yeast with degradation resulting in cell death (Ayaz et al., 2014; Wang and Huffaker, 1997). In addition to activity as a MT polymerase, Stu2 has also been shown to localize to sites of kinetochore attachment and microtubule-organizing centers (Miller et al., 2016).

These better understood Stu2/XMAP215 proteins provide a paradigm for understanding the role of TOG domains in influencing MT dynamics. Based on extensive characterization of XMAP215 and Stu2, we know that MT polymerase activity requires at least two TOGs (Widlund et al., 2011), each of which binds tightly to curved conformation, unpolymerized tubulin but weakly, if at all, to straight conformation tubulin in the microtubule (Ayaz et al., 2012; 2014). The binding affinities of the Stu2 TOGs are similar (TOG1 binds about two-fold tighter at ~70 nM as opposed to TOG2 at ~150 nM, Figure 1.10). How do these affinities compare to the rescue TOGs? I discuss the interactions of rescue TOGs and tubulin/MT lattice in Chapter 2.

Crystal structures of the two Stu2 TOG domains bound to $\alpha\beta$ -tubulin were obtained by our lab and revealed key insights into TOG:tubulin interactions. Each TOG interacts with a single $\alpha\beta$ -tubulin via two critical residues: an arginine (Stu2 TOG1 R200/ Stu2 TOG2 R519) that forms electrostatic interactions with α -tubulin and a tryptophan (Stu2 TOG1 W23/ Stu2 TOG2 W341) that contacts β -tubulin through hydrophobic interactions (Figure 1.11). Mutating either residue abolishes the high-affinity interaction (Ayaz et al., 2014). A docked structure of either TOG domain onto the structure of straight tubulin explains why the TOGs are compatible with a single curved tubulin: the docked TOG can no longer simultaneously engage both α - and β - subunits (Figure 1.11-B). The dual engagement is critical to the binding activity of the polymerase TOGs. As noted earlier, these two residues are also conserved in rescue TOGs but particularly only in TOG2s. The results of mutating the conserved tryptophan and arginine residues in Stu1 TOG2 is also described in Chapter 2. Additionally, recent structural studies of CLASP TOGs

have revealed a distinctive domain structure that may underlie different tubulin-binding properties (Leano et al., 2013; Maki et al., 2015).

In the polymerase Stu2, the two TOG domains are biochemically and structurally very similar. *In vivo* experiments have demonstrated that they might be interchangeable as well. Yeast genetic assays that allow for inducible depletion of Stu2 have shown that in the background of a Stu2 dimer, replacing the native TOG1 with TOG2 had no effect on cell viability (Ayaz et al., 2014). In a dimer background, mutating the tubulin-binding residues of either TOG1 or TOG2, thereby creating “non-functional” TOGs, had little effect as well. In a monomer background, however, mutations in either TOG greatly diminishes cell viability (Ayaz et al., 2014). A minimum of two “functional” TOGs are required for viable cells, which is consistent with previous studies of XMAP215.

Further studies have shown that polymerase activity also requires that the TOGs be coupled to a basic region that provides affinity for the negatively charged tubulin C-terminii that decorate the microtubule surface (Widlund et al., 2011). Single polymerase TOGs bereft of a basic domain bind so tightly to curved tubulin that they end up sequestering free tubulin preventing MT elongation.

Does CLASP activity also require that multiple TOGs work together? Are CLASP TOG1 and TOG2 interchangeable? I delve into these ideas in Chapter 3.

Taken together, a tethering mechanism has been proposed for Stu2 function and is outlined in Figure 1.12 (Ayaz et al., 2014; Geyer et al., 2018). As Stu2 adheres to the end of a growing MT, one of the TOG domains stabilizes a weakly bound tubulin dimer at the end, preventing its disassociation and encouraging association. The other TOG

“searches” for solution-state free tubulin and sequesters the dimers, bringing them back to the MT end. Associations between the two dimers drive conformational change from curved to straight releasing the attached TOGs and allowing them to repeat the process. The resulting increase in concentration of tubulin dimers near the growing MT tip serves to greatly increase polymerization.

Since CLASPs/Stu1 influence transitions events such as rescue and catastrophe, I speculate that Stu1 also has a mechanism involving the MT tip in Chapter 4.

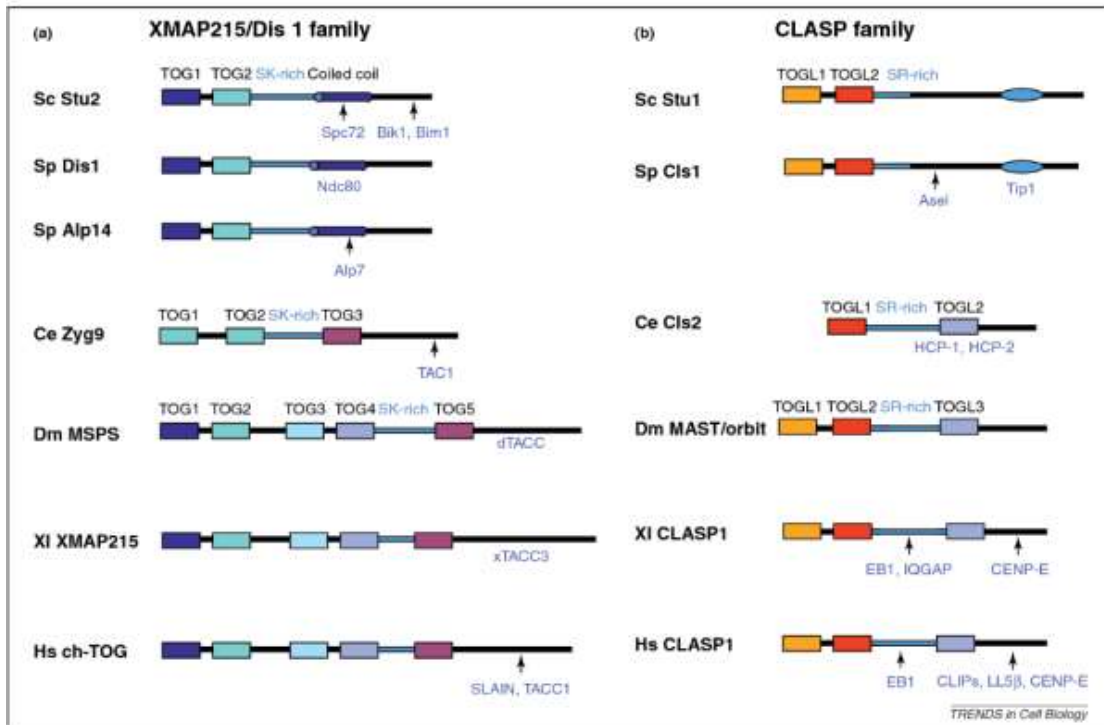


Figure 1.9: Domain organization of XMAP215/Dis1 and CLASP families from yeast, worms and mammals and their binding partners. Figure and legend reproduced from (Al-Bassam and Chang, 2011).

(a) XMAP215/Dis1 proteins contain conserved TOG domains and an SK-rich domain. Domain organization of yeast orthologs *S.cerevisiae* Stu2, *S.pombe* Dis1 and Alp-14 with two TOG domains, *C. elegans* Zyg9 with three and *D. melanogaster* MSPS, *Xenopus laevis* XMAP215 and human ch-TOG with five. All molecules contain regions with stretches of sequences rich in serine, glycine and lysine (SK-rich domains). TOG domains are colored on the basis of the conserved phylogenetic classes from sequence alignments (Figure 5): TOG1 class, blue; TOG2 class, cyan; TOG3 class, sky blue; TOG4 class, purple; TOG5 class, maroon. Protein binding partners (blue) described in the text are shown below each protein, with arrows denoting approximate binding sites. An absence of an arrow denotes an interaction in which binding domains have not been mapped. (b) CLASP proteins contain conserved TOG-Like (TOGL) domains and SR-rich domains. Similar to (a), domain organization of *S. cerevisiae* Stu1 and *S. pombe* Cls1 with two TOGL domains, *C. elegans* Cls2 with two TOGL domains and *D. melanogaster* MAST/orbit, human and *X. laevis* CLASP1 with three TOGL domains. All molecules contain regions with stretches of sequences rich in serine, proline and arginine (SR-rich domains). TOGL domains are colored on the basis of the conserved phylogenetic classes from sequence alignments (shown in Al-Bassam 2011): TOGL1 class, orange; TOGL2 class, red; TOGL3 class, purple. Protein binding partners (blue) described in the text are shown below each protein with arrows denoting approximate binding sites based on studies described in the text. The absence of an arrow denotes an interaction in which the interacting domain has not been mapped.

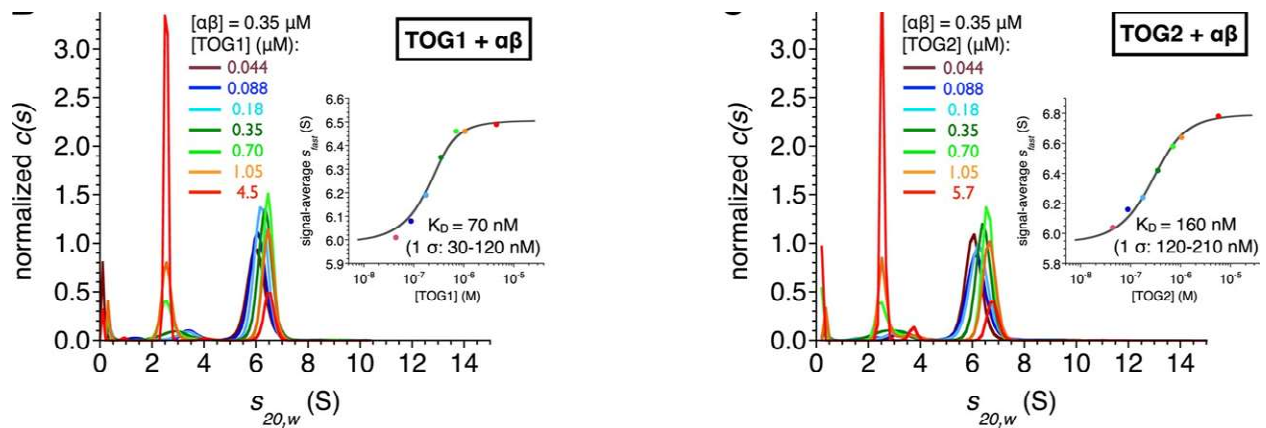


Figure 1.10: Stu2 TOGs bind $\alpha\beta$ -tubulin with comparable affinity. Figures reproduced from Ayaz et. al. 2014.

Analytical ultracentrifugation sedimentation velocity experiments show that Stu2 TOGs binds $\alpha\beta$ -tubulin tightly with fitted affinities of 70 nM (TOG1, left) and 160 nM (TOG2, right). Inset plots are the fit to a 1:1 binding isotherm of s_{fast} .

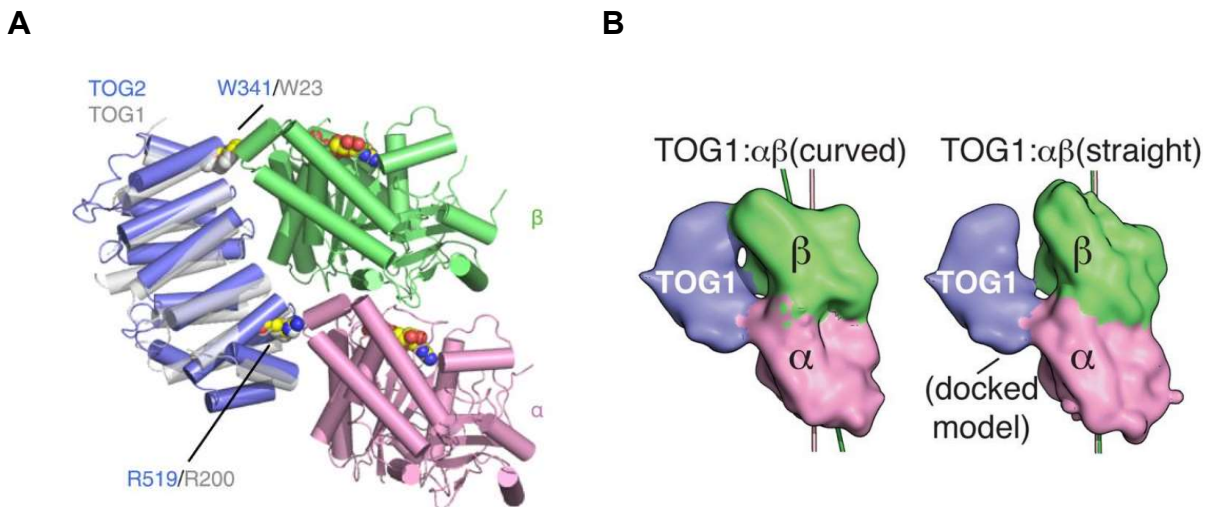


Figure 1.11: Crystal structures of Stu2 TOG:tubulin complex. Figures and legends are reproduced from Ayaz et al., 2014 (A) and Ayaz et al., 2012 (B).

A. Structure of the TOG2: $\alpha\beta$ -tubulin complex (TOG2: slate, α -tubulin: pink, β -tubulin: green), with the important binding residues W341 and R519 represented as spheres. The semi-transparent gray cartoon shows the previously observed binding mode of TOG1, with its binding residues W23 and R200 depicted as spheres.

B. The structure of the TOG1: $\alpha\beta$ -tubulin complex (left) and a docked model with straight $\alpha\beta$ -tubulin (right) illustrates how TOG1-contacting epitopes on α - and β -tubulin move relative to each other in the two conformations.

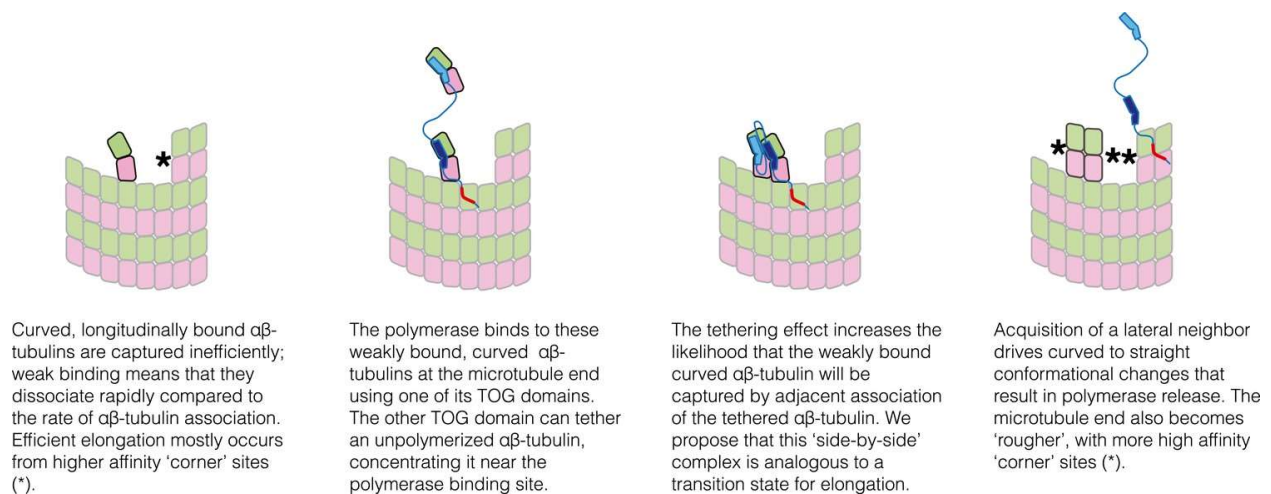


Figure 1.12: Schematic cartoons illustrating the origin of catalytic action. Figure and legend reproduced from Ayaz et al., 2014.

The microtubule end has multiple sites where $\alpha\beta$ -tubulin can associate, but elongation is largely dominated by additions into the few, high-affinity 'corner' sites (left panel) because pure longitudinal associations are weak. By preferentially recognizing curved $\alpha\beta$ -tubulin with one of its TOG domains, the polymerase (TOG domains in blue, basic region in red) can selectively localize to these 'unproductive' binding sites (second from left). The tethering action greatly enhances the rate at which these weakly bound subunits are trapped by neighboring association of another $\alpha\beta$ -tubulin (middle two panels). Polymerization-induced straightening of $\alpha\beta$ -tubulin releases the polymerase for another round of catalysis (right).

The CLASP family are MT rescue and anti-catastrophe factors

Cytoplasmic linker associated proteins (CLASPs) (Akhmanova et al., 2001; Bratman and Chang, 2007; Pasqualone and Huffaker, 1994) comprise a family of microtubule rescue factors. Multiple *in vivo* studies have demonstrated a role for CLASPs in stabilizing MTs and preventing catastrophe. During interphase, CLASP activity is important for stabilizing microtubules and promoting rescue (Mimori-Kiyosue et al., 2005; Drabek et al., 2006). Depending on the cell type, CLASPs have been shown to have slightly different functions: in neurons, they regulate MTs in synapses and growth cones and in migrating cells, they polarize the MT network [REFS from Lawrence]. During mitosis, CLASPs localize to kinetochores, where they regulate microtubule dynamics, and at the midzone, where their activity is important for stabilizing antiparallel microtubule overlaps (Inoue et al., 2004; Pereira et al., 2006; Bratman and Chang, 2007). Loss of CLASP activity leads to diminished microtubule stability, collapse of the spindle, and other aberrations (Maiato et al., 2003; Inoue et al., 2004; Maiato et al., 2005; Pereira et al., 2006; Bratman and Chang, 2007; Ortiz et al., 2009).

The effect of CLASPs on MT dynamics has been studied *in vitro* via reconstitution assays. A recent paper by Lawrence et al. 2018 demonstrated that human CLASP2 has significant effects on catastrophe and rescue (Figure 1.13). From the representative kymograph alone, addition of full-length CLASP2 causes the MT to elongate over the entire length of the movie (Figure 1.13 A) (Lawrence et al., 2018). The addition of 400 nM CLASP2 to 8 μ M mammalian tubulin decreases catastrophe by three-fold and increases rescue six-fold (Figure 1.13-B, C). No change in MT growth or shrinking rates

were observed in the presence of the CLASP2 (Lawrence et al., 2018). The effects on catastrophe and rescue are consistent with CLASPs from yeast (Clp1p, *S. pombe*) and *Drosophila* (mast/Orbit) that have also been shown to decrease the frequency of microtubule catastrophe and/or increase the frequency of microtubule rescue (Al-Bassam et al., 2010; Moriwaki and Goshima, 2016). But the effect of CLASPs on growth and shrinkage has not been as consistent. Clp1p appears to increase growth rates and decrease shrinking rates whereas Mast/Orbit strongly decreased both (Al-Bassam et al., 2010; Moriwaki and Goshima, 2016). Species variability could account for these differences but more exhaustive studies are required.

The dramatic change in transition frequencies demonstrated by addition of full-length CLASP proteins raises the question of their underlying mechanism. In order to study that, I focused on the *Saccharomyces cerevisiae* CLASP homolog, Stu1. Like Stu2, Stu1, is an essential protein in yeast (Pasqualone and Huffaker, 1994). The domain architecture of full-length Stu1 is presented in Figure 1.14. For comparison, the *S. cerevisiae* member of the polymerase family, Stu2, is also shown side by side. Stu1 contains multiple domains: two tubulin-interacting TOG domains, TOG1 (aa 1-250) and TOG2 (aa 313-567), followed by a basic region and an as-yet uncharacterized dimerization region (Figure 1.14). In general, CLASPs contain multiple TOGs with a basic region, and a dimerization element, all of which collectively determine activity (Al-Bassam et al., 2010; Patel et al., 2012; Leano et al., 2013; Funk et al., 2014) (Figure 1.9 B). In addition, CLASPs interact with other MAPs including end-binding proteins such as EB1 (Figure 1.9 B). The effect of human CLASP2 in suppressing MT catastrophe and

promoting MT rescue is greatly enhanced by the presence of EB1 that is believed to help localize the CLASP to the tip of the MT (Lawrence et al., 2018)

How the domain composition and organization of CLASPs determine activity remains largely unknown, but multiple studies indicate that the tubulin-binding activity of CLASP TOGs is essential (Al-Bassam et al., 2010; Patel et al., 2012; Leano et al., 2013; Funk et al., 2014). Structures of CLASP TOGs indicate preservation of the paddle-shaped HEAT-repeat model. However, the interhelical loops that form the TOG:tubulin interface identified in polymerase TOGs are not arranged as in the polymerase TOGs (Leano et al., 2013; Majumdar et al., 2018). I discuss the structure of the CLASP TOGs in general and Stu1 TOG2 in particular further in Chapter 2.

Remarkably, isolated CLASP TOGs are able to recapitulate the activity of the full-length protein in suppressing catastrophe and increasing rescue. This has been demonstrated by very recently published work by our lab (my paper) and by the Akhmanova lab (Aher et al., 2018; Majumdar et al., 2018). This activity is very unlike the polymerase TOGs. Isolated polymerase TOGs are not polymerases themselves and the mechanism for polymerase activity on the basis of the unique properties of their TOGs is described in the following section. That such a small domain is single-handedly capable of producing these effects on MT dynamics is unexpected and raises many questions on the molecular basis of CLASP activity as well as the overall mechanism of catastrophe and rescue. I dive into these topics further in the Discussion section of Chapter 3 and the culminating Chapter 4.

My thesis project: elucidating the role of the CLASP TOGs

In subsequent chapters, I explain how I used a combination of biochemical, structural, and reconstitution studies to gain insight into the role of TOG domains in CLASP function. Using the TOG1 and TOG2 domains from Stu1, the *S. cerevisiae* CLASP, I found that only Stu1-TOG2 displays appreciable tubulin-binding activity (1.68 μM affinity), and that Stu1-TOG2 can also bind to microtubules (12 μM affinity). A crystal structure of Stu1-TOG2 revealed a conserved CLASP-specific residue positioned to interact with $\alpha\beta$ -tubulin, likely conferring distinctive tubulin-binding properties to CLASP-family TOGs. In reconstitution assays the isolated Stu1-TOG2 domain potently suppressed microtubule catastrophe and stimulated microtubule rescue. Observing these activities from an isolated TOG domain contradicts the expectation that an array of TOGs would be required to recapitulate the catastrophe suppressing and rescue promoting activity of CLASPs. Stu1-TOG2 had little, if any, effect on microtubule growing or shrinking rates, so the observed changes in catastrophe and rescue frequencies are not an indirect consequence stemming from altered kinetics of microtubule growing or shrinking. Stu1-TOG2 also did not detectably increase the number of stabilizing cap sites as detected by Bim1-GFP binding, which suggests that it did not act by reducing GTPase activity in the microtubule lattice. I speculate that Stu1-TOG2 binding to the microtubule tip directly influences the switching propensities there. (Majumdar et al., 2018)

These results demonstrate that a single CLASP-family TOG can suppress catastrophe and promote rescue, without needing to be part of a linked array. These unexpected properties of Stu1-TOG2 provide new insight into the molecular origin of CLASP activity,

diversify the understanding of TOG function, and may have implications for other TOG-containing regulatory factors. (Majumdar et al., 2018)

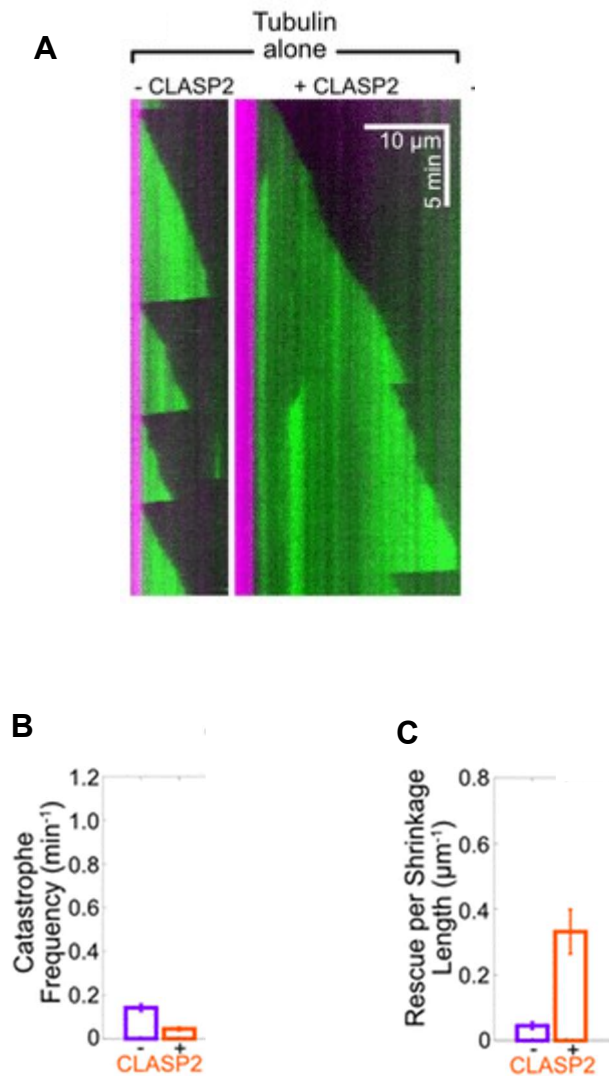


Figure 1.13: CLASP2 γ suppresses catastrophe and promotes rescue. Figure and legend reproduced from Lawrence 2018 with modifications.

Representative kymographs of microtubules grown with 8 μM Alexa 488-labeled tubulin alone and in the presence of 400 nM CLASP2 γ (A).

The addition of 400 nM CLASP2 γ to 8 μM tubulin (A) resulted in more than a threefold suppression of microtubule catastrophe, from $0.14 \pm 0.02 \text{ min}^{-1}$ (SE, $N = 73$) to $0.04 \pm 0.01 \text{ min}^{-1}$ (SE, $N = 26$; B), and a strong promotion of microtubule rescue, from $0.05 \pm 0.01 \mu\text{m}^{-1}$ (SE, $N = 17$) to $0.33 \pm 0.07 \mu\text{m}^{-1}$ (SE, $N = 25$) rescues per shrinkage length (C).

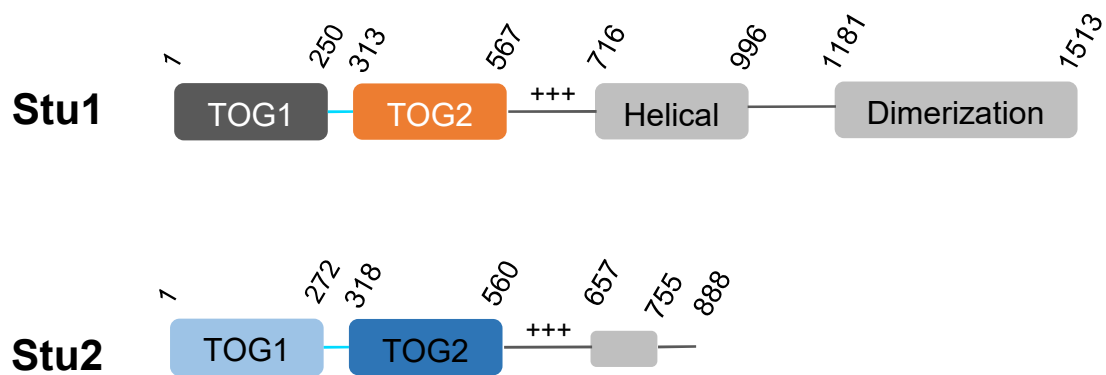


Figure 1.14: Domain organization of yeast proteins Stu1 and Stu2 based on our studies and on (Funk *et al.*, 2014). Numbers indicate the amino acid boundaries of the different domains. Stu1 figure and legend reproduced from Majumdar 2018.

CHAPTER TWO: STRUCTURE & BIOCHEMISTRY

Reproduced from Majumdar et. al 2018 with minor modifications (excluding Abstract and Discussion sections)

Abstract

In order to gain insight into the role of TOGs in CLASP activity, I conducted biochemical and structural studies on the isolated TOG1 and TOG2 domains of the *S. cerevisiae* CLASP Stu1. Unlike the polymerase TOGs, the binding affinity and conformational preference of CLASP TOGs had not yet been defined. I looked at the binding affinity of the Stu1 TOGs to unpolymerized tubulin and to stabilized microtubules to determine conformational preference. I discovered that only Stu1-TOG2 has an appreciable tubulin-binding affinity (1.68 μM , determined by sedimentation velocity analytical ultracentrifugation) along with the ability to bind microtubules (12 μM , determined by total internal reflection fluorescence microscopy). In contrast to Stu1 TOG2, Stu1 TOG1 does not have appreciable binding to either tubulin or microtubules.

Next, I determined the crystal structure of Stu1 TOG2, thereby identifying a CLASP-specific residue that is conserved in CLASP-family TOG2 domains. This arginine is uniquely positioned to interact with β -tubulin and could potentially confer distinctive binding properties to CLASP TOGs.

The Stu1 TOG2 structure also shows that a part of the linker between TOG1 and TOG2 is docked onto the side of the TOG2 domain proper as an additional helix. This indicates that the two Stu1 TOGs are nearer each other than the two Stu2 TOGs, a prediction that is backed up by analysis of the TOG1-TOG2 fragments of Stu1 vs. Stu2 using limited proteolysis and small-angle X-ray scattering.

Taken together, the structural and biochemical studies indicated that the isolated Stu1-TOG2 domain, with its tubulin and microtubule binding properties and a CLASP-specific residue, might be key to CLASP activity. I explore this further in Chapter 3.

Results

Construct design

The constructs I used for the isolated domains Stu1-TOG1 and for Stu1-TOG2 are shown in Figure 2.1. Stu1-TOG1 is 267 residues and Stu1-TOG2 is 317 residues long. Each domain includes segments of the sequence that links TOG1 to TOG2 in the intact protein. Expressing more minimal fragments of either domain yielded insoluble or otherwise poorly-behaved protein. An example of one of these versions of TOG2 is shown in Figure 2.2. Efforts to resolubilize this particular version included optimizing expression host, induction temperature and time, and buffer conditions as well as using the purified post-lysis insoluble fraction for unfolding and refolding experiments using urea and guanidine hydrochloride. More minimal versions of TOG1 were not as recalcitrant as TOG2 but showed formation of soluble aggregates as analyzed by gel-filtration and sedimentation velocity experiments (data not shown).

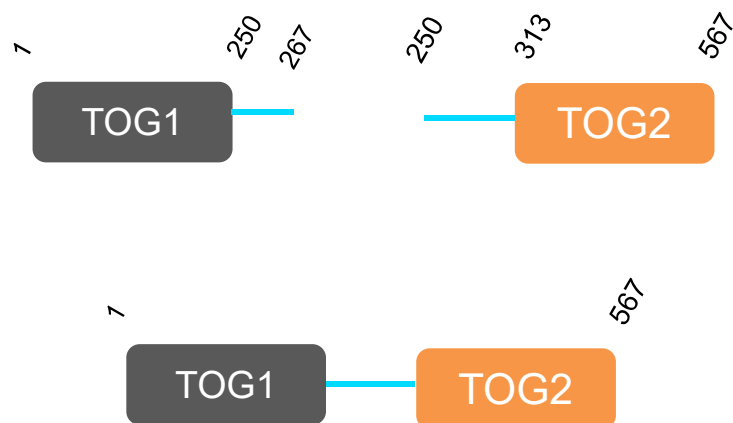


Figure 2.1: Schematics of expression constructs used for Stu1-TOG1 and Stu1-TOG2. Figure and legend reproduced from Majumdar et. al. 2018.

For each TOG, it was necessary to include elements from the linker sequence to obtain soluble, well-behaved protein. The TOG1-TOG2 construct we used encompasses residues 1-567.

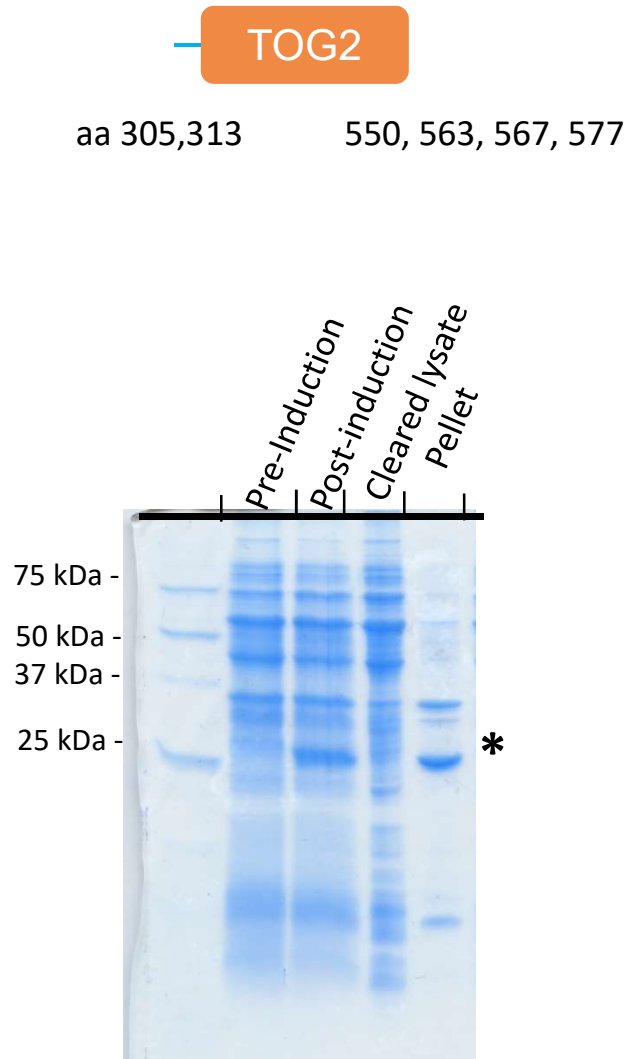


Figure 2.2: Minimal TOG2 construct sequestered into insoluble fraction post-lysis

(Top) Schematic of minimal TOG2 constructs (not including the full linker sequence) that were generated

(Bottom) Minimal TOG2 constructs are insoluble. Example gel showing expression of the most minimal TOG2 construct (313-567, 23 kDa) with a distinct post-induction protein band of ~25 kDa. After lysis, this band is no longer in the cleared lysate and entirely in insoluble pellet. * marks the TOG2 protein band.

Tubulin and microtubule binding properties of the Stu1 TOGs

Polymerase-family TOGs like Stu2-TOG1 and Stu2-TOG2 bind tightly to the curved conformation of $\alpha\beta$ -tubulin but do not bind appreciably to the straight conformation (Ayaz et al., 2012, 2014). The conformational preference of CLASP-family TOGs has not yet been defined. I used analytical ultracentrifugation and microtubule co-sedimentation assays to begin investigating the tubulin- and microtubule-binding properties of the Stu1 TOG domains.

Stu1-TOG1 did not bind appreciably to $\alpha\beta$ -tubulin: there was little, if any, change in the sedimentation behavior of $\alpha\beta$ -tubulin when it was mixed with TOG1 (Figure 2.3; 0.6 μM $\alpha\beta$ -tubulin and 3 μM Stu1-TOG1), a finding consistent with previous work (De la Mora-Rey et al., 2013; Funk et al., 2014). By contrast, Stu1-TOG2 formed a complex with unpolymerized $\alpha\beta$ -tubulin: the TOG2+ $\alpha\beta$ -tubulin mix showed a clear shift to larger sedimentation coefficients compared to TOG2 or $\alpha\beta$ -tubulin alone (Figure 2.3; 0.6 μM $\alpha\beta$ -tubulin and 3 μM Stu1-TOG2). Previously, our lab showed that polymerase TOGs (Stu2-TOG1 and Stu2-TOG2) each bind with comparable affinity to unpolymerized tubulin (Ayaz et al., 2014); a representative experiment from (Ayaz et al., 2014) showing this interaction is reproduced in Figure 2.3 (0.3 μM $\alpha\beta$ -tubulin and 7 μM Stu2-TOG2). The lack of tubulin-binding we observed for Stu1-TOG1 is consistent with a prior study that used co-purification and gel-filtration to examine tubulin-binding by the isolated Stu1 TOGs (Funk et al., 2014).

Stu1-TOG1 and Stu1-TOG2 also differed in their microtubule-binding properties (Figure 2.4; experiments used 3 μM $\alpha\beta$ -tubulin and 9 μM of the candidate interaction partner). Stu1-TOG1 did not appreciably co-sediment with pre-formed microtubules, indicating

that it binds weakly, if at all, to the microtubule lattice (see also Figure 2.7). On the other hand, some Stu1-TOG2 co-sedimented with pre-formed microtubules, indicating that Stu1-TOG2 can bind the microtubule lattice in addition to being able to bind unpolymerized tubulin. This ability of Stu1-TOG2 to interact with both unpolymerized tubulin and with microtubules contrasts with polymerase-family TOGs like Stu2-TOG1 and Stu2-TOG2. Indeed, those polymerase TOGs do not bind microtubules and actually induce microtubule depolymerization because they so strongly prefer the curved conformation of tubulin (Figure 2.4, starred lane; depolymerization induced by a polymerase TOG domain has been described in (Ayaz et al., 2014; Geyer et al., 2015)). Thus, Stu1-TOG2 has different conformation-selectivity compared to polymerase TOGs: while Stu1-TOG2 can bind to unpolymerized tubulin (presumably in its curved conformation), it can also bind to microtubules, where the tubulin is straight. Not observing microtubule depolymerization in co-sedimentation assays using Stu1-TOG2 suggests that Stu1-TOG2 does not prefer curved tubulin as strongly as the polymerase TOGs, and/or that Stu1-TOG2 binds less tightly to curved tubulin.

I used sedimentation velocity analytical ultracentrifugation, microscale thermophoresis, and fluorescence microscopy assays to obtain more quantitative insight into the tubulin and microtubule binding affinities of the Stu1-TOG1 (Figure 2.5, 2.6, 2.7). Adding Stu1-TOG1 at concentrations as high as 24 μM did not change the sedimentation coefficient of the reaction boundary (Figure 2.5; 0.6 μM $\alpha\beta$ -tubulin was used), indicating that the TOG1 domain interacted very weakly, if at all, with unpolymerized tubulin. By contrast, adding Stu1-TOG2 resulted in the formation of a faster sedimenting species (Figure 2.5), reflecting a binding interaction between Stu1-TOG2 and $\alpha\beta$ -tubulin. The binding

isotherm fails to saturate even at a ~300-fold excess of Stu1-TOG2 over $\alpha\beta$ -tubulin. I speculate that this lack of saturation indicates the formation of an oligomeric species with a high-molecular weight in addition to a 1:1 Stu1-TOG2: $\alpha\beta$ -tubulin complex (see Chapter 4 for “curls” observed in samples with a stoichiometric amount of Stu1-TOG2 and $\alpha\beta$ -tubulin using cryoelectron microscopy). Multi-signal sedimentation velocity experiments performed with Stu1-TOG1-TOG2 previously indicated that the main species formed in these binding assays is a 1:1 Stu1: $\alpha\beta$ -tubulin complex (data not shown). In order to obtain a binding affinity that is more representative of a 1:1 complex, I fit the titration to a single-site binding model after excluding the high-concentration data points that failed to show saturation (see Methods for details about the fitting; thank you to Dr. Chad Brautigam, Director of the Macromolecular Biophysics Resource facility). I obtained a dissociation constant of 1.68 μM for the Stu1-TOG2: $\alpha\beta$ -tubulin interaction. I also used microscale thermophoresis to measure the binding affinity in an independent way, obtaining an affinity of 2.6 μM (Figure 2.6). A similar lack of saturation was also observed when titrating Stu1-TOG1-TOG2 against $\alpha\beta$ -tubulin, and similar treatment yielded a binding affinity of 720 nM by analytical ultracentrifugation, so approximately two-fold tighter than TOG2 (Figure 2.8). Microscale thermophoresis data for Stu1-TOG1-TOG2 indicated an even higher affinity at 130 nM (Figure 2.8) which may mean the effect of the aberrant behavior is still pronounced in the AUC data.

Next, I used TIRF microscopy to quantify microtubule binding affinity. Adding Alexa-488-labeled Stu1-TOG1 or Stu1-TOG2 or Stu1-TOG1-TOG2 to ReAsH-labeled yeast microtubules attached to a coverslip yielded dose-dependent increases in TOG fluorescence along the microtubules (Figure 2.7, 2.8). Quantifying the dose-dependence

of this behavior yielded microtubule-binding affinities for Stu1-TOG1 and Stu1-TOG2 of 40 and 12 μM , respectively (Figure 2.7). The analysis and fitting of the acquired data was carried out by Tae Kim.

The binding experiments reveal marked differences between the Stu1-TOG domains. Whereas Stu1-TOG1 binds very weakly to unpolymerized tubulin (estimated $> 300 \mu\text{M}$ affinity) or microtubules ($\sim 40 \mu\text{M}$ affinity), Stu1-TOG2 binds with moderate affinity to both ($\sim 2 \mu\text{M}$ affinity for tubulin, $\sim 12 \mu\text{M}$ affinity for microtubules). Thus, compared to the polymerase TOGs from Stu2 (Ayaz *et al.*, 2014), the CLASP TOG Stu1-TOG2 binds ~ 10 -fold less tightly to unpolymerized tubulin, without a strong preference for unpolymerized over polymerized tubulin.

The disassociation constants for Stu1-TOG1, TOG2, and TOG1-TOG2 to tubulin and the MT lattice are summarized in Table 1.

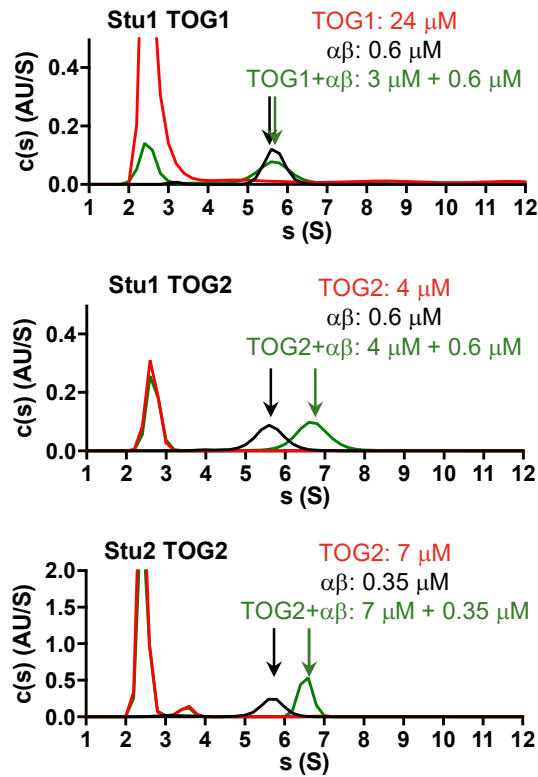


Figure 2.3: Tubulin binding of Stu1-TOGs analyzed by sedimentation velocity analytical ultracentrifugation. Figure and legend reproduced from Majumdar et. al. 2018.

$c(s)$ distributions (signal population as a function of s) for TOG only (red), tubulin only (black), and a TOG:tubulin mix (green) are shown in each panel. Stu1-TOG1 binds weakly, if at all to tubulin (top). Stu1-TOG2 binds tubulin and forms a faster-sedimenting complex (middle). For comparison, the tubulin interactions of Stu2-TOG2 are illustrated (bottom; these data were originally presented in (Ayaz *et al.*, 2014); the y-axis signal is higher because these data were collected using a shorter wavelength to monitor the sedimentation). These $c(s)$ distributions are taken from a single trial; two or more trials gave consistent results (not shown). Figure 2.5 shows results from titrations.

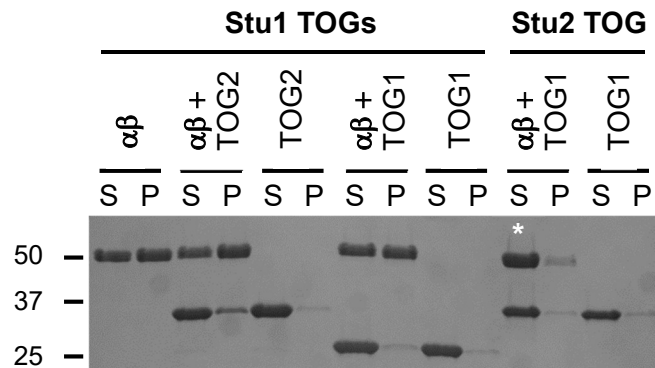


Figure 2.4: Microtubule binding analyzed by co-sedimentation. Figure and legend reproduced from Majumdar et. al. 2018.

S, supernatant; P, pellet. A fraction of Stu1-TOG2 co-sediments with microtubules, indicating some binding; no co-sedimentation is observed for Stu1-TOG1 or for Stu2-TOG1, which is shown to provide a comparison with polymerase TOGs. The white * is to draw attention to the increased tubulin in the supernatant fraction with Stu2-TOG1, which actually depolymerizes the stabilized microtubules because of its preference for curved $\alpha\beta$ -tubulin. Experiment was repeated 3 times (other trials not shown).

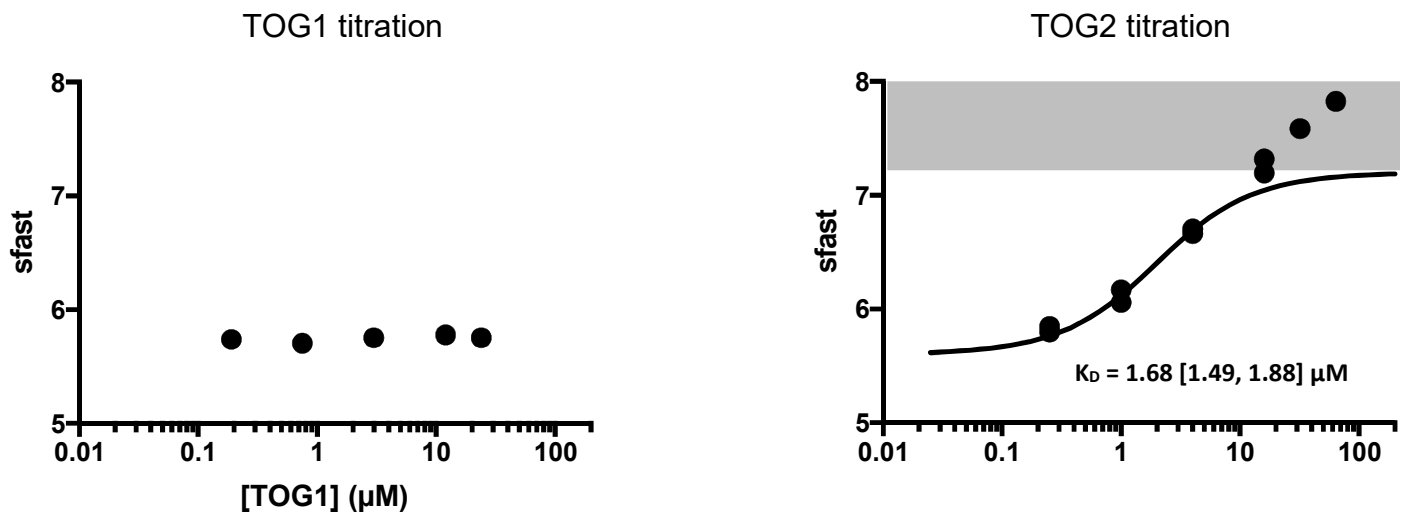


Figure 2.5: Binding affinities of Stu1 TOGs to unpolymerized tubulin.

Figure and legend reproduced from Majumdar et. al. 2018.

Binding isotherms of TOG:tubulin interaction for TOG1 (left) and TOG2 (right) plotting s_{fast} against $[TOG]$. No change in s_{fast} was observed with increasing concentrations of Stu1-TOG1, indicating very weak or no binding (N=1 titration). Dose-dependent increases in s_{fast} were observed for TOG2 (N=2 titrations; data from both are shown). The low concentration region of the titrations is consistent with a one site binding reaction, but the titrations reproducibly fail to saturate at high concentrations. To extract the apparent binding constant from the low concentration region, we excluded data where s_{fast} exceeded 7.2 S (shaded area; 7.2 S is the theoretical maximum S for a 1:1 complex of Stu1-TOG and tubulin, see Methods and see Sup. Fig. 2 for a complementary binding assay). This yielded an apparent $K_D = 1.68 [1.49, 1.88] \mu M$. Tubulin concentration in all samples is $0.6 \mu M$. TOG1 concentrations used were 0.19, 0.75, 3, 12, 24 μM and TOG2 concentrations for both titrations were 0.25, 1, 4, 16, 64 μM and 0.25, 1, 4, 16, 64 μM .

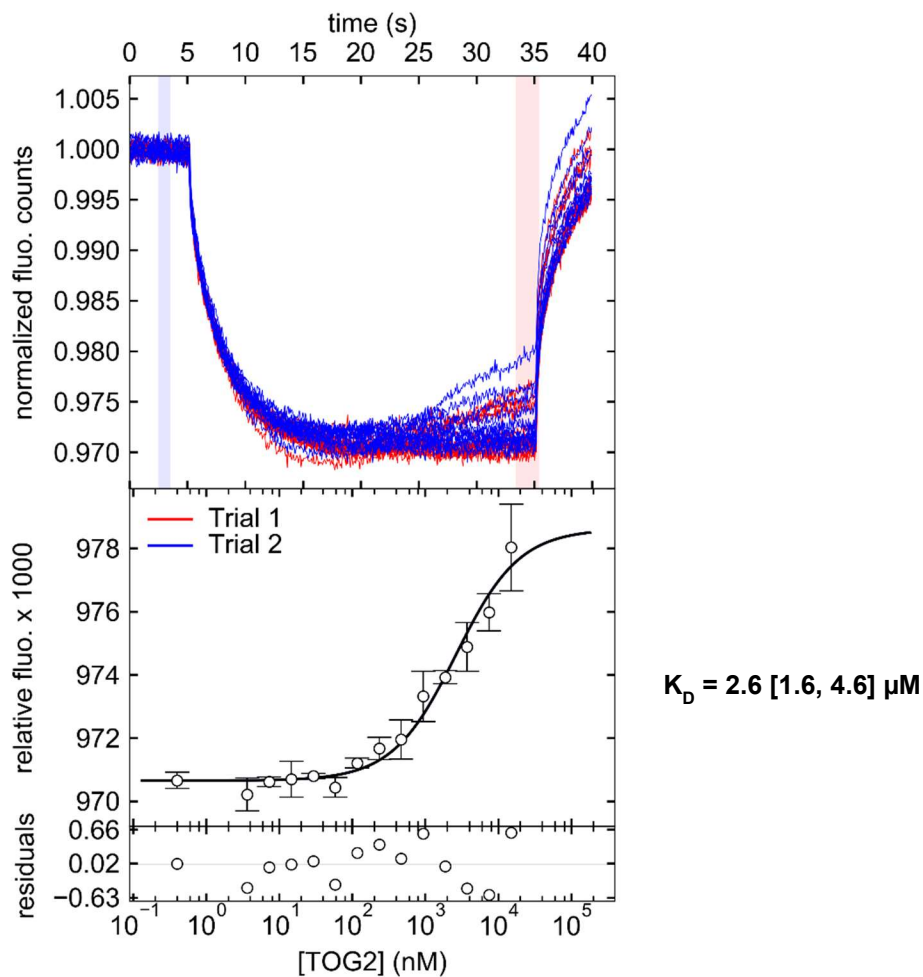


Figure 2.6: Affinity of TOG2 to unpolymerized tubulin determined by MST. Figure and legend reproduced from Majumdar et. al. 2018.

Binding of TOG2 to unpolymerized tubulin analyzed by microscale thermophoresis. [Tubulin] in all samples was 40 nM and TOG added in a 15-point 1:1 dilution series with highest concentration at 120 μ M. Normalized fluorescence scans for different TOG concentrations show changes in fluorescent counts over time showing pre-IR, IR-on and post-IR phases (top panel). Aberrant thermophoresis was detected for high [TOG2] samples and excluded from the binding isotherm (not shown). The data showing relative change in fluorescence versus protein concentration fit well to a single-site binding model (bottom panel), yielding $K_D = 2.6 \mu$ M.

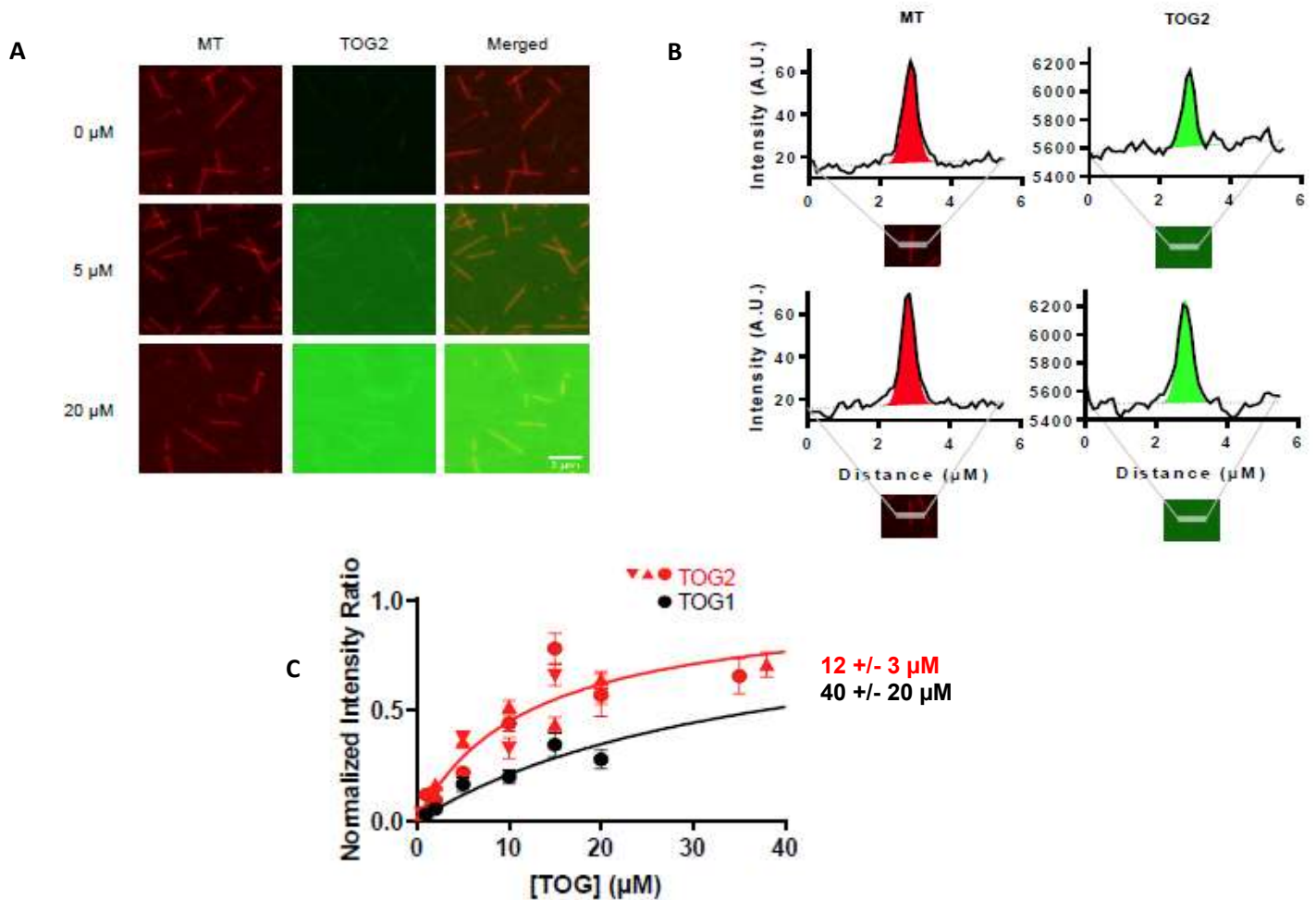


Figure 2.7: Binding affinities of Stu1 TOGs to microtubule lattice. Figure and legend reproduced from Majumdar et. al. 2018.

A. Representative images from a TIRF microscopy based microtubule-binding assay using ReAsH-labeled yeast MTs (left column, red) and Alexa-488-labeled Stu1-TOG2 (middle column, green); merged images are shown in the right column.

B. Quantification of fluorescence intensity. Intensity values from 4-pixel wide line-scans perpendicular to MTs, are plotted as the solid curves. These curves were fit with a Gaussian (to quantify the peak height and intensity; colored region) plus a line (to model uneven background intensity; dotted line). Intensity of MTs shown in red, TOG2 in green.

C. Results of the binding titrations for Stu1-TOG constructs on MT lattice. We performed a normalization (see Methods) to account for day-to-day variations in labeling stoichiometry or laser intensity. $n = 15$ scans per concentration for each of 3 independent titrations for Stu1-TOG2 (red; different symbols for the three titrations); $n = 15$ scans per concentration for a single Stu1-TOG1 titration (black). The fitted dissociation constants are $40 \pm 20 \mu\text{M}$ and $12 \pm 3 \mu\text{M}$ for Stu1-TOG1 and Stu1-TOG2, respectively. Error bars represent SEM. Concentration of TOGs for all titrations were 0.5, 1, 2, 5, 10, 15, 20 μM . Two additional concentrations of TOG2 at 35 and 38 μM were also included

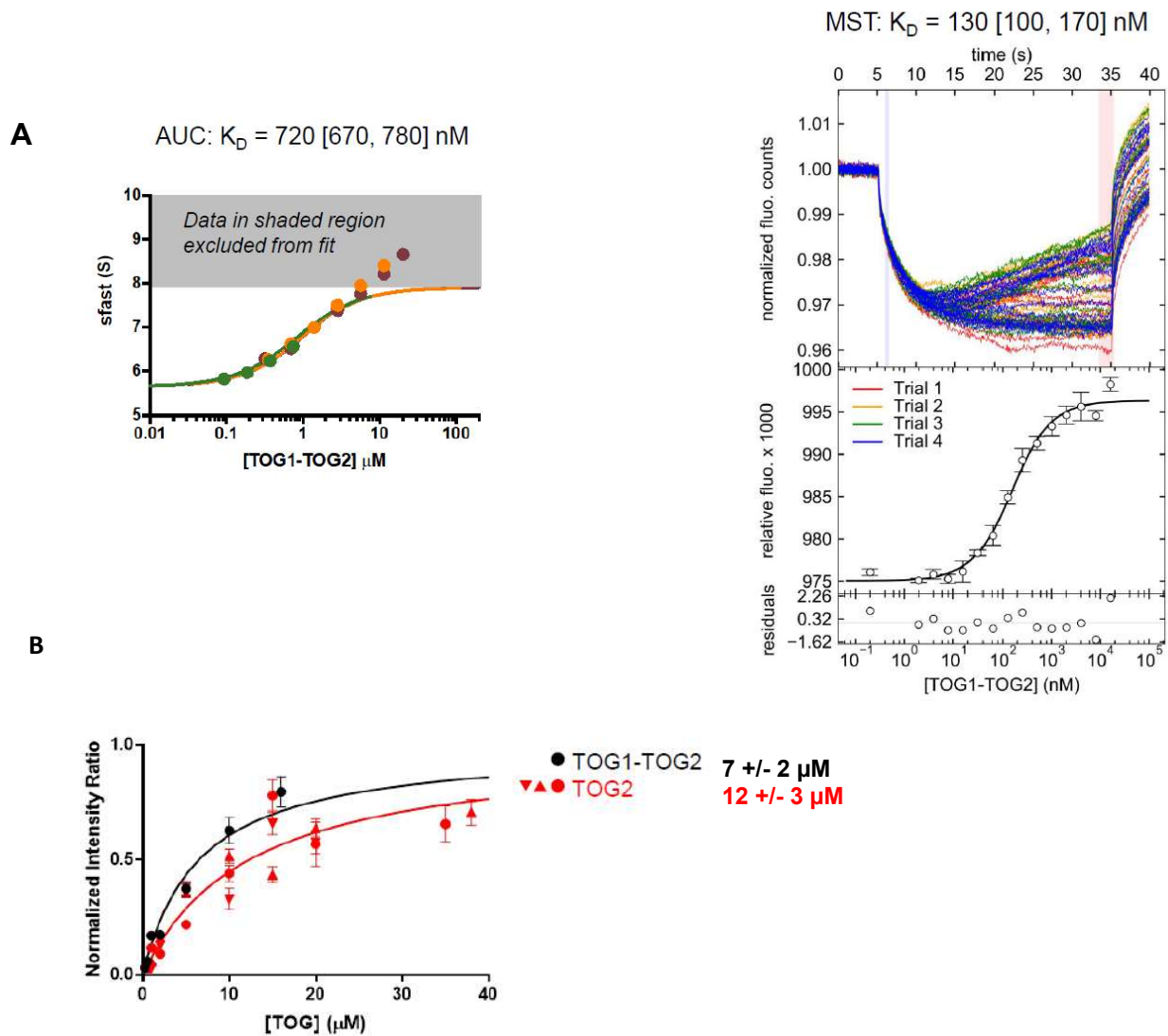


Figure 2.8: Stu1-TOG1-TOG2's affinity for tubulin and MT lattice. Figure and legend reproduced from Majumdar et. al. 2018.

A. TOG1-TOG2 binds to unpolymerized tubulin with a greater affinity than TOG2: as measured by AUC (left panel) and MST (right panel). Data showed aberrant behavior at high [TOG] similar to that described in Figure 2 and Supplemental Figure 2 and thus, high [TOG] datapoints were excluded. For the AUC data plot, we used a 9.3 s sedimentation coefficient for TOG1-TOG2:tubulin complex. Tubulin concentrations in samples for each titration were: 0.25 μM (green titration), 0.5 μM (orange), 0.5 μM (burgundy). TOG1-TOG2 concentrations were 0.09, 0.19, 0.38, 0.75 μM (green titration); 0.35, 0.7, 1.4, 2.8, 5.6, 11.2 μM (orange); and 0.32, 0.7, 2.8, 5.6, 11.2, 20 μM (burgundy).

B. Binding of TOG1-TOG2 (black) to the MT lattice quantified similar to Figure 2.7 Data for TOG2 (red) reproduced from Figure 2.7 for comparison. TOG1-TOG2 binds with about two-fold greater affinity to the lattice than TOG2: Normalized intensity versus concentration (top panel) and binding affinities (bottom table). Concentrations of TOG1-TOG2 were 0.5, 1, 2, 5, 10, 16 μM .

Table 1. Summary of measured tubulin and microtubule binding affinities for Stu1-TOG1, Stu1-TOG2 and Stu1-TOG1-TOG2

	K_D	
	Tubulin	MT
TOG1	--	$40 \pm 20 \mu\text{M}$
TOG2	$1.68 \mu\text{M}$ [1.49, 1.88]	$12 \pm 3 \mu\text{M}$
TOG1-TOG2	720 nM [670-780]	$7 \pm 2 \mu\text{M}$

Structure of the TOG2 domain from Stu1

Different conformation-selectivity for CLASP-family TOGs might result because in these TOGs the structural arrangement of tubulin-binding residues differs from that in polymerase-family TOGs (Ayaz et al., 2012, 2014; Leano et al., 2013; Maki et al., 2015; Slep and Vale, 2007 and next section). To obtain insight into the structural features that may underlie the tubulin-binding properties of Stu1-TOG2, we determined the structure of Stu1-TOG2 to 1.89 Å resolution using X-ray crystallography. I was unable to crystallize Stu1-TOG1. The structure of Stu1-TOG2 was phased using a Tantalum bromide cluster after attempts at molecular replacement only yielded weak solutions that were difficult to advance (not shown). The experimental phases were of high quality, and the model was autobuilt using HKL3000 (Minor et al., 2006) followed by cycles of manual rebuilding and refinement. The refined structure has $R^{\text{work}}/R^{\text{free}}$ values of 17.3% / 21.2% and good geometry (98.5% of residues in the most favored regions of a Ramachandran plot, Molprobit (Chen et al., 2010) score 1.19 (99th percentile)) (Table 2).

The overall structure of Stu1-TOG2 (Figure 2.9) shows the characteristic, paddle-like arrangement of helical hairpins that has been observed in numerous other polymerase- and CLASP-family TOGs (Al-Bassam et al., 2007; Ayaz et al., 2012, 2014; Byrnes and Slep, 2017; Fox et al., 2014; Howard et al., 2015; Leano et al., 2013; Slep and Vale, 2007). Prior structures of other CLASP-family TOGs revealed an ‘arched’ configuration of the long and narrow tubulin binding interface (Leano *et al.*, 2013; Maki *et al.*, 2015), which in polymerase-family TOGs typically adopts a flatter configuration (Figure 2.10). The spatial arrangement of presumptive tubulin-binding residues in these CLASP-family

TOGs is distinct from that observed in polymerase TOGs (Ayaz *et al.*, 2012; 2014). The structure of Stu1-TOG2 (Figure 2.9) does not share the arched arrangement previously observed for vertebrate CLASP-family TOGs: instead, Stu1-TOG2 presents a flatter tubulin-binding interface (Figure 2.9, bottom panel; Figure 2.10). Stu1-TOG2 shows comparable structural similarity to a CLASP-family TOG2 domain (2.6 Å C α rms coordinate deviation to hCLASP1-TOG2 (Leano *et al.*, 2013), the TOG2 domain from the human CLASP1 isoform) as it does to a polymerase TOG (2.5 Å C α rms coordinate deviation to Stu2-TOG2 (Ayaz *et al.*, 2014)) (Figure 2.9, table). By contrast, vertebrate CLASP-family TOG2 domains show larger structural differences when compared to a polymerase TOG (3.5 Å C α rms coordinate deviation to Stu2-TOG2).

One notable feature of the Stu1-TOG2 structure is an additional α -helix positioned along one face of the domain. This helix, colored cyan in Fig. 3, forms part of the linker sequence that connects TOG1 to TOG2 in the intact protein. Analogous 'linker docking' was also observed in structures of vertebrate CLASP-family TOGs (Leano *et al.*, 2013; Maki *et al.*, 2015), but in those cases the docking occurs in a different place on the TOG (Figure 2.9, bottom panel, magenta) and uses a distinct set of linker residues that are not conserved in fungal CLASPs like Stu1 (not shown). The presence of this interaction with the linker probably explains why we were unable to purify well-behaved constructs of Stu1-TOG2 that lacked elements from the preceding linker. That both vertebrate and fungal CLASP-family TOGs show docked linkers may indicate that keeping TOG1 and TOG2 close to each other is important for some aspect of CLASP function.

As described in the preceding section, TOG1 and the shortened linker might influence the activity of TOG2. Even though Stu1-TOG1 by itself does not bind appreciably to $\alpha\beta$ -

tubulin or microtubules (Figures 2.3, 2.4, 2.5), its presence in Stu1-TOG1-TOG2 modestly increased $\alpha\beta$ -tubulin and microtubule binding affinity compared to Stu1-TOG2 (Figure 2.8, Table 1).

A perplexing feature of prior vertebrate CLASP-family TOG structures has been that a conserved Tryptophan residue implicated in tubulin binding appears to be positioned differently than it is in polymerase-family TOGs like Stu2-TOG1 and Stu2-TOG2 ((Leano *et al.*, 2013; Maki *et al.*, 2015); see also Figures 2.9 and 2.10); based on this structural difference it has been speculated that CLASP-family TOGs prefer to interact with a hyper-curved conformation of tubulin (Leano *et al.*, 2013). In our structure of Stu1-TOG2, we observe a similar ‘repositioning’ of the presumptive tubulin-contacting tryptophan (Figure 2.9 bottom). However, we noticed that R386, which is highly conserved in the CLASP-family (Figure 2.11), packs against this tryptophan and mostly fills the space that the tryptophan normally occupies in the polymerase TOGs (Figure 2.11). Prior structures of vertebrate CLASP-family TOG2 domains (Leano *et al.*, 2013; Maki *et al.*, 2015) show the same positioning of this CLASP-family-specific Arginine (not shown). Thus, it appears that in CLASPs the conserved tryptophan may not directly contact tubulin. Instead, the CLASP-family-specific Arginine probably contacts tubulin, thereby conferring distinctive tubulin binding properties via a more polar interaction surface. I test the functional importance of this residue in Chapter 3.

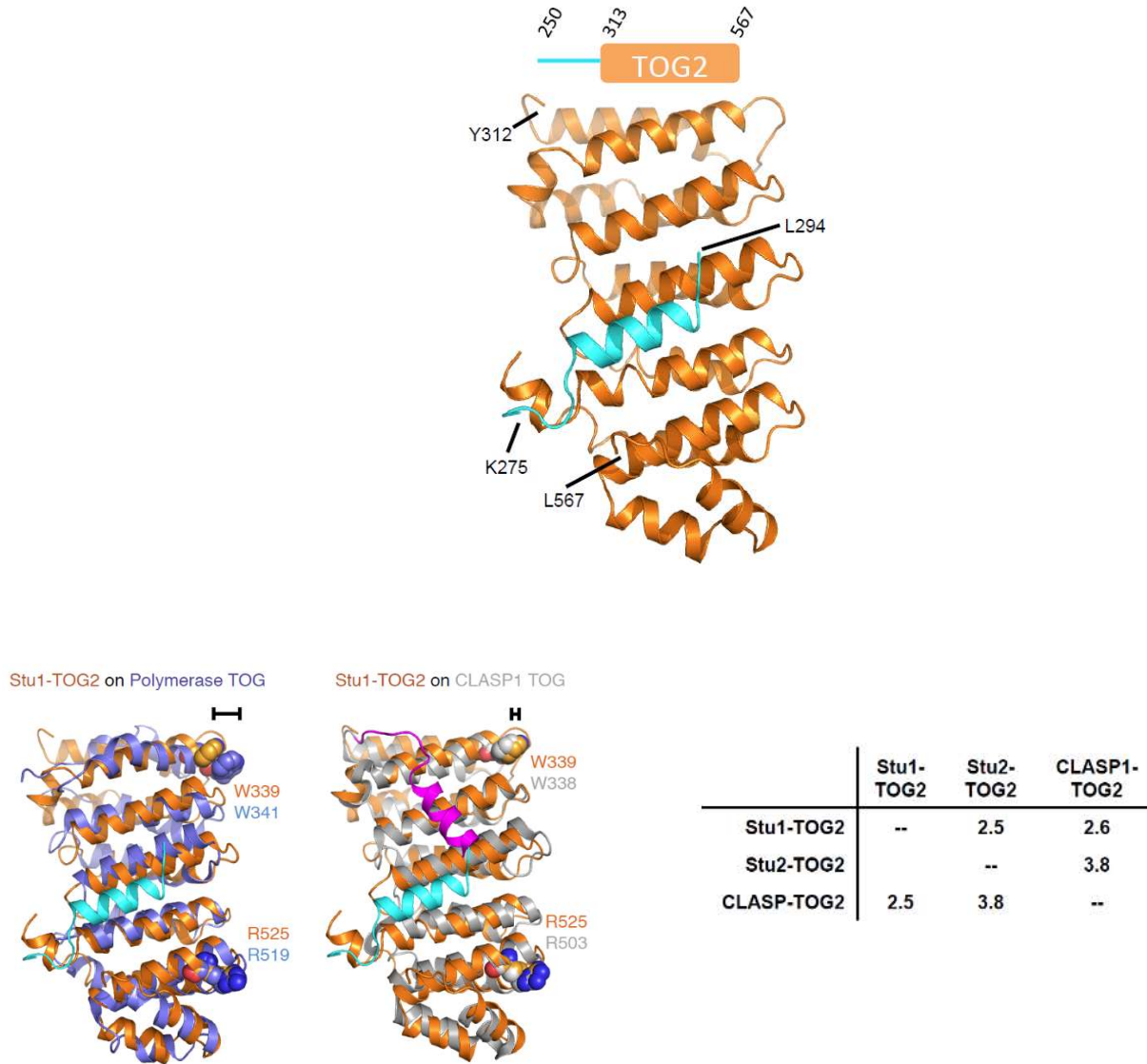


Figure 2.9: Crystal structure of Stu1-TOG2. Figure and legend reproduced from Majumdar et. al. 2018.

(Top). Cartoon representation of the TOG2 structure (orange; the linker sequences are in cyan). Inset shows the construct crystallized (repeated from Figure 2.1).

(Bottom). Rigid body superpositions of Stu1-TOG1 (orange; docked linker cyan) onto a polymerase TOG (left, Stu2-TOG2, slate) or a CLASP TOG (right, CLASP1-TOG2, grey; docked linker magenta). Conserved Arg and Trp residues implicated in tubulin-binding are shown as spheres and colored to match their respective TOG. The different length brackets illustrate the difference in positioning of the conserved Tryptophan. C α rms coordinate deviation values for the superpositions are presented in the table on the right.

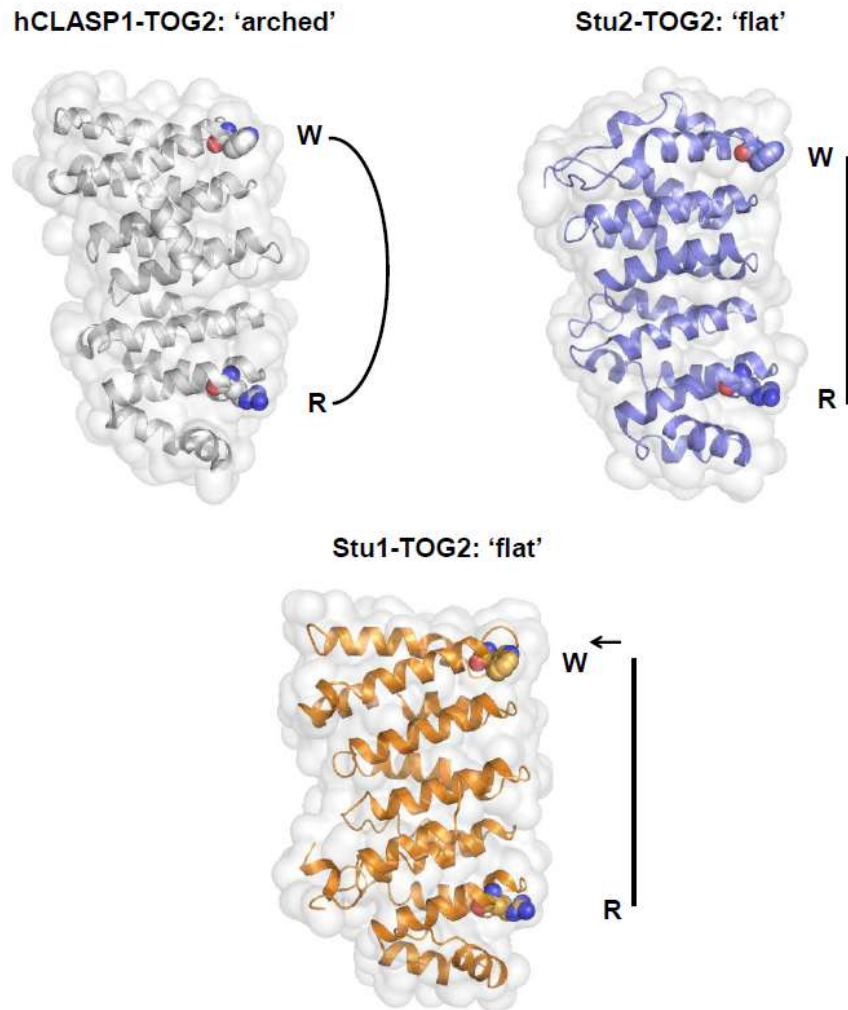


Figure 2.10: Comparing Stu1-TOG2 to 'arched' and 'flat' TOG domains. Figure and legend reproduced from Majumdar et. al. 2018.

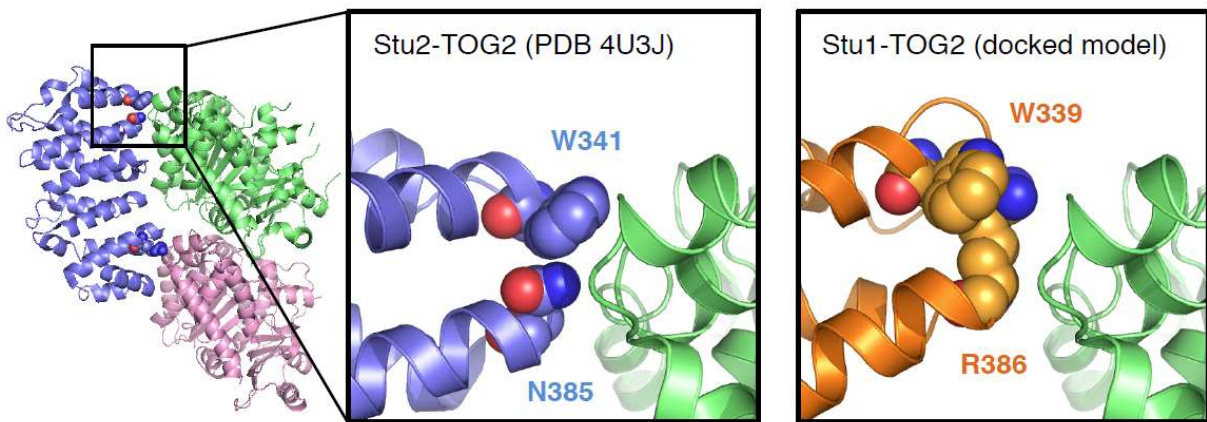
Different configurations of the tubulin-binding interface on selected TOG domains. In each panel a cartoon representation of a given TOG is shown inside of its solvent-accessible surface (transparent grey). Evolutionarily conserved W,R residues implicated in tubulin binding are shown in space-filling representation at the 'top' and 'bottom' of the tubulin binding surface. Line drawings emphasize the shape of the tubulin-binding surface and the important W,R residues. Stu1-TOG2 does not show the 'arched' configuration observed for hCLASP1. The arrow on the Stu1-TOG2 panel indicates the 'retraction' of the conserved Tryptophan.

Top left: CLASP-family TOG: hCLASP1, PDB code 4K92, grey.

Top right: polymerase-family TOG: Stu2-TOG2, PDB code 4U3J, blue.

Bottom: CLASP-family TOG: Stu1-TOG2, PDB code 6COK, this study, orange.

A



B

	339	386	
<i>S. cerevisiae</i>	...TEQN W KLRQ....	TSSL R TTLS...	CLASPs
<i>S. pombe</i>	...TEQN W SVRQ....	LLSL R TTLS...	
<i>D. melanogaster</i>	...KNAD W EKRV....	KEEL R SOVI...	
<i>A. thaliana</i>	...PEKD W SMRI....	LADRR R STIV...	
<i>X. leavis</i>	...DKHD W EQRI....	AKDL R SOVV...	
<i>H. sapiens</i>	...DHKD W SMRV....	AKDL R SOVV...	
<i>S. cerevisiae</i>	...TSSK W KDRV....	QKDAN I QAV...	Polymerases
<i>S. pombe</i>	...ASSK W KDRK....	SKDAN I MVV...	
<i>D. melanogaster</i>	...EEK W TLRK....	TKDS N VVLV...	
<i>A. thaliana</i>	...KATK W SERK....	T-DVN L LAVA...	
<i>X. leavis</i>	...EAK W QERK....	GKDT N MLVV...	
<i>H. sapiens</i>	...EAK W QERK....	GKDT N VMLV...	

Figure 2.11: Conserved CLASP-specific residue identified from Stu1-TOG2. Figure and legend reproduced from Majumdar et. al. 2018.

A. A distinctive tubulin-binding interface for Stu1-TOG2. Cartoon representation of the Stu2-TOG2:tubulin complex (left; PDB 4U3J), with a region of interest boxed. Close-up view of the TOG:tubulin interface in the region of interest for Stu2 (middle) and Stu1 (right). In Stu1-TOG2 an Arg fills the space normally taken by a Tryptophan; this Arg likely contacts tubulin directly, conferring distinctive tubulin-binding properties.

B. Multiple-sequence alignment of CLASP-family (top) and polymerase-family (bottom) TOG domains. W339 (Stu1 numbering) is highly conserved in both CLASP and polymerase TOGs; R386 is highly conserved in CLASPs but in polymerases that position is an asparagine.

Table 2: Data collection and phasing		
	Anomalous	Native
Space group	P2 ₁	P2 ₁
Cell constants (Å or °)	a = 31.2 b = 110.8 c = 44.8 β = 101.6	a = 31.4 b = 111 c = 44.9 β = 101.3
Wavelength (Å)	1.25478	0.97926
Resolution range (Å)	50.00–1.80 (1.83–1.80)	50.00–1.89 (1.92–1.89)
Unique reflections	26,628 (1009)	23,899 (1116)
Multiplicity	6.2 (2.5)	4.5 (3.6)
Data completeness (%)	95.9 (71.6)	98.6 (95.3)
R _{merge} (%)	11.8 (139)	7.4 (56.8)
R _{pim} (%)	4.8 (89)	4.0 (33)
CC _{1/2} (last resolution shell)	0.143	0.812
I/σ(I)	13.8 (0.5)	16.7 (2.4)
FOM*	0.2902	n/a
Anomalous signal	8.4%	n/a

Values in parenthesis refer to the highest resolution shell.

* Figure of merit for phasing is before density modification.

Table 3: Refinement statistics	
Resolution range (Å)	40.95-1.89 (1.97-1.89)
No. of reflections $R_{\text{work}}/R_{\text{free}}$	23025/1152 (2211/116)
Data completeness (%)	95.06(76)
Atoms (non-H protein/solvent)	2197/161
R_{work} (%)	17.3 (21.4)
R_{free} (%)	21.2 (29.3)
R.m.s.d. bond lengths (Å)	0.007
R.m.s.d. bond angles (°)	0.810
Mean B -value (Å ²) (non-H protein/solvent)	25.7/31.1
Ramachandran plot (%) (favored/additional/disallowed)	98.5/1.5/0
Maximum likelihood coordinate error (Å)	0.20
Missing residues, protein	1-27, 47-63,243-251
MolProbity Clashscore	4.02 (98 percentile)
MolProbity overall score	1.19 (99 percentile)

Binding affinities of Stu1-TOG2 point mutants to tubulin and MT lattice

I investigated the effect of point mutations to the putative tubulin-binding interface of Stu1-TOG2 to validate the interface. Polymerase TOGs such as Stu2-TOG1 and Stu2-TOG2 contain conserved residues on the tubulin-binding interface that mediate their high-affinity interactions with curved $\alpha\beta$ -tubulin (Ayaz et al., 2012). Specifically, these residues are a tryptophan that interacts with α -tubulin and an arginine that interacts with β -tubulin. CLASP-family TOGs, for the most part, contain the same conserved residues with TOG1 being a notable exception (see Figure 2.16 and Discussion). But in the current structures of TOG2, the amino acid sidechains appear to be positioned differently along the canonical binding interface (Figures 2.9, 2.10, 2.11). In order to investigate the importance of the conserved tryptophan and arginine to the binding interactions of Stu1-TOG2, I measured the affinity of single mutants W339A and R525A as well as double mutant W339A,R525A to both unpolymerized tubulin (via SV-AUC) and the MT lattice (via TIRF) (Figures 2.12, 2.13). In addition, I also investigated mutating the CLASP-family specific residue R386 (Figure 2.12). All these mutations substantially diminished tubulin-binding activity of Stu1-TOG2 as clearly demonstrated by the lack of shift of the sedimenting boundary in the $c(s)$ distributions of Figure 2.12. Interestingly, MT lattice binding is also affected by the tryptophan and arginine mutations (the experiment with the CLASP-specific residue mutant has not been carried out yet). These results indicate that both Stu1-TOG2:tubulin and Stu1-TOG2:MT interactions are mediated by the canonical TOG:tubulin interface (i.e. interhelical loops). In the case of Stu2 TOGs, the tryptophan and arginine residues were critical to the interaction with $\alpha\beta$ -tubulin and gave rise to the conformational selectivity demonstrated by the polymerase TOGs. Despite these same residues being important to the

interactions of Stu1-TOG2, it is not as conformationally selective and could potentially use the same interface to bind to both curved and straight forms of $\alpha\beta$ -tubulin. R386 appears to be a part of this distinctive Stu1-TOG2:tubulin binding interface (see also Discussion).

Circular dichroism (CD) of the point mutant proteins confirmed that the point mutations do not have a significant effect on protein stability (Figure 2.14).

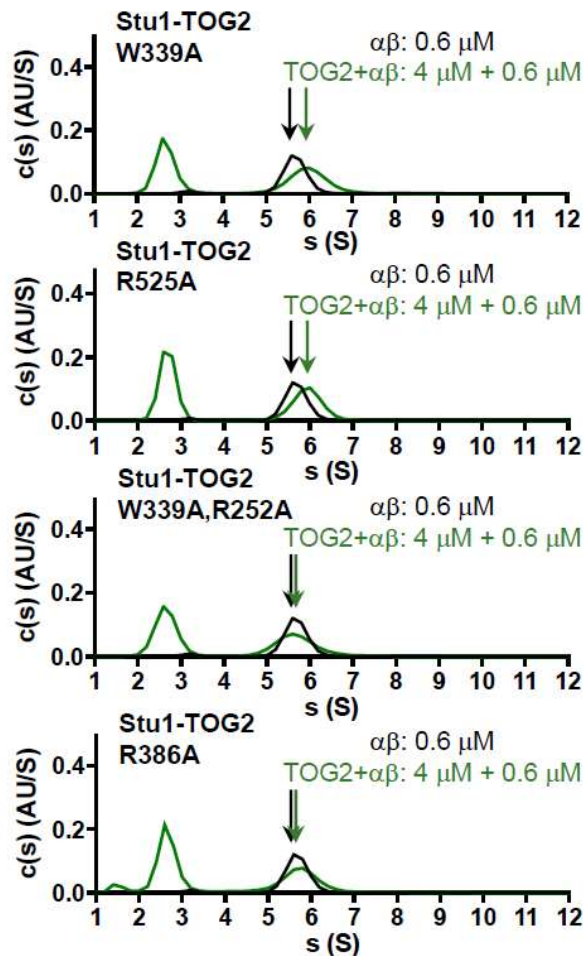
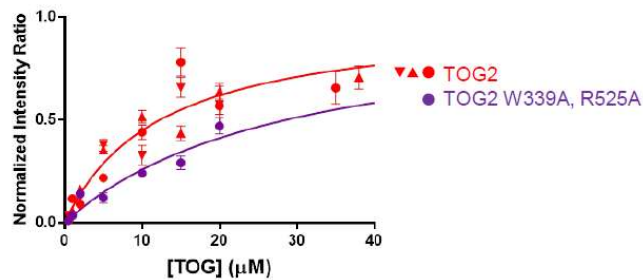


Figure 2.12: Mutating the tubulin-binding interface of Stu1-TOG2 results in loss of tubulin-binding activity. Figure and legend reproduced from Majumdar et. al. 2018.

W339A (top) and R525A (middle) substantially weaken interactions with unpolymerized $\alpha\beta$ -tubulin as detected by sedimentation velocity analytical ultracentrifugation; the double mutant W339A,R252A (bottom) and the CLASP-specific mutant R386A essentially abolishes interactions with tubulin. $c(s)$ distributions are shown for tubulin only (black) and tubulin+mutant (green).



	K_D (μM)
TOG2	12 ± 3
TOG2 W339A, R525A	29 ± 8

Figure 2.13: Affinity of Stu1-TOG2 W339,R525A to MT lattice. Figure and legend reproduced from Majumdar et. al. 2018.

A. Stu1-TOG2 W339A,R525A binds very weakly to MT lattice. Binding isotherm of Stu1-TOG2 W339A,R525A (purple) and TOG2 (red) to MT lattice showing normalized intensity on the lattice versus concentration and fit to a single-site binding model. TOG2 data reproduced from Figure 2. Concentrations of Stu1-TOG2 W339A,R525A were 0.5, 1, 2, 5, 10, 15, 20 μM . $n = 15$ scans per concentration for a single Stu1-TOG2 W339A,R525A titration (purple).

B. Binding affinities of TOG2 and TOG2 W339A, R525A

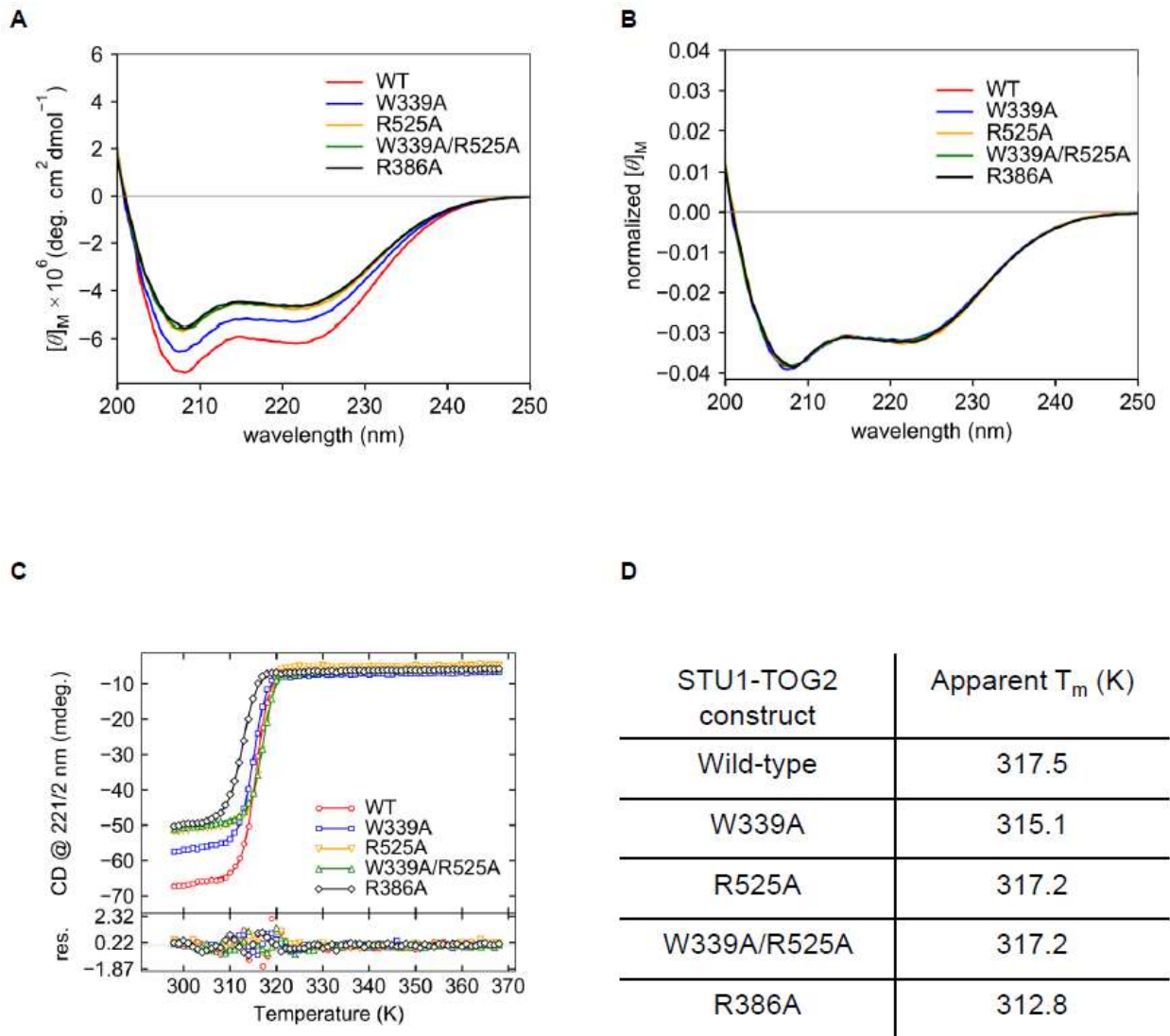


Figure 2.14: Folding and stability of Stu1-TOG2 mutants assessed by CD. Figure and legend reproduced from Majumdar et. al. 2018.

- A.** CD spectra of TOG2 and mutants showing characteristic secondary structural features in the far-UV. Amplitudes of the spectra vary due to differences in concentrations
- B.** Normalized spectra show nearly perfect overlap indicating that the point mutations do not cause large-scale structural changes
- C.** Melting curves (CD monitored at 221nm) in response to heating from 298.15 K to 368.15 K. Mutants show similar melting transition to wildtype TOG2, with the R386A mutant being slightly destabilized (see **D** for melting temperatures derived from these curves)
- D.** Apparent T_m for wildtype and mutant TOG2. Point mutations do not have significant effect on protein stability

The TOG1-TOG2 fragment of Stu1 adopts a compact arrangement

The docking of the linker I observed in the Stu1-TOG2 structure effectively shortens the connection between TOG1 and TOG2, and implies that in Stu1 the two domains should be nearer each other than if the linker were disordered, as it is thought to be in Stu2.

This prediction was tested by limited proteolysis (carried out by Sarah Munyoki) and small-angle X-ray scattering (SAXS) (data collection and analysis kindly carried out by Dr. Zhe Chen).

The TOG1-TOG2 fragments of Stu1 (CLASP-family) and Stu2 (polymerase-family) are of similar overall size (567 and 560 residues, respectively), and each contains two TOG domains that are linked by a comparably sized linker (62 and 75 residues, respectively). To probe the accessibility of sequences in the linkers relative to those in the folded TOG domains, Sarah used limited chymotrypsin proteolysis on the TOG1-TOG2 fragments of Stu1 (CLASP-family) and Stu2 (polymerase-family) (5 μ M TOG1-TOG2, Figure 2.12). We observed marked differences in the pattern of proteolysis on Stu1 compared to Stu2 (Figure 2.14). We only observed appreciable cleavage of Stu1-TOG1-TOG2 into two fragments at the highest levels of chymotrypsin (1:10 chymotrypsin:protein), and the weak intensity of the main proteolytic fragments suggested that the folded domains and the linker sequence were being proteolyzed at comparable rates. Thus, to a first approximation, residues in Stu1-TOG1-TOG2 are uniformly resistant to chymotrypsin treatment and show high protease resistance characteristic of folded domains. Stu2-TOG1-TOG2 behaved quite differently (Figure 2.12). Even at the lowest amount of chymotrypsin tested (1:10000 chymotrypsin:protein), a substantial amount of Stu2-TOG1-TOG2 was cleaved into two fragments, one slightly larger than the other. These

proteolytic fragments were much more resistant to proteolysis because they were only appreciably degraded at ~100-fold higher amounts of protease. Thus, these proteolysis experiments reveal differences in the behavior of the TOG1-TOG2 linker in Stu1 and in Stu2: in Stu1 the linker is approximately as protease resistant as the folded TOG domains, whereas in Stu2 it was much more protease sensitive, consistent with a greater degree of flexibility/disorder (Figure 2.14).

Next, we used SAXS to more directly examine the TOG:TOG separation in the TOG1-TOG2 fragments from Stu1 and Stu2 (Figure 2.12). In these solution experiments the angular dependence of scattered intensity provides information about the shape of the scattering object. James recorded SAXS intensity profiles for the TOG1-TOG2 fragments of Stu1 and Stu2 (Figure 2.14). The low angle scattering provides information about the compactness of the mass distribution in the object, which can be described by a 'radius of gyration' (R_g) derived from the slope of a Guinier plot. Despite similar molecular weights (67 and 64 kDa for TOG1-TOG2 fragments from Stu1 and Stu2, respectively), the TOG1-TOG2 fragments of Stu1 and Stu2 yielded different R_g values: 34.7 vs 43.5 Å, indicating a substantial difference in overall compactness (Figure 2.14). We also analyzed the scattering profiles in terms of the pair-distribution function, which provides a complementary way to characterize the shape of the scattering object using both low- and high-angle scattering data. Consistent with the Guinier analysis, $P(r)$ analysis also indicated that the TOG1-TOG2 fragment of Stu1 is more compact than that of Stu2: the maximum interatomic distance in Stu1-TOG1-TOG2 was 136 Å whereas for Stu2 it was 175 Å (Figure 2.14). In favorable circumstances where there is one dominant solution conformation, shape reconstruction from SAXS data can

provide more detailed insight into the underlying structure. However, and probably as a result of conformational flexibility, the SAXS data for Stu1-TOG1-TOG2 or Stu2-TOG1-TOG2 were not able to be well described by a single, fixed arrangement of TOG1 and TOG2 domains (not shown). Thus, while the SAXS data support a closer arrangement of TOG domains in Stu1 compared to Stu2, the data do not allow us to provide a unique model for how the domains are arranged.

We also used SAXS to gain insight into the solution structure of the linker-TOG2 construct that we crystallized (Figure 2.14). The scattering profiles we obtained were consistent with the smaller size of this fragment ($R_g = 24.4 \text{ \AA}$, $D_{max} = 80 \text{ \AA}$) (Figure 2.12 C). The extrapolated intensity at zero scattering angle (I_0) indicates that the linker-TOG2 was monomeric in solution during the measurement. In this case, *ab initio* shape reconstructions based on the measured scattering data (see Methods) yielded a molecular envelope that closely matched our crystal structure (Figure 2.14 D). Two orientations of our structure fit comparably into this envelope. Figure 2.14 E shows representative examples of these two orientations. In each of the two orientations, the disordered segments fit into 'bumps' in the calculated SAXS envelope that were not well-filled by the ordered parts from the crystal structure. That the disordered segments fill the parts of the SAXS envelope not occupied by the structured portion of the domain supports the model fitting into the SAXS envelope and provides evidence that the linker docking we observed is not a crystallization artifact.

Together, the data in this section indicate that the TOGs in Stu1-TOG1-TOG2 adopt a compact arrangement, likely because a segment of the linking sequence docks onto the side of the TOG2 domain as observed in the crystal structure (Figure 2.8-A, B). This

compact arrangement contrasts with the more extended arrangement of Stu2-TOG1-TOG2, wherein the linker sequence is not thought to form an integral part of one of either TOG domain. The functional importance of these differences is not yet clear.

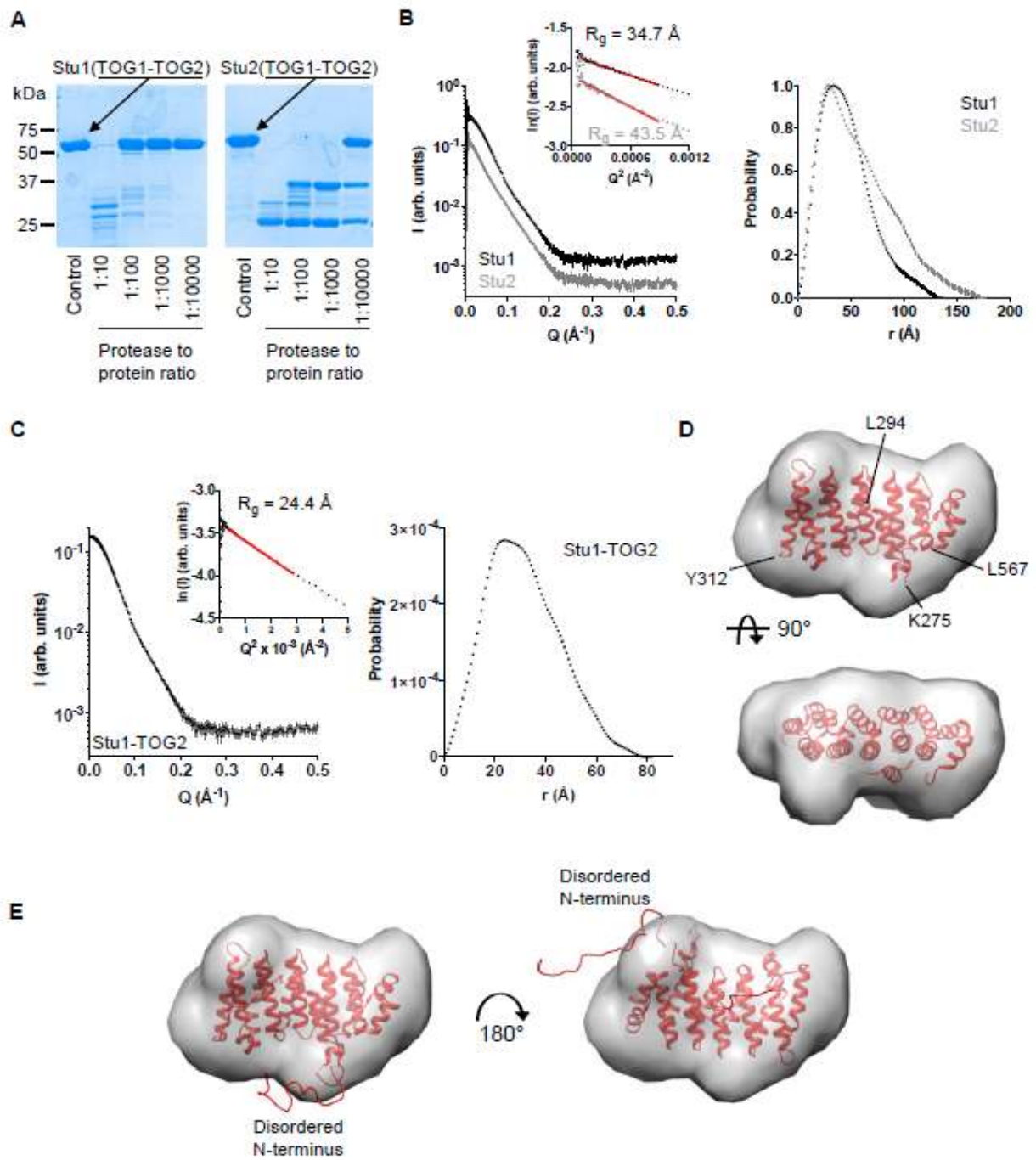


Figure 2.15: Solution analysis of TOG1-TOG2 and TOG2 fragments
 (*Legend on next page)

Figure 2.15: Solution analysis of TOG1-TOG2 and TOG2 fragments

A. Limited chymotrypsin proteolysis of TOG1-TOG2 fragments from Stu1 (left) and Stu2 (right). Stu1-TOG1-TOG2 is less protease sensitive than Stu2-TOG1-TOG2, consistent with a more compact structure (less flexible linker sequence).

B. (left) SAXS scattering intensity profiles for TOG1-TOG2 fragments from Stu1 (black) and Stu2 (grey). Curves are offset for clarity. Inset shows Guinier plots of the data and associated fit (red line). (right) Normalized pair distribution distributions ($P(r)$) for TOG1-TOG2 fragments of Stu1 (black) and Stu2 (grey).

C. (left) SAXS scattering intensity profile for the Stu1-TOG2 fragment. Inset shows Guinier plot of the intensity data and associated fit (red line). (right) Pair distribution distributions ($P(r)$) for TOG2.

D. Crystal structure of Stu1-TOG2 (cartoon) fit into a 3D volume reconstructed from the SAXS data for TOG2 (see **C.**). Two orthogonal views of the fit are shown.

E. Two alternative dockings of TOG2 into the 3D volume reconstructed from the SAXS data for TOG2, with models for disordered parts of the structure represented as a ribbon. (left) same docking as in **D** showing that in this orientation the disordered N-terminus fills an empty region at the bottom of the reconstructed volume; (right) alternative docking in which the TOG domain is rotated $\sim 180^\circ$ around an axis perpendicular to the page, in this orientation the disordered N-terminus fills an empty region at the top right of the reconstructed volume.

Discussion

In this Chapter, I have identified significant differences between the CLASP family Stu1-TOGs and the polymerase family Stu2-TOGs that could lead to a greater understanding of how these protein families use TOG domains to achieve divergent function.

The polymerase TOGs demonstrate high-affinity, conformationally-selective interactions tubulin. Specifically, both Stu2-TOGs bind curved $\alpha\beta$ -tubulin with an affinity in the 50-150 nM range mediated by the tryptophan and arginine on Stu2-TOG's interhelical loops. Mutating either residue abolishes this binding interaction. Additionally, neither Stu2-TOG has been observed to interact with the MT lattice in the absence of the lattice-binding basic domain. In fact, isolated Stu2-TOGs will depolymerize stabilized MTs!

In contrast, on the CLASP side, only Stu1-TOG2 appears to have appreciable binding affinity without a strong preference for the unpolymerized curved form of tubulin over the polymerized straight conformation, with the affinity for unpolymerized tubulin is 10-fold lower than that of polymerase TOGs. This finding raises several questions. Is the TOG:tubulin interface in TOG2 disrupted in some way? Is it possible that Stu1-TOG2 binds an intermediate form of tubulin between curved and straight? In order to look at the interaction between Stu1-TOG2 and tubulin, I attempted to crystallize a co-complex similar to the methods used to crystallize Stu2-TOGs in complex with a polymerization-incompetent tubulin (Ayaz et al., 2012, 2014). These efforts have so far proved unsuccessful and no hits have been obtained. Another approach using cryo-electron microscopy is described in Chapter 4 under current work in progress.

In the meanwhile, I was able to crystallize Stu1-TOG2 by itself. Analysis of this structure indicated differences with the polymerase TOGs such as a conserved CLASP-specific residue lending credence to the idea that the CLASP TOGs engage with tubulin in a somewhat different manner than the polymerase TOGs. Exactly how different is the interaction and the potential mechanistic insight that could be obtained from such information remains to be uncovered.

Next, Stu1-TOG1 is not only lacking in binding activity for either $\alpha\beta$ -tubulin or the MT lattice but also lacks the conserved binding residues that appear critical to the TOG:tubulin interfaces that have been analyzed so far in both CLASP and polymerase TOGs (Figure 2.16). What is the role of TOG1 then? In order to begin understanding TOG1's role, I also carried out binding assays with Stu1-TOG1-TOG2. Like TOG2, TOG1-TOG2 appears to have appreciable binding affinity to both unpolymerized and polymerized tubulin but the binding affinities seem about two-fold higher than those for TOG2 (affinity for $\alpha\beta$ -tubulin and MT lattice in TOG2 is 1.68 μM and 12 μM respectively while for TOG1-TOG2, they are 720 nM and 7 μM , summarized in Table 1). The presence of TOG1, the linker or both might be the source of this enhanced affinity. What the increased affinity means in the context of the full-length Stu1 protein will be a matter of investigation for the graduate student after me.

Finally, all these data seem to indicate that TOG2 might be important in Stu1's function. In order to test that hypothesis, I started out by studying the effect of the Stu1 TOGs on MT dynamics. The results are presented in the next chapter, Chapter 3.

Conservation:

STU1_TOG1	3VPIEEKMALLI	MDDENSQDLID
STU1_TOG2	EQNWKLRQSNI	DSQTTVREAMR
STU2_TOG1	YKLWKARLEAYF	HGDRNVRSQTM
STU2_TOG2	SSKWKDRVEALE	DTQPAIRTIGF
XMAP_TOG1	HKVWKARLNGYE	SREKAIRDEAK
XMAP_TOG2	AKKWQDRKEALE	DSAPEVRDAAF
XMAP_TOG3	SSNWKERLASME	ATNPAIRTSAI
XMAP_TOG4	DKNWKIRKEGLI	DRNGDVRKKSQ
XMAP_TOG5	HADFQHHIKGLA	DRDTTVRNAAL
CLASP1_TOG2	KHDWEQQRVNALF	DADSEARIEAR

Figure 2.16: Sequence alignment of Stu1-TOG1 and Stu1-TOG2 compared to Stu2, XMAP and CLASP TOGs illustrating lack of conserved residues in Stu1-TOG1

Stu1-TOG1 does not contain the canonical tryptophan and arginine that have been shown to engage tubulin in other TOGs. Other CLASP TOG1s appear to contain at least the arginine though most do not contain the tryptophan.

Stu1-TOG2, other CLASP TOG2s, and the polymerase TOGs contains both residues.

Experimental Procedures

Protein expression and purification

Yeast $\alpha\beta$ -tubulin was overexpressed in *S. cerevisiae* and purified as previously described (Geyer et al., 2015; Johnson et al., 2011a). Tubulin aliquots were stored in 10 mM PIPES pH 6.9, 1 mM $MgCl_2$, 1 mM EGTA containing 20 or 50 μ M GTP depending on the application. STU1-TOG1 (11-276) and Stu1-TOG2 (305-567) were subcloned into a modified pET28a vector containing N-terminal polyhistidine and SUMO tags (gift from Xuewu Zhang, UT Southwestern), overexpressed in *E. coli* strain BL21(DE3), and purified using Ni-affinity chromatography. The SUMO tag was cleaved by Ulp protease and removed by either cation exchange chromatography (Stu1-TOG2) or a second Ni-affinity chromatography (Stu1-TOG1). Point mutants in Stu1-TOG2 were prepared using site-directed mutagenesis (Quikchange, Stratagene) and expressed and purified like the wild-type protein. The integrity of all expression constructs was confirmed by DNA sequencing. All proteins were concentrated and dialyzed into RB100 (25 mM Tris pH 7.5, 100 mM NaCl, 1 mM $MgCl_2$, 1 mM EGTA) for storage. For AUC samples, an additional 20 μ M GTP was included in the dialysis buffer.

Crystallization and tantalum bromide soak/phasing

Crystals of STU1-TOG2 were initially obtained using sparse-matrix crystallization screening, performed using a Phenix DT Drop Setter, mixing protein (at ~10 mg/ml) and precipitant 1:1 for sitting-drop vapor diffusion at 20 °C. After optimization, the best crystals were obtained with manual setups using 18% PEG3350, 0.1 M HEPES pH 7.5 as the precipitant. Crystals were cryoprotected by quick serial transfer through 18% PEG3350, 0.1 M HEPES pH 7.5 containing 10% glycerol, then 20% glycerol and flash

frozen in liquid nitrogen. To obtain a heavy-atom derivative for experimental phasing, crystals were soaked with tantalum bromide (Jena Bioscience) (~0.2-0.5 mg) added directly to the 2 μ l sitting drop for 1 hour prior to flash-freezing.

Diffraction data were collected by remote control data collection using Argonne National Laboratory APS beamline 19ID, using wavelengths of 0.97926 and 1.25478 Å for native and derivative datasets respectively. Diffraction data were processed using HKL3000 (Minor *et al.*, 2006). Crystals adopt space group $P2_1$ with one molecule in the asymmetric unit and 42% solvent content. Native and tantalum-bromide soaked crystals diffracted isotropically to 1.89 and 1.80 Å resolution, respectively. The tantalum bromide dataset showed a strong anomalous signal of 8.4 %. SAD phasing, solvent flattening, and model building were performed using the automated routines in HKL3000 (Minor *et al.*, 2006). Manual rebuilding and refinement against the slightly better diffracting native dataset was performed using COOT (Emsley *et al.*, 2010) and PHENIX (Adams, 2010), respectively.

Analytical Ultracentrifugation

Samples for analytical ultracentrifugation (Stu1-TOG1, Stu1-TOG2 and mutants thereof, yeast $\alpha\beta$ -tubulin) were dialyzed into RB100 (25 mM Tris pH 7.5, 1 mM $MgCl_2$, 1 mM EGTA, 100 mM NaCl) containing 20 μ M GTP. Samples were mixed and incubated at 4 °C for at least one hour prior to the experiment. Analytical ultracentrifugation experiments was performed in an Optima XL-1 centrifuge using an An50-Ti rotor (Beckman Coulter) as previously described (Ayaz *et al.*, 2012; 2014; Geyer *et al.*, 2015), at 20°C after the centrifugation rotor and cells had equilibrated at that temperature for at least 2.5 hr. Sedimentation was monitored by absorbance at 280 nm.

Buffer viscosities, buffer densities, and protein partial-specific volumes were calculated using SEDNTERP (Laue et al., 1992). SEDFIT (Schuck, 2000) was used to generate $c(s)$ distributions. For binding titrations, $c(s)$ distributions from SEDFIT were imported into GUSSE (Brautigam, 2015) and integrated to generate an isotherm file for SEDPHAT (Schuck, 2010). SEDPHAT was used to fit the binding isotherms for TOG2 and TOG1-TOG2 to a single-site binding model (A+B Hetero-association) with a fixed s_{AB} (maximum sedimentation coefficient allowed) corresponding to a theoretical maximum for a 1:1 tubulin:TOG2/TOG1-TOG2 complex with an assumed frictional ratio of 1.3.

Microtubule co-sedimentation assays

Microtubule co-sedimentation assays were carried out as previously described (Ayaz et al., 2012; Geyer et al., 2015) using 3 μ M wild-type yeast $\alpha\beta$ -tubulin in 1x G-PEM assembly buffer (100 mM PIPES pH 6.9, 20% glycerol, 2 mM $MgSO_4$, 1 mM EGTA). Tubulin samples containing 5 mM GTP were polymerized for 30 min at 30 °C before adding candidate binding partner to a final concentration of 9 μ M. Mixed samples were incubated for an additional 30 min at 30 °C before pelleted by ultracentrifugation at 60,000 rpm ($\sim 150000 \times g$) at 30 °C for 30 min in a pre-warmed TLA-100 rotor (Beckman-Coulter). Afterward, supernatant was carefully removed, and pellet was re-suspended in an equal volume of assembly buffer, and samples were analyzed by SDS-PAGE.

SAXS : Data Collection, Analysis, Modeling

Purified protein samples were exchanged into RB100 containing 5% Glycerol using a Superdex 200 10/300 column. The samples for SAXS were at a concentration between 1 and 4 mg/mL. Measurements were taken at room temperature using the SAXS instrument at the 12ID-B beamline of the Advanced Photon Source, Argonne National

Laboratory. The energy of x-rays was 14 KeV. Data were collected using a Pilatus 2 M detector (DECTRIS) at a sample-to-detector distance of about 2 m, covering $\sim 0.004 - 0.85 \text{ \AA}^{-1}$ for the scattering vector Q . Immediately prior to data collection, samples were centrifuged at 15,000 g for 5 min, and the top 80 % of the solution was used for the SAXS measurement. This process helps eliminate any aggregates. Samples were measured in a quartz capillary flow cell with a 1.5 mm diameter under a flow rate of 10 mL/s to mitigate potential radiation damage. 30-40 successive frames with an exposure of 1 second were recorded for each sample, and the resulting data averaged to improve signal and reduce noise. Three concentrations of each sample were measured ('neat', 2-fold, and 4-fold diluted). Each sample measurement was preceded by the measurement of its matching buffer solution. In addition to being used for background subtraction, the buffer measurements also served as a check on beam properties and the cleanliness of the sample cell between switching of samples.

Scattering profiles (intensity I vs. scattering vector Q) were reduced and SAXS data were merged using beamline software. After buffer background subtraction, to eliminate the possible structure factor, the SAXS data were extrapolated against concentration to obtain the final zero-concentration SAXS data set for further data analysis. Pair distance distribution functions, $P(r)$, were calculated with GNOM (Svergun, 1992).

Low-resolution molecular shape reconstructions of Stu1-TOG2 from the experimental scattering data were performed with DAMMIN (Svergun, 1999) or DAMMIF (Franke and Svergun, 2009) with similar results. The scattering profiles were used up to a Q of 0.49 \AA^{-1} for the reconstruction. Multiple calculations were performed, and the

resulting bead models were averaged by DAMAVER (Volkov and and Svergun, 2003) to generate a final model representing the most probable shape for the protein. Fitting of the crystal structure of Stu1-TOG2 into the SAXS envelope was carried out using Chimera (Pettersen et al., 2004).

Limited chymotrypsin proteolysis

TOG1-TOG2 fragments from Stu1 or Stu2 (5 μ M final concentration) were incubated with different amounts of chymotrypsin for 90 min at room temperature. Chymotrypsin was serially diluted (10-fold steps) from a stock concentration of 1 mg/mL. Reaction was quenched by adding SDS-PAGE loading buffer and boiling for 10 min. Samples were analyzed by SDS-PAGE.

Total Internal Reflection Fluorescence Microscopy (MT lattice binding)

Yeast tubulin with a C-terminal WDCCPGCCK tag (Griffin *et al.*, 2000) was expressed and purified as described above for wild-type yeast tubulin (also described in (Geyer *et al.*, 2015)). 3 μ M aliquots were thawed and labeled with ReAsH-EDT2 reagent (Toronto Research Chemicals) by incubating with five-fold molar excess reagent and 2 mM TCEP for 90 minutes at room temperature. Excess free dye was then removed using Zeba Spin desalting columns (Thermo), and GTP γ S-stabilized microtubules were prepared as above. Stu1-TOG constructs with a KCK tag were purified as described above and stored at -80 °C. Aliquots were thawed on each day and labeled with Alexa-488 (similar to ReAsH labeling protocol above). Preparation of flow chambers was carried out as described above for DIC except GTP γ S-stabilized microtubules were not sheared before being flowed in. After microtubule incubation, 20 μ L RB100 + 10 μ M epothilone (to keep microtubules stable) containing various concentrations of fluorescent Stu1-TOG was flowed in.

Interactions of fluorescent Stu1 TOG constructs with MTs were imaged by total internal reflection fluorescence microscopy using an Olympus IX81 microscope with a TIRF ApoN 100x/1.49 objective lens, a 491 nm and 561nm 50 mW solid-state laser and Photometrics Prime95B camera. Reactions were done at room temperature and the microscope was controlled as described above. Images were taken with 5 ms exposure for the 561 nm channel and with 20 ms exposure for the 491 nm channel. Bleed through between channels was negligible. The fluorescence intensity from MT and the background fluorescence were measured by using the PlotProfile function (4 pixel wide measurement lines oriented perpendicularly to the MTs) in ImageJ (Schneider *et al.*, 2012). These linescans were fitted to a custom function (a sum of a sloped line, representing the background fluorescence and a normal distribution with pre-determined sigma from PSF measurements, representing the fluorescence from the MT):

$$I_{tot} = I_{bkgd,0} + k_{bkgd}x + \frac{I_{MT}}{\sqrt{2\pi\sigma^2}} * e^{-\frac{(x-x_0)^2}{2\sigma^2}}$$

Where $I_{bkgd,0}$ is the background intensity at $x = 0$, and k_{bkgd} is the slope of background intensity as a function of x . I_{MT} is the fluorescence intensity from the MT, $\sigma = 0.2 \mu\text{m}$ is the spread of the PSF, and x_0 is the location of the MT. The background intensity at x_0 was used as the background intensity fluorescence for all following calculations. The fluorescence intensity of MT is proportional (φ gives the proportionality constant) to the laser power (LP), the fluorophore labeling efficiency (LE), and the fractional saturation of TOG binding to MTs (f):

$$I_{MT} = \varphi * LP * LE * f = \varphi * LP * LE * \frac{[TOG]}{[TOG] + K_D}$$

The fluorescence intensity of the background is proportional to the laser power, the fluorophore labeling efficiency, and the concentration of the protein:

$$I_{bgd} = \varphi' * LP * LE * [TOG]$$

The quotient of above two intensities does not depend on the laser power or the labeling efficiency (which vary from experiment to experiment). Multiplying the quotient by concentration of TOG, we obtain a value that is proportional to the fractional saturation:

$$I_{norm} = \frac{I_{MT}}{I_{bgd}} * [TOG] = \frac{\varphi * LP * LE * \frac{[TOG]}{[TOG] + K_D}}{\varphi' * LP * LE * [TOG]} * [TOG] = \frac{\varphi}{\varphi'} * \frac{[TOG]}{[TOG] + K_D}$$

Finally, we normalize the green channel (TOG) intensity by the red channel (MT) intensity to account for the presence of some microtubule bundling (based on the distribution of microtubule fluorescence intensities, roughly 69% of the microtubules measured were singles, with about 29% as 2-wide bundles). All measured intensity ratios of all TOG constructs were fitted simultaneously with a binding isotherm with a global maximum intensity ratio:

$$I_{ratio} = \frac{I_{maxratio} * [TOG]}{[TOG] + K_D}$$

Microscale Thermophoresis

Protein stocks including labeled tubulin and unlabeled TOG constructs were purified and labeled as above. Buffer condition was identical to AUC: RB100 + 20 μ M GTP. A 15-point, 1:1 dilution series of TOG2 with 120 μ M as its highest concentration was prepared in 10 μ L aliquots. A sixteenth sample was prepared with no TOG2. To each

tube, 10 μ L of 80 nM tubulin that had been supplemented to 0.1% (v/v) Tween-20 was added and mixed, giving a highest [TOG2] of 60 μ M (for TOG1-TOG2, highest concentration is 32.5 μ M), a constant [tubulin] of 40 nM (50 nM for TOG1-TOG2 titrations), and a final concentration of Tween-20 of 0.05%. Samples were incubated in the dark for at least 30 min prior to loading them into premium-coated capillaries and placing them in the instrument (a NanoTemper NT.115 BLUE/RED device). The blue filter was selected, and three replicate titrations performed using 80% MST, 70% LED, a pre-IR phase of 5 s, an IR-on phase of 30 s, and a post-IR phase of 5 s (95% LED for TOG1-TOG2 titration). The data were analyzed using the 1:1 binding model in the program PALMIST (Scheuermann et al., 2016).

Circular Dichroism

Purified proteins (Stu1-TOG2, wild type and point mutants) were dialyzed into 10 mM Na Phosphate pH 7.5, 50 mM NaCl and diluted to approximately 0.4 mg/ml using the same buffer. Circular dichroism spectroscopy was performed on a Jasco J-815 CD spectrometer. 300 μ L samples were prepared and placed in 0.1 cm CD cuvette, degassed, and spectra collected from 190 to 250 nm. The CD as a function of temperature was monitored at 208 nm and 221 nm. Temperature was varied from 25 $^{\circ}$ C to 95 $^{\circ}$ C at a ramp rate of 1 $^{\circ}$ C/min. Melt data were fitted to the equation:

$$CD(T) = \frac{(b_1 + m_1T) + (b_2 + m_2T)e^{-\Delta H(1-T/T_m)/RT}}{1 + e^{-\Delta H(1-T/T_m)/RT}}$$

where b_1 and m_1 are respectively intercept and slope parameters for the left portion of the curve, b_2 and m_2 are respectively intercept and slope parameters for the right side of the curve, T_m is the melting temperature, and R is the universal gas constant.

Analysis of sequence conservation

Sequences for CLASP- and polymerase-family proteins from *S. cerevisiae* (Stu1 and Stu2), *S. Pombe* (Cls1 and Alp14), *D. melanogaster* (mast/Orbit and minispindles), *A. Thaliana* (CLASP and MOR1), *X. laevis* (XCLASP1A and XMAP215), and *H. sapiens* (CLASP1 and ch-TOG) were obtained from NCBI and aligned using T-coffee (Notredame et al., 2000). Portions of the multiple sequence alignment in the region of Stu1-TOG2(W339) and Stu1-TOG2(R386) are shown in Figure 2.11.

CHAPTER THREE: RECONSTITUTION

Reproduced from Majumdar et al 2018 with minor modifications (excluding Abstract section).

Abstract

In this Chapter, I describe the results of the reconstitution studies used to study the effects of Stu1 TOGs on MT dynamics. In *in vitro* reconstitution assays, the isolated Stu1 TOG2 domain potently suppressed MT catastrophe and stimulated MT rescue. Stu1 TOG1 did not have any such effects and assays containing Stu1 TOG1 were indistinguishable from the control. Mutating any of the three residues critical to Stu1 TOG2:tubulin interaction (W339, R525, R386 described in Chapter 2) abolished these effects. Observing these activities from an isolated TOG domain contradicts the expectation that an array of TOGs would be required to recapitulate the activity of the CLASP family in suppressing catastrophe and promoting rescue. However, Stu1-TOG2 also did not noticeably change the rates of growth or shrinking in dynamic MTs. This would seem to indicate that the observed changes in transition frequencies are not an indirect consequence of altered kinetics of MT growth or shrinking. Additionally, no change in the number of stabilizing cap sites (detected by Bim1-GFP binding) in the presence of Stu1-TOG2 were observed, furthering the idea that Stu1-TOG2 does not act by decreasing GTP-ase activity in the MT lattice. Taking these results together, we speculate that Stu1-TOG2 binds directly to the MT tip to influence transitions there.

Results

The isolated Stu1-TOG2 domain suppresses catastrophe and stimulates rescue

The ability of TOG2 to bind the microtubule lattice led us to speculate that TOG2 binding might affect microtubule stability and/or dynamics. We therefore used time-lapse differential interference contrast (DIC) microscopy to determine whether the presence of substoichiometric amounts of Stu1-TOG2 affected any of the parameters of microtubule dynamics: growing rate, shrinking rate, catastrophe frequency, or rescue frequency (Figure 3.1). We used 0.8 μ M yeast $\alpha\beta$ -tubulin and 200 nM Stu1-TOG2 for these experiments. Figure 3.1-A shows representative kymographs from the control experiment: dynamic microtubules growing from GTP γ S-stabilized seeds without any Stu1-TOG2 added. These kymographs are typical for wild-type yeast $\alpha\beta$ -tubulin, showing slow growth, frequent catastrophe, very fast shrinking, and no rescues. Figure 3.1-B shows representative kymographs from microtubules growing in the presence of 200 nM Stu1-TOG2. Stu1-TOG2 caused striking changes in microtubule dynamics: growth phases were substantially longer, and there were a number of rescue events. Microtubule growing and shrinking rates were largely unchanged by the addition of Stu1-TOG2 (~5% and ~7% difference, respectively, $p > 0.05$) (Figure 3.1-C). By contrast, there were substantial changes in the frequencies of catastrophe (inverse of microtubule lifetime) and rescue (Figure 3.1-C). Median microtubule lifetimes increased from 506 s in the control to 1580 s in the presence of Stu1-TOG2, corresponding to a four-fold decrease in catastrophe frequency (Figure 3.1-C). We also observed an appreciable rescue frequency in the presence of Stu1-TOG2 (~19 min^{-1} ; 37 rescues out of 82 catastrophes recorded); no rescues were observed in control measurements

where Stu1-TOG2 was not present (217 catastrophes observed) (Figure 3.1-C). Similar experiments using the Stu1-TOG1 domain (200 nM) behaved identically to control reactions without any TOG (Figure 3.3). It would appear TOG1 does not affect MT dynamics. Thus, the isolated Stu1-TOG2 domain is sufficient to stimulate rescue and suppress catastrophe, and these effects on microtubule transition frequencies occur without substantial changes in the rates of microtubule growing or shrinking.

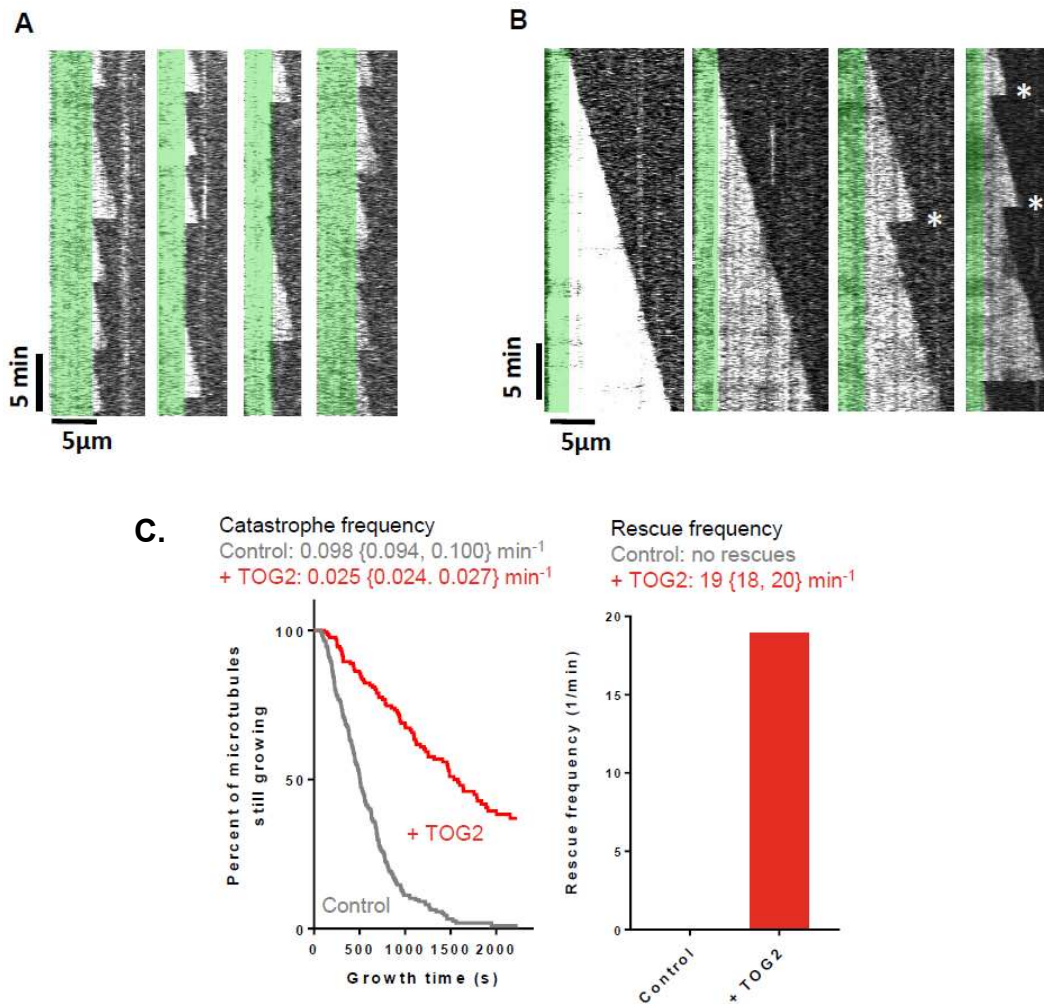


Figure 3.1: Anti-catastrophe and rescue activity of Stu1-TOG2. Figure and legend reproduced from Majumdar et. al. 2018.

A. Representative kymographs of yeast $\alpha\beta$ -tubulin ($0.8 \mu\text{M}$) growing from GTP γ S-stabilized seeds (pseudo-colored green). Microtubule dynamics were imaged using time-lapse DIC microscopy and show slow growth, rapid shrinking, frequent catastrophe and no rescues. See **C** for quantification of the dynamics.

B. As above, but in the presence of Stu1-TOG2 ($0.2 \mu\text{M}$). The presence of Stu1-TOG2 leads to longer growth phases (reduced catastrophe) and elevated rescue (rescues are marked with *).

C. Quantification of the microtubule dynamics from **A** (in grey) and **B** (in red). From left to right: catastrophe frequency decreases four-fold in the presence of TOG2 (control: $0.098 \{0.094, 0.100\} \text{min}^{-1}$, $n = 57$, 160 catastrophes; +TOG2: $0.025 \{0.024, 0.027\} \text{min}^{-1}$, $n = 44$, 38); rescue frequency increases in the presence of TOG2 (control: no rescues; +TOG2: $19 \{18, 20\} \text{min}^{-1}$, $n = 21$, 16 rescues). Values reported for transition frequencies are weighted average over two independent experiments. n gives the number in each of two trials. Averages from each separate experiment is given in braces to provide a measure of experimental variation.

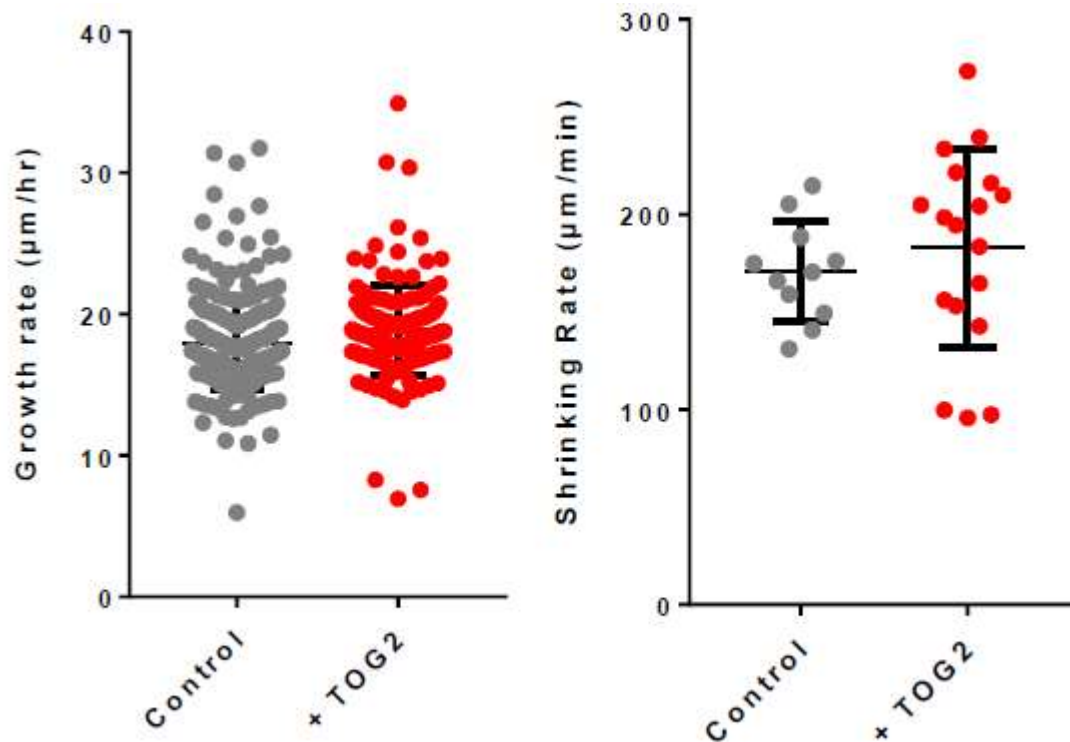


Figure 3.2: Stu1-TOG2 does not affect growth rates or shrinking rates. Figure and legend reproduced from Majumdar et. al. 2018.

Quantification of the microtubule dynamics similar to Figure 3.1. From left to right: growing rates do not change substantially (control: $17.9 \pm 0.2 \mu\text{m/hr}$, $n = 245$; +TOG2: $18.8 \pm 0.3 \mu\text{m/hr}$, $n = 126$); shrinking rates are also little changed (control: $170 \pm 8 \mu\text{m/min}$, $n = 11$; +TOG2: $183 \pm 12 \mu\text{m/min}$, $n = 18$); Error bars on the scatter plots indicate overall mean and standard deviation. Values reported for growth rates are weighted average over two independent experiments. n gives the total number of observed events for growing and shrinking rates. Values reported for shrinking rates are from a single experiment. Errors reported for growth and shrinking rates are SEM.

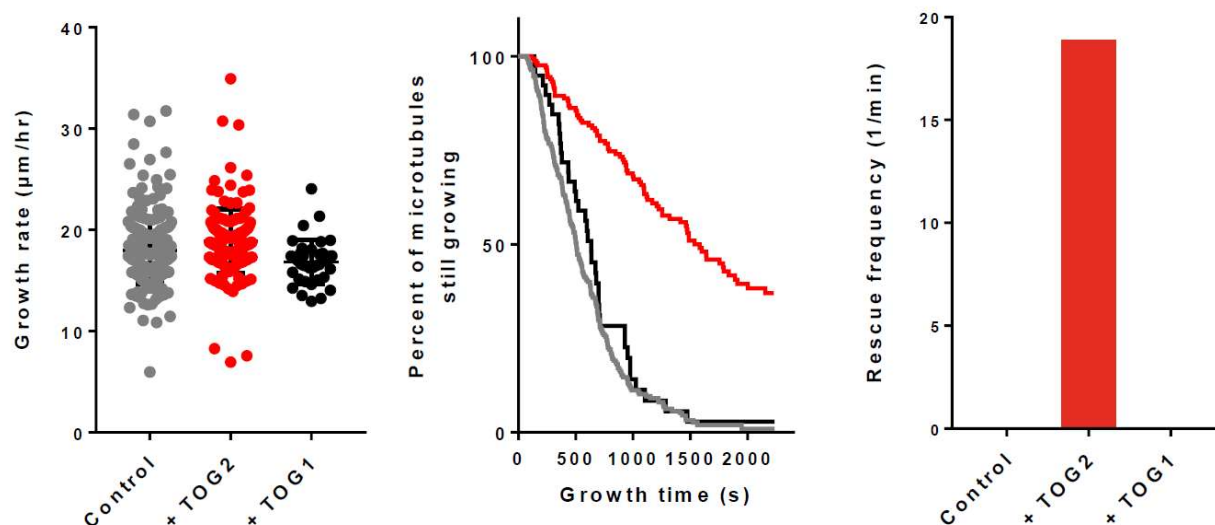


Figure 3.3: TOG1 does not affect MT dynamics. Figure and legend reproduced from Majumdar et. al. 2018.

Quantification of the microtubule dynamics in presence of 200 nM TOG1 (in black; data for Control, grey, and TOG2, red, are reproduced from Figure 5). From left to right: growing rates do not change substantially (control: $17.9 \pm 0.2 \mu\text{m/hr}$, $n = 245$; +TOG1: $16.8 \pm 0.3 \mu\text{m/hr}$, $n = 38$; for comparison +TOG2: $18.8 \pm 0.3 \mu\text{m/hr}$, $n = 126$); in contrast to the anti-catastrophe activity we observed for Stu1-TOG2, no change in catastrophe frequency is observed in the presence of TOG1 (control: $0.098 \{0.094, 0.100\} \text{min}^{-1}$, $n = 57, 160$; +TOG2: $0.025 \{0.024, 0.027\} \text{min}^{-1}$, $n = 44, 38$; +TOG1: 0.092min^{-1} , $n = 36$). No rescues were observed in the presence of TOG1 (control: no rescues; +TOG1: no rescues; for comparison +TOG2: $19 \{18, 20\} \text{min}^{-1}$, $n = 21, 16$ rescues). Values reported for control and +TOG2 are weighted average over two independent experiments with the averages from each separate experiment given in braces to provide a measure of experimental variation, followed by number of observed events in each trial. Values for +TOG1 are from a single trial.

Mutations on the tubulin-binding interface of Stu1-TOG2 abolish anti-catastrophe and rescue activity in vitro, Stu1 function in cells

Polymerase-family TOG domains contain conserved residues at the 'top' and 'bottom' of their tubulin-binding surface that mediate their conformation-selective, high-affinity interactions with curved $\alpha\beta$ -tubulin. CLASP-family TOGs contain the same conserved residues, but as mentioned previously they are positioned somewhat differently in the structure (Figures 3.1, 3.2). To determine if both of these conserved residues (W339 and R525 in Stu1-TOG2) are important for the catastrophe-suppressing and rescue-promoting activities of TOG2, we measured the effects of singly (W339A or R525A) or doubly (W339A,R525A) mutated TOG2 on microtubule polymerization dynamics (Figure 3.4-A; 200 nM TOG domain was used). The single or double mutant TOG2 domains failed to suppress catastrophe or to promote rescue: reactions containing W339A, R525A, or W339A,R525A all showed a high frequency of catastrophe, and a complete lack of rescues, similar to what we observed in 'no TOG2' control reactions (Figure 3.4-B). The mutant Stu1-TOG2 domains also are impaired for tubulin binding (Figure 3.4-B). Circular dichroism spectroscopy confirmed that the mutants were stably folded at 30 °C (see Chapter 2), so the lack of anti-catastrophe and rescue effects do not result from a mutation-induced defect in folding or stability.

We also investigated the consequences of mutating the CLASP-family-specific residue R386 (Figure 3.4-D). Stu1-TOG2(R386A) failed to suppress catastrophe, and did not enhance rescue (Figure 3.4 D). Stu1-TOG2(R386A) also substantially eliminated the tubulin-binding affinity of Stu1-TOG2 (Figure 3.4-D). Together, these data demonstrate that the CLASP-family-specific residue we identified in the structure is required for the anti-catastrophe, rescue-promoting, and tubulin-binding activities of Stu1-TOG2.

In summary, specific interactions between the isolated Stu1-TOG2 domain and $\alpha\beta$ -tubulin underlie the anti-catastrophe and rescue promoting activities we observed. The CLASP-family-specific residue we identified at the 'top' of the presumptive Stu1-TOG2:tubulin interface is essential for these activities. For the polymerase TOGs Stu2-TOG1 and Stu2-TOG2 to bind curved $\alpha\beta$ -tubulin, the 'top' and 'bottom' of the TOG (corresponding to W339 and R525 in Stu1-TOG2) must simultaneously contact $\alpha\beta$ -tubulin (Ayaz *et al.*, 2012; 2014). Single mutations in Stu1-TOG2 (W339A or R525A or R386A) abolish anti-catastrophe and rescue activity, so it seems plausible that Stu1-TOG2 exerts its effects on microtubule dynamics by recognizing a particular conformation of $\alpha\beta$ -tubulin (see Discussion).

Are the catastrophe suppressing and rescue promoting activities of the isolated Stu1-TOG2 domain relevant to the essential function to Stu1 in cells? We addressed this question using a genetic rescue assay (Figure 3.4-C). We prepared cells in which endogenous Stu1 protein could be conditionally depleted (Nishimura *et al.*, 2009): we incorporated a *stu1*-AID allele at the endogenous *STU1* locus, and a transgene to express the TIR1 F-box protein at the *HIS3* locus; addition of the plant hormone auxin to these cells results in rapid degradation of Stu1-AID protein and concomitant loss of cell viability. Wild-type Stu1 (non-degradable because no -AID), expressed from a centromeric plasmid under control of its endogenous promoter, fully rescues the growth defect caused by depletion of endogenous Stu1-AID (Figure 3.4-C). In contrast, covering alleles with W339A or R525A mutations in the full-length *STU1* gene failed to compensate for the loss of endogenous Stu1-AID. A covering allele with the R386A mutation (the CLASP-family-specific residue we implicated in tubulin binding, Figure

2.11, 3.3-A) also could not compensate for the loss of endogenous Stu1-AID. Thus, mutations that abolish the tubulin-binding, anti-catastrophe, and rescue-promoting activities of isolated TOG2 in vitro also significantly impair the function of Stu1 in cells.

The results from point mutants in the rescue assay (Figure 3.3-C), and data from others (Funk *et al.*, 2014), both indicate that an intact TOG2 domain is necessary for Stu1 function. Other regions of the protein, for example the dimerization domain or the basic region that mediates binding to the microtubule lattice, have also been shown to make important contributions to the physiological functions of Stu1 (Funk *et al.*, 2014).

In contrast to Stu1-TOG2, the presence of Stu1-TOG1-TOG2 (200 nM) caused a decrease in the rate of microtubule elongation (Figure 3.5). Thus, it seems that when in the same polypeptide (Stu1-TOG1-TOG2), the presence of the TOG1 domain can influence the activities of TOG2. We do not yet understand the mechanistic origin of the different behaviors of Stu1-TOG1-TOG2.

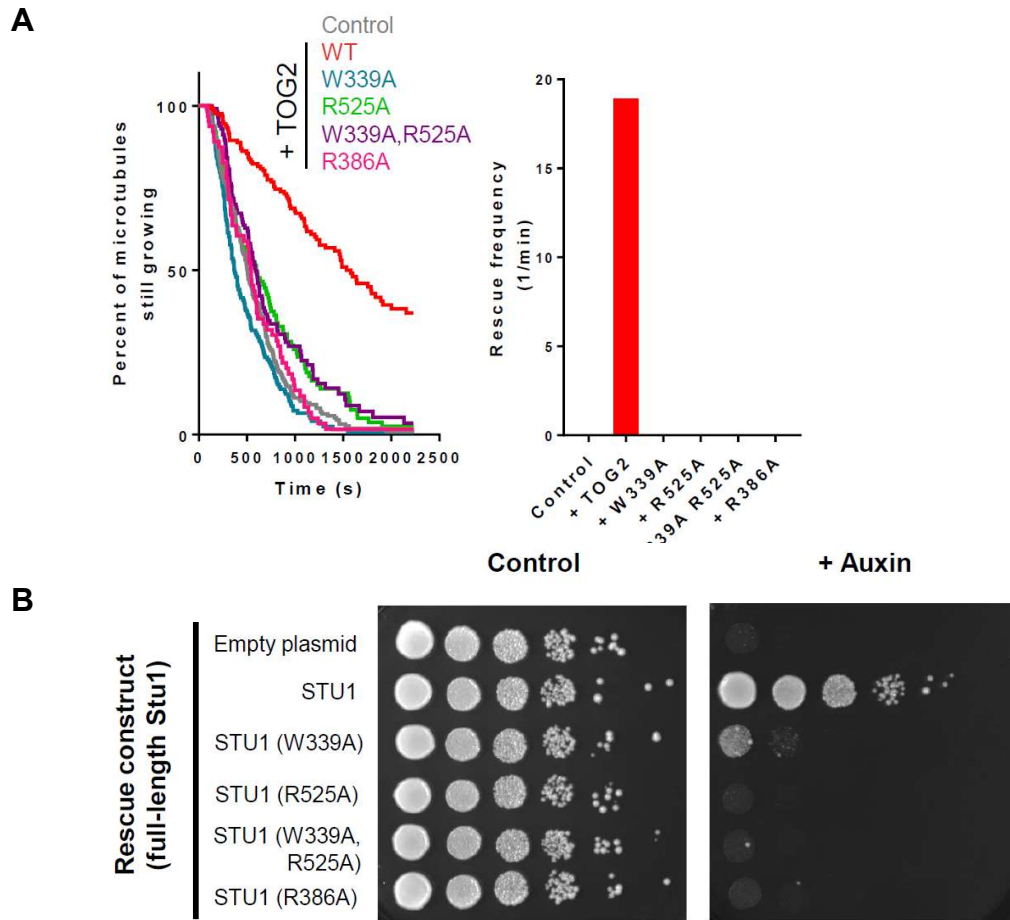


Figure 3.4: Consequences of mutating the tubulin-binding interface of Stu1-TOG2. Figure and legend reproduced from Majumdar et. al. 2018.

A. W339A (blue) or R525A (green) mutations on the tubulin-binding interface abolish anti-catastrophe (left) and rescue (right) activity comparably to the double mutant W339A,R525A (purple). R386A (pink), a mutation of the CLASP-specific residue identified from the structure, also abolishes anti-catastrophe and rescue-promoting activity. Assays were performed using yeast $\alpha\beta$ -tubulin ($0.8 \mu\text{M}$) with mutant TOG2 ($0.2 \mu\text{M}$). Catastrophe events for a single trial per mutant are summarized as a survival plot with average frequency (in min^{-1}) and number of measured catastrophes as follows: W339A, 0.118, 153; R525A, 0.0775, 94; W339A,R525A, 0.082, 98; R386A, 0.103, 60. Data with (red) and without (grey) TOG2 are duplicated from Fig. 5.

B. Results of a genetic rescue assay in which endogenous Stu1 can be degraded in an auxin-dependent manner, leading to a loss in cell viability. While plasmid-based expression of non-degradable wild-type, full-length Stu1 rescues the inducible growth defect, W339A, R529A, W339A,R529A (double mutant), and R386A point mutations in the full-length protein do not. STU1-AID cells expressing various covering alleles (as listed) were serially diluted and spotted on plates with either DMSO or auxin.

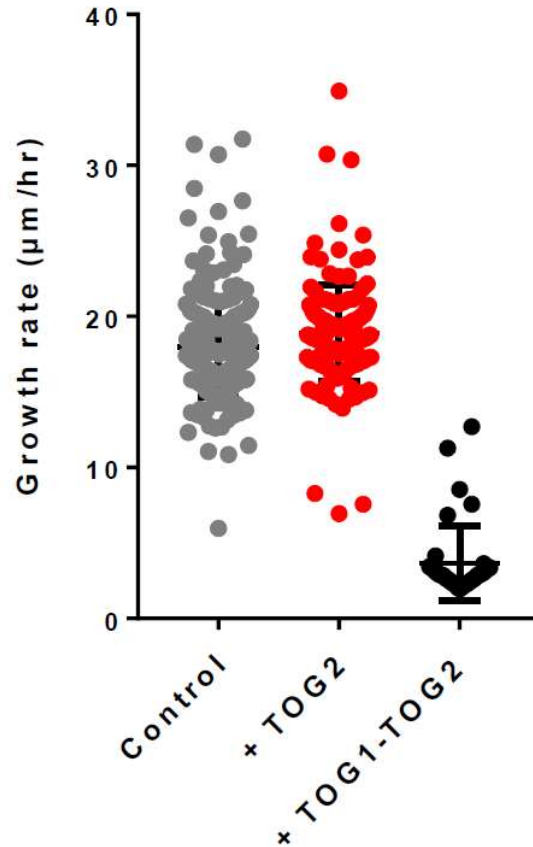


Figure 3.5: Effect of Stu1-TOG1-TOG2 on MT growth. Figure and legend reproduced from Majumdar et. al. 2018.

Growth rates of MTs in presence of TOG1-TOG2 (black) compared to Control (grey) and TOG2 (red) (data for Control and TOG2 reproduced from Figure 5). In presence of TOG1-TOG2, microtubules grow nearly 4-5 fold slower. From left to right: control: $17.9 \pm 0.2 \mu\text{m/hr}$, $n = 224$; +TOG2: $18.8 \pm 0.3 \mu\text{m/hr}$, $n = 126$; +TOG1-TOG2: $3.7 \pm 0.4 \mu\text{m/hr}$, $n = 33$). Transition frequencies for +TOG1-TOG2 were not quantified. Values reported are weighted average over two independent experiments; n denotes the number of observed events. Errors reported are SEM. Error bars on the scatter plots for growing rates indicate mean and standard deviation.

The TOG2 domain does not detectably increase the EB comet

We speculated that Stu1-TOG2 might influence dynamics by affecting the size of the microtubule's stabilizing cap. End-binding (EB) proteins mark the stabilizing cap region near the growing microtubule end (Bieling et al., 2007; Duellberg et al., 2016; Maurer et al., 2012; Zanic et al., 2009), so Tae Kim used the yeast EB protein Bim1 (Schwartz et al., 1997) to test whether Stu1-TOG2 influenced the size of the stabilizing cap or the number of EBs therein (Figure 3.5). He measured Bim1-GFP fluorescence intensity profiles along control microtubules (no Stu1-TOG2 present, Figure 3.5-A) and along microtubules with Stu1-TOG2 (200 nM) present in the assay (Figure 3.5-B). To obtain a higher signal to noise measure of the cap, he aligned and averaged multiple profiles together. Then, he fit a Gaussian distribution with different baselines for the lattice and for the background (see Methods) to quantify the total peak intensity and width of the Bim1-GFP 'comet' (Figure 3.5-C, D). The measured width of the caps (1σ ; 0.20 and 0.23 μm for samples without and with TOG2 respectively) (Figure 3.5-C, D) was comparable to the point spread function of our microscope (0.198 μm , also 1σ), which limits our ability to detect small changes in comet length. However, the integrated cap intensity (219 and 194 A.U. for samples without and with TOG2 respectively), which is related to the number of Bim1-GFP proteins bound in the cap region, did not differ significantly (Figure 3.5-C, D). Thus, while we cannot draw definitive conclusions about Stu1-TOG2-induced changes in the length of the cap, the intensity measurements indicate that the presence of Stu1-TOG2 does not increase the number of high-affinity EB binding sites in the cap. Consequently, the anti-catastrophe and rescue-promoting effects of Stu1-TOG2 probably do not result from an increase in the size of the microtubule's stabilizing cap.

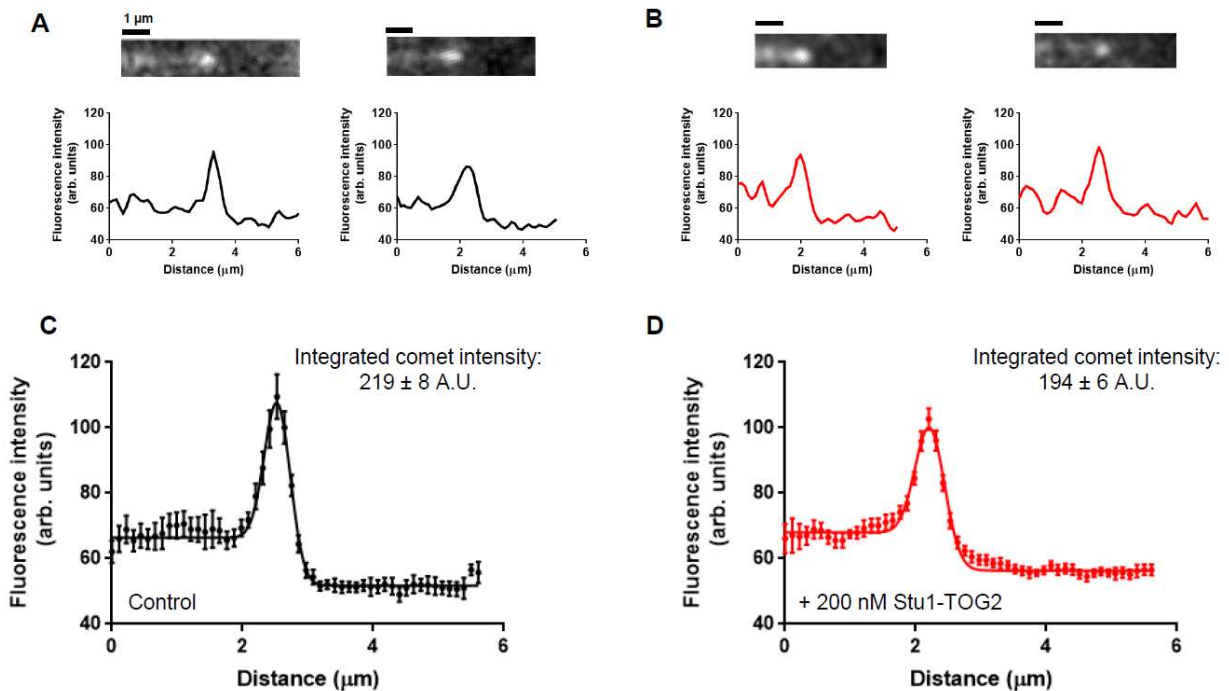


Figure 3.6: TOG2 does not influence the stabilizing cap. Figure and legend reproduced from Majumdar et. al. 2018.

A. Representative still images and associated fluorescence intensity line scans characterizing the comet of Bim1-GFP on the end of growing control microtubules with no Stu1-TOG2 added (microtubules are unlabeled in this experiment, and the direction of growth is left to right). Bim1 is the yeast EB protein.

B. As in A, but with 200 nM Stu1-TOG2 (unlabeled) added to the assay.

C. Aligned and averaged comet profile ($n = 18$ comets) for Bim1-GFP comets on control microtubules growing without any Stu1-TOG2 present. Solid line shows fit by a Gaussian with different baseline intensity behind the cap (on the microtubule lattice) and in front of the cap (actual fluorescence background). (The peak intensity integrates to 219 ± 8 A.U. and the fitted peak width, σ , is $0.20 \pm 0.01 \mu\text{m}$)

D. As in C, but for the reactions including 200 nM Stu1-TOG2 ($n = 30$ comets, the peak intensity integrates to 194 ± 6 A.U. and the fitted peak width, σ , $0.23 \pm 0.01 \mu\text{m}$). Neither peak intensity nor peak width are significantly different between the control and the +Stu1-TOG2 reactions by ANOVA (For peak intensity: $F(1, 37) = 1.667$, $p = 0.3223$; for peak width: $F(1, 37) = 1.082$, $p = 0.9218$)

Discussion

Multiple families of microtubule regulatory factors contain arrays of TOG domains. Recent studies of microtubule polymerases have demonstrated that polymerase activity requires at least two linked TOG domains, establishing a paradigm that regulatory function requires arrayed TOGs (Widlund *et al.*, 2011; Ayaz *et al.*, 2014). We began this study with the expectation that the anti-catastrophe and rescue-promoting activity of CLASP-family proteins would also require linked TOGs. However, our experiments revealed that the isolated Stu1-TOG2 domain displays anti-catastrophe and rescue-promoting activity, without need for a second, linked TOG partner. Our findings are corroborated by similar activity demonstrated in the structurally distinct vertebrate CLASP-family TOGs like hCLASP1-TOG2 (Aher *et al.*, 2018). Nevertheless, by demonstrating that an isolated TOG domain can display the same kinds of regulatory activities attributed to the full-length protein from whence the TOG came, the results reported here expand our understanding of what TOG domains can do and how they may do it. In particular, that an isolated CLASP-family TOG can suppress catastrophe and promote rescue indicates that ‘tethering’ of an unpolymerized tubulin to the lattice is not strictly required for these activities.

Not requiring a linked array of TOGs to obtain activities promoted by the intact protein may have implications for other TOG-containing regulatory factors. Indeed, recent structures of TOG3, TOG4, and TOG5 from XMAP215-family microtubule polymerases (Byrnes and Slep, 2017; Howard *et al.*, 2015), and of TOG domains from cilium-localized regulatory factors (Das *et al.*, 2015; Rezacikova *et al.*, 2016), have revealed a range of TOG structures, variable conformation-specificity for tubulin binding, and a

diversity of linker dockings or other appendages. Understanding how these 'alternative' TOGs contribute to different regulatory functions, and whether they need a tethered TOG partner to achieve activity, are interesting questions for future work.

Our data exclude several potential mechanisms for how the isolated Stu1-TOG2 domain suppresses catastrophe and promotes rescue. Less catastrophe and more rescue might in principle be achieved by increasing the rate of microtubule elongation. However, Stu1-TOG2 did not significantly change microtubule elongation rates, so Stu1-TOG2 probably does not exert its effects by changing the conformation of unpolymerized $\alpha\beta$ -tubulin or by changing the structure/configuration of the growing microtubule end. Less catastrophe and more rescue could in principle also be achieved by reducing the rate of microtubule shrinking, for example by stabilizing the GDP microtubule lattice. But we observed that the presence of Stu1-TOG2 did not alter microtubule shrinking rates, so it seems unlikely that Stu1-TOG2 exerts its effects by stabilizing the GDP microtubule lattice. Finally, less catastrophe could be achieved by increasing the size of the microtubule's stabilizing cap. Yet, we measured comparable amounts of Bim1-GFP, the yeast EB protein that marks the stabilizing cap, bound at the growing end in the presence and absence of Stu1-TOG2. Thus, the anti-catastrophe and rescue activity of the isolated Stu1-TOG2 domain cannot be explained by effects on unpolymerized $\alpha\beta$ -tubulin, on the configuration of the growing microtubule end, by stabilization of the GDP lattice, or by an increase in the size of the stabilizing cap. Some other as yet unidentified molecular mechanism must be operating.

Whatever the mechanism by which Stu1-TOG2 acts, the genetic rescue assays we performed indicate that the essential function of Stu1 is lost when Stu1-TOG2

interactions with tubulin are abrogated. A similar result was obtained for Cls1, the *S. pombe* ortholog (Al-Bassam et al., 2010). Given that the isolated Stu1-TOG2 domain is sufficient to suppress catastrophe and promote rescue *in vitro*, it could be that the other domains of Stu1 serve to recruit more TOG2 to the microtubule lattice (e.g. the basic region) or to amplify the activity of individual TOG2s (e.g. via dimerization). Other regions of CLASPs can dictate specific localization patterns (e.g. an EB-interacting SxIP motif (Honnappa et al., 2009; Patel et al., 2012) or kinetochore localization mediated by Stu1-TOG1 (Funk et al., 2014)). It is also possible that more intimate inter-domain cooperation operates to modulate the activity of Stu1-TOG2. Indeed, we find it interesting that both yeast and vertebrate CLASP TOGs feature 'docked' linkers that force a more compact arrangement of the linked TOGs. Presumably this conserved feature of CLASP TOGs reflects some important but as yet undetermined constraint on their function.

Suppression of catastrophe and promotion of rescue could in principle represent two distinct molecular activities of Stu1-TOG2. However, given that none of the Stu1-TOG2 mutants we tested separated anti-catastrophe activity from rescue-promoting activity, it seems simpler to consider the possibility that Stu1-TOG2 achieves both effects using a common molecular mechanism. Recent data on human CLASP2 TOGs, however, has indicated that the two activities could be different since hCLASP2 TOG2 suppresses catastrophe while hCLASP2 TOG3 appears to mildly promote rescue with no apparent effect on catastrophe (Aher et al., 2018).

But what is the mechanism? The selective effects on transition frequencies (catastrophe and rescue) without changes in growing or shrinking rates suggest that the isolated

Stu1-TOG2 domain acts directly on $\alpha\beta$ -tubulin subunits at (or very near) the microtubule end. Stu1-TOG2 affects catastrophe and rescue at low concentrations where its interactions with unpolymerized $\alpha\beta$ -tubulin or with the microtubule lattice are far from saturation. One speculative explanation for the different concentration-dependence Stu1-TOG2 binding and activity is that Stu1-TOG2 influences transition frequencies because it binds more tightly to some intermediate state of $\alpha\beta$ -tubulin at the microtubule end that is important for catastrophe and rescue but not rate-limiting for steady-state growing or shrinking. The same regions required for individual polymerase TOGs to bind curved tubulin are important for the tubulin-binding and anti-catastrophe and rescue-promoting activities of Stu1:TOG2, so this intermediate state might be a partially curved conformation of $\alpha\beta$ -tubulin at the microtubule end. This conformation-selective model is appealing because it resonates with the known conformation-selectivity of polymerase TOGs like Stu2-TOG1 and Stu2-TOG2. However, our data do not exclude other kinds of models, for example those in which Stu1-TOG2 does not bind more tightly to an intermediate conformation of $\alpha\beta$ -tubulin, in which the TOG domain itself undergoes conformational re-arrangements on the microtubule, or something else. Resolving this ambiguity will require knowledge about the optimal tubulin conformation for Stu1-TOG2 binding.

I discuss further experiments to gain more knowledge about Stu1-TOG2:tubulin binding conformation in Chapter 4.

Experimental Procedures

Time-lapse Differential Interference Contrast microscopy

Flow chambers were prepared as described previously (Gell et al., 2010; Geyer et al., 2015; Piedra et al., 2016) with the exception that GTP γ S-stabilized “seed” yeast microtubules were used instead of axonemes to template microtubule growth. To make seeds, 3 μ M wild-type yeast $\alpha\beta$ -tubulin in 1x G-PEM was allowed to polymerize overnight at 30 °C with 2mM GTP γ S. The resulting GTP γ S-stabilized microtubules were sheared by vigorous pipetting before being introduced into the flow chamber. Chambers were pre-incubated for 10 min with an anti-His-tag antibody (Millipore) diluted to 5 μ g/mL in BRB80, 80 mM PIPES pH 6.9, 1 mM MgCl₂, 1 mM EGTA (Millipore,). Chambers were then blocked with 1% F-127 Pluronic in BRB80 for 5 min, and washed with 1X PEM (100 mM PIPES pH 6.9, 1 mM EGTA, 1 mM MgSO₄) containing 1 mM GTP. Then, 3 μ L of sheared seeds were flowed in and incubated for 10 min. Yeast $\alpha\beta$ -tubulin aliquots were taken from -80°C, rapidly thawed, and passed through a 0.1 μ m centrifugal filter at 4 °C to remove aggregates. The concentration of $\alpha\beta$ -tubulin was measured by UV absorbance using an extinction coefficient of 115,000 M⁻¹cm⁻¹. Samples containing $\alpha\beta$ -tubulin and accessory protein (STU1 TOGs or mutants) in 1x PEM + 0.1 mg/mL BSA + 1 mM GTP + 10% RB100 were flowed into the prepared chamber containing seeds and the chamber immediately sealed with VALAP. Control experiments were carried out in the identical buffer and included 10% RB100 (without any accessory protein) to ensure matching buffer conditions.

MT dynamics were imaged by differential interference contrast microscopy (DIC) using an Olympus IX81 microscope with a PlanS Apo N 100x/1.49 NA objective lens and DIC

prisms. Illumination at 550 nm was obtained by inserting a bandpass filter of 550/100 nm (Olympus) in the light path. Temperature was maintained at 30 °C using a WeatherStation temperature controller with enclosure fit to the microscope's body. Micro-Manager 2.0 (Edelstein *et al.*, 2010) was used to control the microscope and a Photometrics Prime95B camera used to record the reactions. MT dynamics were recorded by taking an averaged set of 10 images of 100 ms exposure every 5 s for 37.5 min. Averaging was carried out using the FrameCombiner plugin in Micro-Manager 2.0. At the end of each movie, an averaged set of 200 out-of-focus background images was taken for background correction. The intensity of each image was normalized to its mean before the entire stack was divided by the background. To correct for temporal illumination variation during data acquisition, a second flat-field correction was performed using a flat-field image created by applying broad 20 pixel Gaussian filter to the original image. To improve contrast, a 2-pixel variance filter was applied. Kymographs were generated using ImageJ Reslice and MT length over time measured manually. Rates of MT elongation were calculated using MT length and timestamps of images. Lifetimes of each growing phase right before a catastrophe were also calculated and survival plots generated using GraphPad Prism. Catastrophe frequency was calculated as number of observed catastrophes divided by the sum total of lifetimes. Rescues were noted along with respective shrinking distances to calculate number of rescues per μm of shrinking, then converted to frequency using the shrinking rate (see below).

To measure shrinking rates, chambers were prepared as described above and incubated for 10 min to allow for growth before images were acquired continuously

(streaming), obtaining images every 20 milliseconds. We used Micromanager's "On-the-fly-data-processing" plugin to average 50 images together to form a single frame. Data processing was carried out as described above.

Comet analysis using Bim1-GFP

Preparation of flow chambers was carried out as described above. Samples of wild-type $\alpha\beta$ -tubulin along with 20 nM Bim1-GFP, with or without 0.2 μ M STU1 TOG2, in imaging buffer (1x PEM + 0.1 mg/mL BSA + antifade reagents (glucose, glucose oxidase, catalase) (Gell *et al.*, 2010)) were flowed into the chamber. Interactions of Bim1-GFP with MTs were imaged by total internal reflection fluorescence microscopy using an Olympus IX81 microscope with a TIRF ApoN 100x/1.49 objective lens, a 491 nm 50 mW solid-state laser and Photometrics Prime95B camera. Reactions were temperature controlled at 30 °C and the microscope was controlled as described above. Images of MTs were taken every 5 seconds for 15 min. Bim1-GFP fluorescence intensity along microtubules and extending beyond their growing ends was obtained using the PlotProfile function in ImageJ (Schneider *et al.*, 2012). These linescans were aligned using a custom-made function in MATLAB (see below). In this function, the linescans are initially aligned by aligning the maximum intensity points from the linescans. Then, the linescans were allowed to move one by one minimizing the average squared distance from the averaged linescan. This process was iterated until all linescans were stably aligned.

The function used for linescan alignment in MATLAB is inspired by (Maurer *et al.*, 2014), and includes terms for constant background fluorescence intensity, a Gaussian shaped Bim1-GFP comet, and a soft roll-off to capture the boundary between the Bim1-

GFP fluorescence and the background:

$$I_x = I_{Background} + I_{MTBody} * normcdf(x, x_0, \sigma_{PSF}) + \frac{I_{peak}}{\sqrt{2\pi\sigma^2}} * e^{-\frac{(x-x_0)^2}{2\sigma^2}}$$

Where I_x is the fluorescence intensity at position x , x_0 is position of the center of the comet, σ_{PSF} represents the PSF of our microscope, and σ is the comet width, $I_{background}$, I_{MTBody} , and I_{peak} are intensities of the background, body of the microtubule lattice, and peak respectively, and $normcdf$ is the cumulative normal distribution (used to model the fall-off in fluorescence intensity at the microtubule end).

Genetic rescue assay

We used an auxin-inducible degron system (Nishimura et al., 2009) to create a genetic rescue assay. *S. cerevisiae* strains used are described in Table S1. STU1-3HA-IAA7 was generated using PCR-based methods described in (Longtine et al., 1998; Miller et al., 2016) and integrated at the endogenous STU1 locus. pGPD1-TIR1 integration plasmid for integration at the His3 locus was a gift from Matthew Miller and Sue Biggins (Fred Hutchison Cancer Research Institute). Cells from the resulting strain express (i) Stu1 fused to an auxin responsive protein (IAA7) from endogenous STU1 locus, and (ii) TIR1, a protein required for auxin-induced degradation (Nishimura *et al.*, 2009).

Covering alleles were generated as follows. The STU1 gene with upstream and downstream regulatory sequences was amplified using PCR and subcloned into pRS315, a LEU2 centromeric plasmid (gift from Christine Weirich, UT Southwestern).

To avoid introducing undesired mutations in the rescue plasmid, point mutations in Stu1-TOG2 were introduced by QuikChange mutagenesis using a separate plasmid containing the coding sequence for residues 1-700 of STU1. After mutations were confirmed by sequencing, the MscI/PstI fragment was liberated for subcloning into the

similarly digested pRS315 rescue plasmid containing full-length STU1. The STU1-AID strain was grown overnight in YPD medium, made competent following Frozen EZ-Yeast transformation protocol (Zymogen), transformed with the covering alleles and plated on Leu(-) selective media.

For the spotting assay, the strains transformed with covering alleles were grown overnight in Leu(-) selective media and cells diluted to OD600 = ~1 from which serial 1:10 dilutions were made and spotted onto YPD plates with DMSO or 0.4 mM auxin (indole-3-acetic acid, Sigma, dissolved in DMSO). Plates were incubated at 30 °C for 2 days.

CHAPTER FOUR: PERSPECTIVES

To summarize, in the preceding chapters, I have presented data that show that a single isolated CLASP TOG domain is sufficient to suppress catastrophe and promote rescue. Unlike the polymerase TOGs that function in arrays to give polymerase activity, only a single CLASP TOG is enough to demonstrate anti-catastrophe and rescue-promoting activity akin to the full-length CLASPs.

How is a small TOG domain able to achieve this? In Chapter 3, I discussed several potential mechanisms, many of which are excluded by our current data. Stu1-TOG2 does not appear to be affecting MT dynamics by 1) increasing elongation rates (Figure 3.2), 2) affecting the strength of lateral contacts in the GDP lattice (no change in shrinking rates, Figure 3.2), or 3) changing the rate of GTP hydrolysis (no detectable change in Bim-1 cap size, Figure 3.6).

I speculated that the large effects on transition frequencies at the MT tip without affecting bulk growing and shrinking rates could mean that Stu1-TOG2 affects $\alpha\beta$ -tubulin at or near the MT end. One way to observe Stu1-TOG2 at the MT end is to conduct assays on dynamic MTs in the presence of fluorescently labeled Stu1-TOG2. Preliminary data from these assays have not shown an enrichment of Stu1-TOG2 at the end over the rest of the growing MT (data not shown), eliminating the possibility of a mechanism where a stably-bound Stu1-TOG2 tracks the growing end of a MT.

Interestingly, in experiments with fluorescent full-length CLASP2 (and EB1 to enhance localization and activity), accumulation of CLASP2 at the MT end did not correlate with sites of rescue (Lawrence et al., 2018). CLASP appears able to promote rescue without

significant accumulation at the tip and perhaps, the CLASP:tubulin interaction at the tip is more transient.

While further experiments are needed to confirm this observation, one possible mechanism for Stu1 activity is that Stu1-TOG2 stabilizes the “peeling” protofilaments at the end of a shrinking MT (an antithesis of the MCAK-influenced MT depolymerization model described in Chapter 1) or otherwise affects end-tapering in a growing MT but in a more transient manner. The peeling protofilament model could shed some light on the binding assay data highlighted in Chapter 2. Figure 4.1 shows a schematic of a peeling protofilament. The “curls” at the end of a MT protofilament are possibly an intermediate conformation between the curved conformation of unpolymerized $\alpha\beta$ -tubulin and the straight conformation of the polymerized form (Figure 4.1). So far, we know that Stu1-TOG2 displays an affinity for both curved and straight tubulin while still using the canonical TOG:tubulin interface established by studies of polymerase TOGs but the affinities are in the micro-molar range rather than nano-molar. It could be that Stu1-TOG2 binds a partially curved conformation of tubulin that is intermediate between the two forms, strengthening tubulin:tubulin interactions and supporting the formation of “curls”.

The formation of tubulin oligomers could explain the lack of saturation in TOG:tubulin binding assays using Stu1-TOG2 and Stu1-TOG1-TOG2 (Figure 2.5). The lack of saturation is likely due to a complex of higher molecular weight than a simple 1:1 interaction. Tubulin oligomers formed in the presence of Stu1-TOG2 could be shifting the reaction boundary to the right resulting in non-saturating binding isotherms. I have also carried out these binding titrations using polymerization-blocked tubulin mutants

(described in (Johnson et al., 2011b)) and found the lack of saturation in these assays as well (data not shown). This could indicate that the mutations in these “blocked” mutants are not sufficient to prevent the formation of these particular oligomers, especially if these oligomers are not stacked directly head-to-tail and are more curl-like (as illustrated in Figure 4.1).

This model explaining the binding mode of Stu1-TOG2:tubulin interactions that enhances tubulin:tubulin oligomerization could offer further insight into the mechanism of the anti-catastrophe and rescue effects of Stu1. But is this lack of saturation a universal CLASP behavior or is Stu1 an anomalous artefact? To determine that, I looked at sequence alignments of fungal CLASPs via NCBI’s BLAST to identify homologs that I could study to support or refute the observations made with Stu1-TOG2. I was able to identify two candidates that had good coverage but low sequence identity with Stu1. These CLASPs are from *Zygosaccharomyces rouxii* and *Kluyveromyces dobzhanskii*. Cloning, expressing, and purifying TOG1-TOG2 fragments of these fungal CLASPs allowed me to repeat the binding titrations and confirmed that the lack of saturation behavior is not limited to Stu1 (Figure 4.3). Addition of TOG1-TOG2 from either species to $\alpha\beta$ -tubulin results in a faster-sedimenting species indicative of a binding interaction. However, with increasing amounts of TOG1-TOG2 titrated against a constant amount of tubulin, the s-fast does not eventually stop increasing and the reaction boundary continues to shift to the right, even at ~100-fold excess of TOG1-TOG2 over $\alpha\beta$ -tubulin. This lack of saturation of the isotherm is consistent with Stu1:tubulin isotherms described above and in Chapter 2, lending credence to this being a universal behavior of CLASPs.

In order to explore the binding conformations of Stu1-TOG2:tubulin interactions, I am currently conducting cryoelectron microscopy on samples of tubulin and microtubules in the presence of Stu1-TOG2 as described below.

Current work on Stu1-TOG2:tubulin interactions

To look at the TOG2:tubulin interface in molecular detail, I initially attempted to co-crystallize a complex of Stu1 TOG2 with polymerization-incompetent $\alpha\beta$ -tubulin via methods successfully established by our lab using polymerase TOGs ((Ayaz et al., 2012, 2014). No hits were obtained and I speculate that the comparably weaker affinity of Stu1-TOG2 for tubulin compared to the polymerase TOGs may have hampered crystallization.

Continuing to look for structural details, I next looked at samples of $\alpha\beta$ -tubulin and Stu1-TOG2 using cryoelectron microscopy (Figure 4.3). $\alpha\beta$ -tubulin alone can be seen as single particles (Figure 4.3-A) whereas in the presence of Stu1-TOG2, I observed both single particles and oligomers (Figure 4.3-B). The oligomers are of particular interest to us since they seemingly adopt a “curl”-like conformation reminiscent of the depolymerizing end schematics shown in Figure 4.1. These samples were kept at 4 °C prior to grid preparation i.e. no 30 °C incubation was carried out that would have allowed the yeast tubulin to polymerize. I plan to study this conformation further and collect more data on these structures to obtain molecular detail.

The formation of tubulin oligomers in the presence of Stu1-TOG2 observed by cryoelectron microscopy is consistent with the oligomerization hypothesis that explains the lack of saturation of binding isotherms explained previously (Chapter 2, Figures 2.5 and 4.2). Oligomeric “curls” similar to those in Figure 4.3 were also observed in samples of polymerization-blocked mutant and Stu1-TOG2 analyzed by cryoelectron microscopy and could indicate that Stu1 is indeed stabilizing an intermediate tubulin conformation between curved and straight forms (data not shown).

Future Directions

In addition to analyzing the molecular details of the TOG:tubulin interface, there are several further areas of investigation pertaining to the other domains of Stu1. A study of the individual parts will allow us further insight into the mechanism behind the functioning of the whole protein.

Firstly, what is the role of Stu1-TOG1? While Stu1-TOG2 offers an intriguing insight into the mechanism of rescue and CLASP activity, we are still in the dark about the other domains. Stu1-TOG1 does not appear to have tubulin-binding activity or any effect on MT dynamics on its own, which then raises the question of its potential role in the full-length protein. *In vivo* studies have shown that Stu1-TOG1 is responsible for recruiting Stu1 to kinetochores as well as maintaining/regulating the stability of kinetochore MTs (Funk et al., 2014). My preliminary data indicates additional roles e.g. perhaps, TOG1 serves to enhance the binding affinity of TOG2 as seen in the increased affinity of TOG1-TOG2 (Chapter 2). Further analysis of Stu1-TOG1-TOG2 could help unearth any potential effect of Stu1-TOG1 on MT dynamics.

Secondly, what is the role of the shortened linker and the docked helix, which appears to be a feature of CLASP TOGs? This will be explored further in TOG1-TOG2 and TOG1-TOG2 mutants that vary the linker in length and/or sequence. Current work by Michal Niziolek in our lab is further quantifying the extent of the effects of TOG1-TOG2 on MT dynamics. Once that is established, we can proceed to compare the effects of altered linker lengths, allowing us to determine the scope of the role of the linker e.g. what is the minimum length of linker required, what happens if the linker is extended so as to render the two TOGs essentially independent, is the linker sequence important?

Next, how will the presence of the lattice-binding domain affect Stu1-TOG2 activity? In the case of the polymerase TOGs, we have observed that the lattice-binding domain is crucial to the “tethering” model described in Chapter 1 (Figure 1.12), with the tethering action allowing weakly-bound subunits to be captured by their neighbors and incorporated into the MT lattice. Could the Stu1 MT lattice binding region (ML domain) be playing a similar role albeit in supporting an anti-catastrophe mechanism? As a first step, we are attempting to study the effects on MT dynamics of Stu1-TOG domains in conjunction with the ML domain. Aside from the TOGs, Stu1’s ML domain has been mapped out by Funk 2013. Currently, members of our lab are trying to clone, express, and study TOG1-TOG2 and TOG2 constructs that are extended to include this ML domain. If the presence of the ML domain enhances the anti-catastrophe and rescue effects, that could support a model where the ML domain enhances Stu1 activity by allowing the TOGs to associate more effectively with the MT lattice.

Lastly, beyond the TOGs, the ML region and the dimerization domain, much of the full-length Stu1 is uncharacterized. The TOG2 domain only take up 500 amino acids out of the 1500 amino acids of the full-length protein and it will be interesting to study what the other 2/3rds of the protein is up to. Certainly, some of these regions are those that interact with the different CLASP binding partners. For example, in mammalian *in vitro* studies, EB1 enhances CLASP2 activity by localizing CLASP2 to the tip of the MT (Lawrence et al., 2018). It would be interesting to reproduce this study in yeast and observe 1) to what extent does Bim1 enhance Stu1 activity and 2) perhaps the resulting localization of Stu1 to the MT tip can offer further insight into the mechanism of the protein.

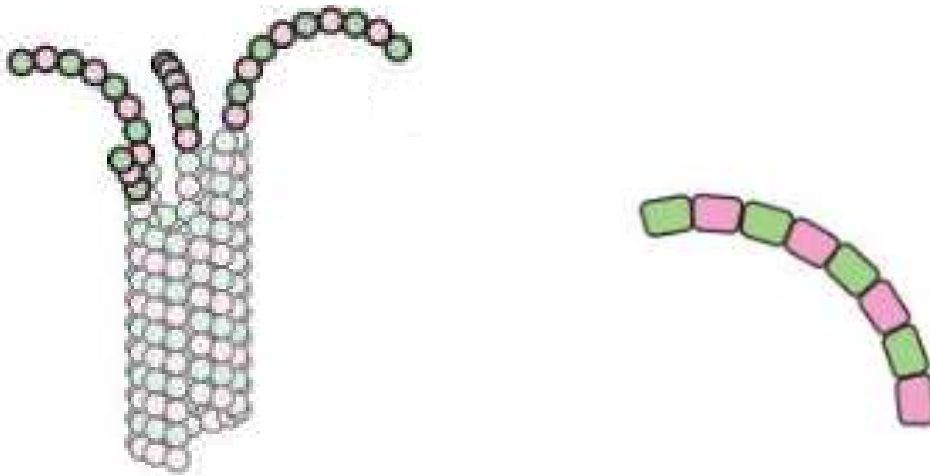


Figure 4.1: Schematic showing the end of a microtubule (left) and a single protofilament (right). Figures reproduced from (Brouhard and Rice, 2018).

As a MT depolymerizes, the protofilaments peel away from each other into “rams-horns” and the tubulin dimers start to relax back into a curved conformation. A single protofilament end could like the schematic shown on the right with $\alpha\beta$ -tubulin dimers still stacked end-to-end but not strictly in the straight conformation. If Stu1-TOG2 is able to stabilize this intermediate somehow, it could allow the microtubule to recover from catastrophe (rescue) or never fully transition into catastrophe (anti-catastrophe effect).

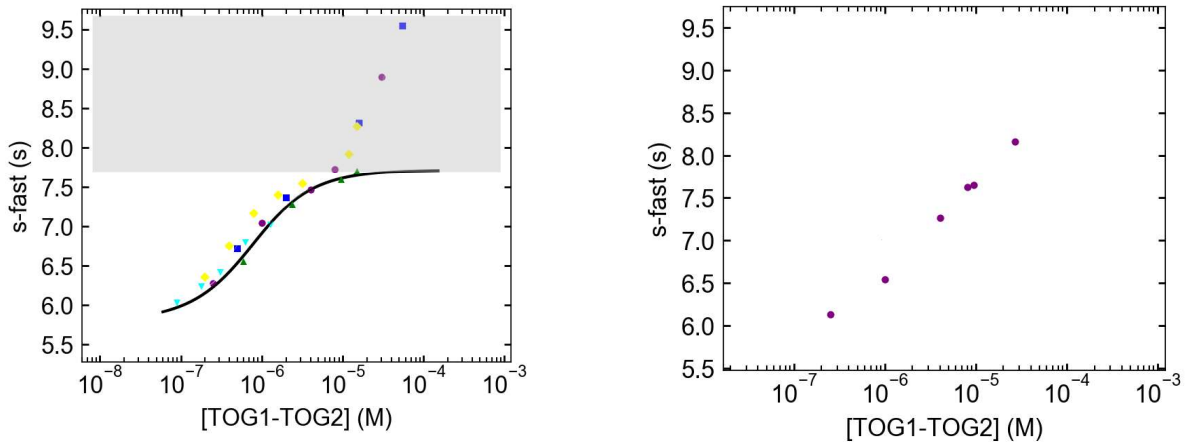
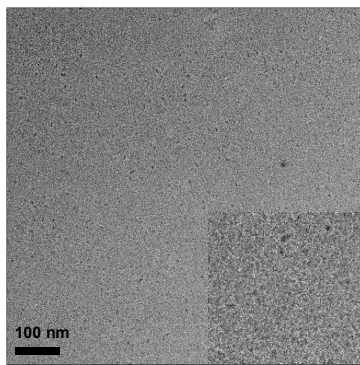
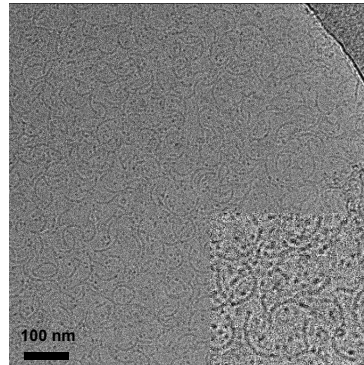


Figure 4.2: Binding isotherms of TOG:tubulin interactions for TOG1-TOG2 region in fungal CLASP homologs show a lack of saturation consistent to that observed in Stu1-TOG1-TOG2.

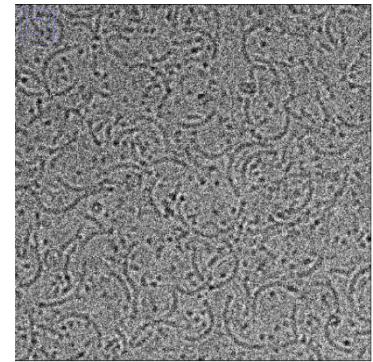
TOG1-TOG2 fragments from CLASPs in *Zygosachharomyces rouxii* (left) and *Kluveromyces dobzhanskii* (right). Dose-dependent increases in *s-fast* are observed for both species ($N = 4$ titrations for *Z. rouxii* indicated by the 4 different colors with a concentration range of $0.1 - 55 \mu\text{M}$ and $N = 1$ for *K. dobzhanskii* with concentration of TOG1-TOG2 ranging from $0.25 - 27 \mu\text{M}$). Isotherms reproducibly fail to saturate at high concentrations. For the *Z. rouxii* isotherm, a one-site binding constant of $\sim 200 \text{ nM}$ is obtained from the low concentration region by excluding data points above the theoretical maximum of 7.2 s . For *K. dobzhanskii*, only three data points are below 7.2 s so this analysis was not carried out.



A. $\alpha\beta$ -tubulin only



B. $\alpha\beta$ -tubulin + Stu1-TOG2
(non-ligated)



C. Enlarged center from B.

Figure 4.3: Tubulin forms “curl”-like oligomers in the presence of Stu1-TOG2 (preliminary data, unpublished).

Micrographs generated by cryoelectron microscopy on 0.4 mg/mL samples of A) $\alpha\beta$ -tubulin only B) $\alpha\beta$ -tubulin + Stu1-TOG2. $\alpha\beta$ -tubulin by itself contains only single particles and no oligomers. Insets show enlarged portions. In the presence of Stu1-TOG2, $\alpha\beta$ -tubulin appears to assemble into “curls”. C) Enlarged center from B. showing “curls” clearly. Buffer conditions for all samples is 25 mM Tris pH7.5, 100 mM NaCl, 1 mM $MgCl_2$ and 1 mM EGTA. All samples were kept cold on ice prior to freezing.

References

- Adams, P.D. (2010). PHENIX: a comprehensive Python-based system for macromolecular structure solution. *Acta Crystallogr. D Biol. Crystallogr* **66**, 213–221.
- Aher, A., Kok, M., Sharma, A., Rai, A., Olieric, N., Rodriguez-Garcia, R., Katrukha, E.A., Weinert, T., Olieric, V., Kapitein, L.C., et al. (2018). CLASP Suppresses Microtubule Catastrophes through a Single TOG Domain. *Dev. Cell* **46**, 40-58.e8.
- Akhmanova, A., and Steinmetz, M.O. (2008). Tracking the ends: a dynamic protein network controls the fate of microtubule tips. *Nature Reviews Molecular Cell Biology* **9**, 309–322.
- Akhmanova, A., and Steinmetz, M.O. (2015). Control of microtubule organization and dynamics: two ends in the limelight. *Nat. Rev. Mol. Cell Biol* **16**, 711–726.
- Akhmanova, A., Hoogenraad, C.C., Drabek, K., Stepanova, T., Dortland, B., Verkerk, T., Vermeulen, W., Burgering, B.M., De Zeeuw, C.I., Grosveld, F., et al. (2001). CLASPs Are CLIP-115 and -170 Associating Proteins Involved in the Regional Regulation of Microtubule Dynamics in Motile Fibroblasts. *Cell* **104**, 923–935.
- Al-Bassam, J., and Chang, F. (2011). Regulation of microtubule dynamics by TOG-domain proteins XMAP215/Dis1 and CLASP. *Trends in Cell Biology* **21**, 604–614.
- Al-Bassam, J., Larsen, N.A., Hyman, A.A., and Harrison, S.C. (2007). Crystal structure of a TOG domain: conserved features of XMAP215/Dis1-family TOG domains and implications for tubulin binding. *Structure* **15**, 355–362.
- Al-Bassam, J., Kim, H., Brouhard, G., van Oijen, A., Harrison, S.C., and Chang, F. (2010). CLASP promotes microtubule rescue by recruiting tubulin dimers to the microtubule. *Dev. Cell* **19**, 245–258.
- Alushin, G.M., Lander, G.C., Kellogg, E.H., Zhang, R., Baker, D., and Nogales, E. (2014). High-Resolution Microtubule Structures Reveal the Structural Transitions in $\alpha\beta$ -Tubulin upon GTP Hydrolysis. *Cell* **157**, 1117–1129.
- Ayaz, P., Ye, X., Huddleston, P., Brautigam, C.A., and Rice, L.M. (2012). A TOG: $\alpha\beta$ -tubulin complex structure reveals conformation-based mechanisms for a microtubule polymerase. *Science* **337**, 857–860.
- Ayaz, P., Munyoki, S., Geyer, E.A., Piedra, F.-A., Vu, E.S., Bromberg, R., Otwinowski, Z., Grishin, N.V., Brautigam, C.A., and Rice, L.M. (2014). A tethered delivery mechanism explains the catalytic action of a microtubule polymerase. *Elife* **3**, 03069.
- Bechstedt, S., and Brouhard, G.J. (2012). Doublecortin recognizes the 13-protofilament microtubule cooperatively and tracks microtubule ends. *Dev. Cell* **23**, 181–192.

- Bharadwaj, R., and Yu, H. (2004). The spindle checkpoint, aneuploidy, and cancer. *Oncogene* 23, 2016–2027.
- Bieling, P., Laan, L., Schek, H., Munteanu, E.L., Sandblad, L., Dogterom, M., Brunner, D., and Surrey, T. (2007). Reconstitution of a microtubule plus-end tracking system in vitro. *Nature* 450, 1100–1105.
- Bratman, S.V., and Chang, F. (2007). Stabilization of overlapping microtubules by fission yeast CLASP. *Dev. Cell* 13, 812–827.
- Brautigam, C.A. (2015). Calculations and Publication-Quality Illustrations for Analytical Ultracentrifugation Data. *Meth. Enzymol* 562, 109–133.
- Brito, D.A., Yang, Z., and Rieder, C.L. (2008). Microtubules do not promote mitotic slippage when the spindle assembly checkpoint cannot be satisfied. *J. Cell Biol.* 182, 623–629.
- Brouhard, G.J. (2015). Dynamic instability 30 years later: complexities in microtubule growth and catastrophe. *Mol Biol Cell* 26, 1207–1210.
- Brouhard, G., and Sept, D. (2012). Microtubules: Sizing Up the GTP Cap. *Current Biology* 22, R802–R803.
- Brouhard, G.J., and Rice, L.M. (2014). The contribution of $\alpha\beta$ -tubulin curvature to microtubule dynamics. *J. Cell Biol.* 207, 323–334.
- Brouhard, G.J., and Rice, L.M. (2018). Microtubule dynamics: an interplay of biochemistry and mechanics. *Nat. Rev. Mol. Cell Biol.* 19, 451–463.
- Brouhard, G.J., Stear, J.H., Noetzel, T.L., Al-Bassam, J., Kinoshita, K., Harrison, S.C., Howard, J., and Hyman, A.A. (2008). XMAP215 Is a Processive Microtubule Polymerase. *Cell* 132, 79–88.
- Byrnes, A.E., and Slep, K.C. (2017). TOG-tubulin binding specificity promotes microtubule dynamics and mitotic spindle formation. *J. Cell Biol* 216, 1641–1657.
- Chaaban, S., and Brouhard, G.J. (2017). A microtubule bestiary: structural diversity in tubulin polymers. *Mol. Biol. Cell* 28, 2924–2931.
- Chalfie, M., and Thomson, J.N. (1982). Structural and functional diversity in the neuronal microtubules of *Caenorhabditis elegans*. *J. Cell Biol.* 93, 15–23.
- Chen, V.B., Arendall, W.B., Headd, J.J., Keedy, D.A., Immormino, R.M., Kapral, G.J., Murray, L.W., Richardson, J.S., and Richardson, D.C. (2010). MolProbity: all-atom structure validation for macromolecular crystallography. *Acta Crystallogr. D Biol. Crystallogr* 66, 12–21.

Chrétien, D., Fuller, S.D., and Karsenti, E. (1995). Structure of growing microtubule ends: two-dimensional sheets close into tubes at variable rates. *J. Cell Biol.* 129, 1311–1328.

Das, A., Dickinson, D.J., Wood, C.C., Goldstein, B., and Slep, K.C. (2015). Crescerin uses a TOG domain array to regulate microtubules in the primary cilium. *Mol. Biol. Cell* 26, 4248–4264.

De la Mora-Rey, T., Guenther, B.D., and Finzel, B.C. (2013). The structure of the TOG-like domain of *Drosophila melanogaster* Mast/Orbit. *Acta Cryst F, Acta Cryst Sect F, Acta Crystallogr F, Acta Crystallogr Sect F, Acta Cryst F Struct Biol Cryst Commun, Acta Cryst Sect F Struct Biol Cryst Commun, Acta Crystallogr Sect F Struct Biol Cryst Commun* 69, 723–729.

Desai, A., and Mitchison, T.J. (1997). Microtubule polymerization dynamics. *Annu. Rev. Cell Dev. Biol.* 13, 83–117.

Díaz, J.F., Valpuesta, J.M., Chacón, P., Diakun, G., and Andreu, J.M. (1998). Changes in microtubule protofilament number induced by Taxol binding to an easily accessible site. Internal microtubule dynamics. *J. Biol. Chem.* 273, 33803–33810.

Duellberg, C., Cade, N.I., Holmes, D., and Surrey, T. (2016). The size of the EB cap determines instantaneous microtubule stability. *Elife* 5, 711.

Emsley, P., Lohkamp, B., Scott, W.G., and Cowtan, K. (2010). Features and development of Coot. *Acta Crystallogr. D Biol. Crystallogr* 66, 486–501.

Fox, J.C., Howard, A.E., Currie, J.D., Rogers, S.L., and Slep, K.C. (2014). The XMAP215 family drives microtubule polymerization using a structurally diverse TOG array. *Mol. Biol. Cell* 25, 2375–2392.

Franke, D., and Svergun, D.I. (2009). DAMMIF, a program for rapid ab-initio shape determination in small-angle scattering. *Journal of Applied Crystallography* 42, 342–346.

Funk, C., Schmeiser, V., Ortiz, J., and Lechner, J. (2014). A TOGL domain specifically targets yeast CLASP to kinetochores to stabilize kinetochore microtubules. *J. Cell Biol* 205, 555–571.

Ganguly, A., Yang, H., and Cabral, F. (2010). Paclitaxel-dependent cell lines reveal a novel drug activity. *Mol. Cancer Ther.* 9, 2914–2923.

Gardner, M.K., Zanic, M., Gell, C., Bormuth, V., and Howard, J. (2011). Depolymerizing Kinesins Kip3 and MCAK Shape Cellular Microtubule Architecture by Differential Control of Catastrophe. *Cell* 147, 1092–1103.

Gell, C., Bormuth, V., Brouhard, G.J., Cohen, D.N., Diez, S., Friel, C.T., Helenius, J., Nitsche, B., Petzold, H., Ribbe, J., et al. (2010). Microtubule dynamics reconstituted in

vitro and imaged by single-molecule fluorescence microscopy. *Methods Cell Biol.* **95**, 221–245.

Geyer, E.A., Burns, A., Lalonde, B.A., Ye, X., Piedra, F.-A., Huffaker, T.C., and Rice, L.M. (2015). A mutation uncouples the tubulin conformational and GTPase cycles, revealing allosteric control of microtubule dynamics. *Elife* **4**, 3389.

Geyer, E.A., Miller, M.P., Brautigam, C.A., Biggins, S., and Rice, L.M. (2018). Design principles of a microtubule polymerase. *Elife* **7**.

Gigant, B., Curmi, P.A., Martin-Barbey, C., Charbaut, E., Lachkar, S., Lebeau, L., Siavoshian, S., Sobel, A., and Knossow, M. (2000). The 4 Å X-ray structure of a tubulin:stathmin-like domain complex. *Cell* **102**, 809–816.

Helenius, J., Brouhard, G., Kalaidzidis, Y., Diez, S., and Howard, J. (2006). The depolymerizing kinesin MCAK uses lattice diffusion to rapidly target microtubule ends. *Nature* **441**, 115–119.

Honnappa, S., Gouveia, S.M., Weisbrich, A., Damberger, F.F., Bhavesh, N.S., Jawhari, H., Grigoriev, I., van Rijssel, F.J.A., Buey, R.M., Lawera, A., et al. (2009). An EB1-Binding Motif Acts as a Microtubule Tip Localization Signal. *Cell* **138**, 366–376.

Howard, A.E., Fox, J.C., and Slep, K.C. (2015). *Drosophila melanogaster* mini spindles TOG3 utilizes unique structural elements to promote domain stability and maintain a TOG1- and TOG2-like tubulin-binding surface. *J. Biol. Chem* **290**, 10149–10162.

Howes, S.C., Geyer, E.A., LaFrance, B., Zhang, R., Kellogg, E.H., Westermann, S., Rice, L.M., and Nogales, E. (2017). Structural differences between yeast and mammalian microtubules revealed by cryo-EM. *The Journal of Cell Biology* [jcb.201612195](https://doi.org/10.1083/jcb.201612195).

Hunter, A.W., Caplow, M., Coy, D.L., Hancock, W.O., Diez, S., Wordeman, L., and Howard, J. (2003). The kinesin-related protein MCAK is a microtubule depolymerase that forms an ATP-hydrolyzing complex at microtubule ends. *Mol. Cell* **11**, 445–457.

Hyman, A.A., Chrétien, D., Arnal, I., and Wade, R.H. (1995). Structural changes accompanying GTP hydrolysis in microtubules: information from a slowly hydrolyzable analogue guanylyl-(α,β)-methylene-diphosphonate. *The Journal of Cell Biology* **128**, 117–125.

Johnson, V., Ayaz, P., Huddleston, P., and Rice, L.M. (2011a). Design, overexpression, and purification of polymerization-blocked yeast $\alpha\beta$ -tubulin mutants. *Biochemistry* **50**, 8636–8644.

Johnson, V., Ayaz, P., Huddleston, P., and Rice, L.M. (2011b). Design, Overexpression, and Purification of Polymerization-Blocked Yeast $\alpha\beta$ -Tubulin Mutants. *Biochemistry* **50**, 8636–8644.

Jordan, M.A., and Wilson, L. (2004). Microtubules as a target for anticancer drugs. *Nat. Rev. Cancer* 4, 253–265.

Laue, T.M., Shah, B.D., Ridgeway, T.M., and Pelletier, S.L. (1992). Analytical Ultracentrifugation in Biochemistry and Polymer Science, edited by SE Harding, AJ Rowe & JC Horton (Cambridge: Royal Society of Chemistry).

Lawrence, E.J., Arpag˘, G., Norris, S.R., and Zanic, M. (2018). Human CLASP2 specifically regulates microtubule catastrophe and rescue. *Molecular Biology of the Cell* 29, 1168–1177.

Leano, J.B., Rogers, S.L., and Slep, K.C. (2013). A cryptic TOG domain with a distinct architecture underlies CLASP-dependent bipolar spindle formation. *Structure* 21, 939–950.

von Loeffelholz, O., Venables, N.A., Drummond, D.R., Katsuki, M., Cross, R., and Moores, C.A. (2017). Nucleotide- and Mal3-dependent changes in fission yeast microtubules suggest a structural plasticity view of dynamics. *Nature Communications* 8.

Longtine, M.S., McKenzie, A., Demarini, D.J., Shah, N.G., Wach, A., Brachat, A., Philippsen, P., and Pringle, J.R. (1998). Additional modules for versatile and economical PCR-based gene deletion and modification in *Saccharomyces cerevisiae*. *Yeast* 14, 953–961.

Majumdar, S., Kim, T., Chen, Z., Munyoki, S., Tso, S.-C., Brautigam, C.A., and Rice, L.M. (2018). An isolated CLASP TOG domain suppresses microtubule catastrophe and promotes rescue. *Molecular Biology of the Cell* 29, 1359–1375.

Maki, T., Grimaldi, A.D., Fuchigami, S., Kaverina, I., and Hayashi, I. (2015). CLASP2 Has Two Distinct TOG Domains That Contribute Differently to Microtubule Dynamics. *J. Mol. Biol* 427, 2379–2395.

Mandelkow, E.M., Mandelkow, E., and Milligan, R.A. (1991). Microtubule dynamics and microtubule caps: a time-resolved cryo-electron microscopy study. *J. Cell Biol.* 114, 977–991.

Manka, S.W., and Moores, C.A. (2018). The role of tubulin-tubulin lattice contacts in the mechanism of microtubule dynamic instability. *Nat. Struct. Mol. Biol.* 25, 607–615.

Maurer, S.P., Fourniol, F.J., Bohner, G., Moores, C.A., and Surrey, T. (2012). EBs recognize a nucleotide-dependent structural cap at growing microtubule ends. *Cell* 149, 371–382.

Maurer, S.P., Cade, N.I., Bohner, G., Gustafsson, N., Boutant, E., and Surrey, T. (2014). EB1 Accelerates Two Conformational Transitions Important for Microtubule Maturation and Dynamics. *Curr. Biol* 24, 372–384.

Miller, M.P., Asbury, C.L., and Biggins, S. (2016). A TOG Protein Confers Tension Sensitivity to Kinetochores-Microtubule Attachments. *Cell* 165, 1428–1439.

Minor, W., Cymborowski, M., Otwinowski, Z., and Chruszcz, M. (2006). HKL-3000: the integration of data reduction and structure solution—from diffraction images to an initial model in minutes. *Acta Crystallogr. D Biol. Crystallogr* 62, 859–866.

Mitchison, T.J. (1993). Localization of an exchangeable GTP binding site at the plus end of microtubules. *Science* 261, 1044–1047.

Mitchison, T., and Kirschner, M. (1984). Dynamic instability of microtubule growth. *Nature* 312, 237–242.

Moriwaki, T., and Goshima, G. (2016). Five factors can reconstitute all three phases of microtubule polymerization dynamics. *J Cell Biol* 215, 357–368.

Nishimura, K., Fukagawa, T., Takisawa, H., Kakimoto, T., and Kanemaki, M. (2009). An auxin-based degron system for the rapid depletion of proteins in nonplant cells. *Nat. Methods* 6, 917–922.

Nogales, E. (2000). Structural insights into microtubule function. *Annu. Rev. Biochem.* 69, 277–302.

Nogales, E., Wolf, S.G., and Downing, K.H. (1998). Structure of the alpha beta tubulin dimer by electron crystallography. *Nature* 391, 199–203.

Nogales, E., Whittaker, M., Milligan, R.A., and Downing, K.H. (1999). High-resolution model of the microtubule. *Cell* 96, 79–88.

Notredame, C., Higgins, D.G., and Heringa, J. (2000). T-Coffee: A novel method for fast and accurate multiple sequence alignment. *J. Mol. Biol* 302, 205–217.

Pasqualone, D., and Huffaker, T.C. (1994). STU1, a suppressor of a beta-tubulin mutation, encodes a novel and essential component of the yeast mitotic spindle. *J. Cell Biol* 127, 1973–1984.

Patel, K., Nogales, E., and Heald, R. (2012). Multiple domains of human CLASP contribute to microtubule dynamics and organization in vitro and in *Xenopus* egg extracts. *Cytoskeleton (Hoboken)* 69, 155–165.

Pettersen, E.F., Goddard, T.D., Huang, C.C., Couch, G.S., Greenblatt, D.M., Meng, E.C., and Ferrin, T.E. (2004). UCSF Chimera—a visualization system for exploratory research and analysis. *J Comput Chem* 25, 1605–1612.

Piedra, F.-A., Kim, T., Garza, E.S., Geyer, E.A., Burns, A., Ye, X., and Rice, L.M. (2016). GDP-to-GTP exchange on the microtubule end can contribute to the frequency of catastrophe. *Mol. Biol. Cell* 27, 3515–3525.

Prota, A.E., Bargsten, K., Northcote, P.T., Marsh, M., Altmann, K.-H., Miller, J.H., Díaz, J.F., and Steinmetz, M.O. (2014). Structural basis of microtubule stabilization by laulimalide and peloruside A. *Angew. Chem. Int. Ed. Engl.* **53**, 1621–1625.

Reid, T.A., Schuster, B.M., Mann, B.J., Balchand, S.K., Plooster, M., McClellan, M., Coombes, C.E., Wadsworth, P., and Gardner, M.K. (2016). Suppression of microtubule assembly kinetics by the mitotic protein TPX2. *J Cell Sci* **129**, 1319–1328.

Rezabkova, L., Kraatz, S.H.W., Akhmanova, A., Steinmetz, M.O., and and Kammerer, R.A. (2016). Biophysical and Structural Characterization of the Centriolar Protein Cep104 Interaction Network. *J. Biol. Chem* **291**, 18496–18504.

Rice, L.M., Montabana, E.A., and Agard, D.A. (2008). The lattice as allosteric effector: Structural studies of $\alpha\beta$ - and γ -tubulin clarify the role of GTP in microtubule assembly. *PNAS* **105**, 5378–5383.

Roostalu, J., Cade, N.I., and Surrey, T. (2015). Complementary activities of TPX2 and chTOG constitute an efficient importin-regulated microtubule nucleation module. *Nat Cell Biol* **17**, 1422–1434.

Scheuermann, T.H., Padrick, S.B., Gardner, K.H., and and Brautigam, C.A. (2016). On the acquisition and analysis of microscale thermophoresis data. *Anal. Biochem* **496**, 79–93.

Schneider, C.A., Rasband, W.S., and and Eliceiri, K.W. (2012). NIH Image to ImageJ: 25 years of image analysis. *Nat. Methods* **9**, 671–675.

Schuck, P. (2000). Size-distribution analysis of macromolecules by sedimentation velocity ultracentrifugation and lamm equation modeling. *Biophys. J* **78**, 1606–1619.

Schuck, P. (2010). Sedimentation patterns of rapidly reversible protein interactions. *Biophys. J* **98**, 2005–2013.

Schwartz, K., Richards, K., and and Botstein, D. (1997). BIM1 encodes a microtubule-binding protein in yeast. *Mol. Biol. Cell* **8**, 2677–2691.

Slep, K.C., and Vale, R.D. (2007). Structural Basis of Microtubule Plus End Tracking by XMAP215, CLIP-170, and EB1. *Mol. Cell* **27**, 976–991.

Svergun, D.I. (1992). Determination of the regularization parameter in indirect-transform methods using perceptual criteria. *Journal of Applied Crystallography* **25**, 495–503.

Svergun, D.I. (1999). Restoring low resolution structure of biological macromolecules from solution scattering using simulated annealing. *Biophys. J* **76**, 2879–2886.

Volkov, V.V., and and Svergun, D.I. (2003). Uniqueness of ab-initio shape determination in small-angle X-ray scattering. *Journal of Applied Crystallography* **36**, 860–864.

Wang, P.J., and Huffaker, T.C. (1997). Stu2p: A microtubule-binding protein that is an essential component of the yeast spindle pole body. *J. Cell Biol.* 139, 1271–1280.

Widlund, P.O., Stear, J.H., Pozniakovsky, A., Zanic, M., Reber, S., Brouhard, G.J., Hyman, A.A., and Howard, J. (2011). XMAP215 polymerase activity is built by combining multiple tubulin-binding TOG domains and a basic lattice-binding region. *Proc. Natl. Acad. Sci U.S.a.*, 108–2741.

Zanic, M., Stear, J.H., Hyman, A.A., and Howard, J. (2009). EB1 recognizes the nucleotide state of tubulin in the microtubule lattice. *PLoS ONE* 4, 7585.

Zhang, R., Alushin, G.M., Brown, A., and Nogales, E. (2015). Mechanistic Origin of Microtubule Dynamic Instability and Its Modulation by EB Proteins. *Cell* 162, 849–859.